

**CHALLENGES OF CONTROL DESIGN FOR  
PRECISION SERVO SYSTEM  
WITH APPLICATION ON HARD DISK DRIVE**

Ehsan Keikha

NATIONAL UNIVERSITY OF SINGAPORE

2013

**CHALLENGES OF CONTROL DESIGN FOR  
PRECISION SERVO SYSTEM  
WITH APPLICATION ON HARD DISK DRIVE**

Ehsan Keikha

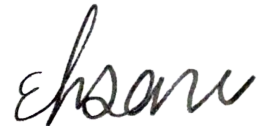
A THESIS SUBMITTED FOR THE DEGREE OF  
DOCTOR OF PHILOSOPHY  
DEPARTMENT OF ELECTRICAL AND COMPUTER ENGINEERING  
NATIONAL UNIVERSITY OF SINGAPORE

2013

**Statement of Originality**

I hereby certify that the content of this thesis is the result of work done by me and has not been submitted for a higher degree to any other University or Institution.

12 December 2013



.....  
Date

.....  
Ehsan Keikha

*This thesis is dedicated to*

*my beloved wife,*

*Neda*

# Acknowledgments

There are many people whom I wish to thank for the help and support they have given me throughout my PhD studies. Foremost, I would like to express my sincere gratitude to my supervisor A/P Abdullah Al Mamun. I thank him for his invaluable guidance, insights and suggestions which helped me throughout this work. Besides my main advisor, I would like to thank Professor Charanjit Singh Bhatia, Professor Roberto Horowitz, Professor T.H Lee and Dr. Yao Kui for their support. Last but not the least, I would like to thank my parents, my parents in law, my brother, and my sister for always being there when I needed them most, and for supporting me through all these years. I would especially like to thank my wife Neda, who with her unwavering support, patience, and love has helped me to achieve this goal. This dissertation is dedicated to her.

# Contents

<b>Acknowledgments</b>	<b>i</b>
<b>Summary</b>	<b>v</b>
<b>List of Tables</b>	<b>vi</b>
<b>List of Figures</b>	<b>vii</b>
<b>Acronyms</b>	<b>xi</b>
<b>1 Introduction</b>	<b>1</b>
1.1 Overview of Precision Servo System . . . . .	1
1.1.1 HDD Servo System components . . . . .	2
1.1.2 Dual-Stage Actuation Servo Systems . . . . .	5
1.2 Servo Control Architecture . . . . .	6
1.3 Motivations . . . . .	8
1.4 Research Objectives . . . . .	12
1.4.1 Integral Resonant Control to Suppress Micro-Actuator Resonance	12
1.4.2 Probabilistic Approach for Design of Robust Control . . . . .	13
1.4.3 Design Controller Under Irregular Sampling . . . . .	14
1.5 Outline of the Thesis . . . . .	15
<b>2 Modeling of HDD</b>	<b>16</b>
2.1 Introduction . . . . .	16
2.2 Experimental Setup . . . . .	17

2.3	Dual-Stage Actuator Modeling . . . . .	20
2.4	Uncertainty Model Characteristic . . . . .	23
2.4.1	Modeling Dynamic Uncertainty . . . . .	23
2.4.2	Modeling Parametric Structured Uncertainty . . . . .	24
2.5	Identification of Disturbance . . . . .	25
2.6	DSA Track-Following Control Design . . . . .	29
2.6.1	Sensitivity Decoupling Method . . . . .	29
2.6.2	Controller Design Results . . . . .	31
2.6.3	Actuated Slider to Achieve a High Bandwidth . . . . .	33
2.7	Conclusion . . . . .	36
<b>3</b>	<b>Integral Resonant Control to Suppress Micro-Actuator Resonance</b>	<b>37</b>
3.1	Introduction . . . . .	37
3.2	Integral Resonant Control: An Overview . . . . .	41
3.3	Effect of Feed-through Term $D_f$ . . . . .	42
3.3.1	Choice of $C(s)$ . . . . .	45
3.3.2	IRC Design for Micro-Actuator with Multiple Resonant Modes	47
3.3.3	Inclusion of Command Input for the Micro-Actuator . . . . .	49
3.3.4	IRC for Suppression of Micro-Actuator Resonance in Dual Stage Actuator . . . . .	49
3.4	Results . . . . .	52
3.4.1	Identification of PZT Micro-Actuator Model . . . . .	52
3.4.2	Design and Evaluation of IRC Compensator for Secondary Ac- tuator . . . . .	54
3.4.3	Results for Dual-Stage Actuator . . . . .	59
3.4.4	Experimental Results . . . . .	63
3.4.5	Conclusion . . . . .	65
<b>4</b>	<b>Probabilistic Approach for Design of Robust Control</b>	<b>67</b>
4.1	Introduction . . . . .	67
4.2	Problem Formulation of Robust Track-Following Control . . . . .	72

4.3	Multi-Objective Robust Control Design based on Linear Matrix Inequality . . . . .	75
4.3.1	Mixed $\mathcal{H}_2/\mathcal{H}_\infty$ Controller . . . . .	76
4.4	Probabilistic Robust Controller . . . . .	78
4.5	Simulation and Experimental Results . . . . .	82
4.5.1	Generalized Plant or Augmented Open-loop . . . . .	82
4.5.2	Performance Verification . . . . .	84
4.5.3	Control Implementation . . . . .	88
4.6	Conclusion . . . . .	90
<b>5</b>	<b>Design Controller under Irregular Sampling</b>	<b>93</b>
5.1	Introduction . . . . .	93
5.2	Model of Servo System under Irregular Sampling . . . . .	97
5.2.1	Regular Sampling and Actuation . . . . .	98
5.2.2	Irregular Sampling and Actuation . . . . .	101
5.2.3	Irregular Sampling with Regular Control Updates . . . . .	103
5.3	Controller Design under Irregular Sampling . . . . .	108
5.3.1	Limits of Performance in HDD . . . . .	108
5.3.2	Probabilistic Control Design for HDD . . . . .	113
5.4	Simulation . . . . .	121
5.4.1	Irregular Sampling and Actuation . . . . .	124
5.4.2	Irregular Sampling and Regular Actuation . . . . .	126
5.5	Conclusion . . . . .	128
<b>6</b>	<b>Conclusions and Future Works</b>	<b>130</b>
6.1	Conclusion . . . . .	130
6.2	Future Works . . . . .	133
	<b>Bibliography</b>	<b>136</b>
	<b>List of Publications</b>	<b>150</b>



# Summary

With the advent of technology of nanoscience and nanotechnology in the past two decades, nanopositioning systems have received a considerable attention from both science and industry. There is an added impetus on design of nanopositioning systems since they have a critical role in achieving speed and accuracy of many devices such as Scanning Probe Microscope (SPM) and Hard Disk Drives (HDD). In this thesis, several challenges on the control design of nano-positioning systems are studied. We mainly focus on the robust control design methodologies. The robustness is in terms of parametric uncertainties of the nominal plant and sampling time variation. The proposed approaches are less conservative and more computational efficient than the conventional robust control design approaches. The HDD servo system is used as an example in the simulation and implementation of these controllers to evaluate the performance of the proposed methods. In nanopositioning systems, the vibration of flexible modes is a major obstacle to achieve higher bandwidth which is required for the demanded performance. An effective method of suppressing these modes in the piezo-electric micro-actuator is presented which is based on the principle of the integral resonant control. Moreover, a multi-objective robust controller is designed which minimizes the worst case root mean square (RMS) value of the positioning error signal (PES) subject to the closed-loop stability in the presence of parametric and dynamic uncertainties. A sequential algorithm based on ellipsoid iteration is utilized to handle the parametric uncertainties. The dynamic uncertainties are also represented as linear fractional transformation (LFT) and by virtue of the small gain theorem, the stability of the closed loop system is guaranteed. The design is less conservative compared to classical robust approaches. Finally, a novel method of discretizing the continuous-time plant dynamics is presented which deals with the systems with irregular sampling rate and regular control update. Irregular sampling is gradually becoming an issue not to be neglected in modern HDDs. In this thesis, a non-sequential probabilistic algorithm based on a relatively new approach called “scenario optimization” is utilized to handle uncertainties with sampling rate in HDD.

# List of Tables

2.1	Setting of DSA and LDV . . . . .	21
2.2	Parameters of the identified VCM model . . . . .	21
2.3	Parameters of the identified PZT micro-actuator model . . . . .	22
2.4	The result of the designed controller designed for a commercial HDD with different sampling rates . . . . .	33
2.5	Controller designed results of NUS/IMRE micro-actuator with differ- ent sampling rates . . . . .	35
3.1	Parameters used for illustration of frequency of under damped zeros. .	43
3.2	Parameters of the identified PZT micro-actuator model. . . . .	53
3.3	Damping of the five modes of the micro-actuator. . . . .	57
4.1	Parameter variation in the plant . . . . .	83
4.2	Comparison of the nominal and worst case stability margins . . . . .	89
4.3	Comparison of the nominal and worst case performance specifications	89
5.1	Comparison of the nominal and worst case performance specifications	127
5.2	Comparison of the nominal and worst case stability margins . . . . .	128

# List of Figures

1.1	Schematic of a hard disk drive . . . . .	3
1.2	Embedded servo sectors and different fields in a servo sector . . . . .	4
1.3	Dual-stage servo configurations. Reprinted with permission,(1) Actuated suspension. (2) Actuated slider. (3) Actuated head . . . . .	5
1.4	Picture of a PZT-actuated suspension (provided by Hutchinson Technology, Inc..) . . . . .	6
1.5	The block diagram of the dual-stage actuators . . . . .	6
1.6	Block diagram of HDD servo system . . . . .	7
2.1	Experimental setup for model identification and implementation of compensator . . . . .	19
2.2	Arrangement for (a) identification experiment and (b) implementation	19
2.3	Measured and identified frequency response for VCM actuator . . . . .	21
2.4	Measured and identified frequency response for PZT actuator . . . . .	22
2.5	Repetitive part of PES . . . . .	26
2.6	Block diagram of HDD servo system . . . . .	28
2.7	PES for 90 revolutions . . . . .	28
2.8	Total PSD, and PSD due to windage, measurement noise and NRRO	28
2.9	Block diagram of the track-following controller design. . . . .	30
2.10	Controller frequency for VCM and PZT . . . . .	32
2.11	Frequency of sensitivity function . . . . .	32
2.12	Experimental measurement of the frequency response of designed PZT	35
2.13	Sensitivity of the simulation results for IMRE/NUS micro-actuator .	36

3.1	Compensator in IRC configuration (a) and in conventional feedback configuration (b) . . . . .	42
3.2	Pole-zero map (left) and Bode magnitude plot (right) of micro-actuator with three resonant modes . . . . .	44
3.3	Root locus with leaky integrator for the nominal plant model . . . . .	47
3.4	Root locus with leaky integrator for the nominal plant model . . . . .	47
3.5	Block diagram of the PZT IRC controller design using the sensitivity decoupling method. . . . .	51
3.6	Equivalent sensitivity function block diagram. . . . .	51
3.7	Measured frequency response of the PZT micro-actuator and the response of identified model. . . . .	53
3.8	Effect of augmenting the transfer function with $D_f$ in parallel. . . . .	55
3.9	Bode plot of the open loop transfer function. . . . .	56
3.10	Simulated Bode (magnitude) plots of uncompensated and compensated micro-actuator. . . . .	58
3.11	Simulated time-domain response of micro-actuator with and without IRC compensator. . . . .	58
3.12	Comparison between simulated responses with IRC and with 10th-order notch filter. . . . .	59
3.13	Sensitivity and complementary sensitivity function. . . . .	60
3.14	Comparison of the nominal and worst case gain margins . . . . .	61
3.15	Comparison of the nominal and worst case phase margins . . . . .	62
3.16	(a) Step response for nominal plant (b) Worst-case step response for the variation in PZT parameter . . . . .	62
3.17	Experimental step response with IRC implemented using dSpace card. . . . .	64
3.18	Experimental step response comparison between IRC and 10th-order notch filter. . . . .	65
4.1	Generalized plant with uncertainty $\Delta$ . . . . .	73
4.2	LFT form of structured uncertainties . . . . .	75

4.3	Probabilistic design procedure . . . . .	81
4.4	The optimal performance weighting function $W_p$ . . . . .	84
4.5	Control Weighting Function for VCM $W_{uv}$ and PZT $W_{um}$ . . . . .	85
4.6	Uncertainty weighting functions for VCM $W_{\Delta V}$ and PZT $W_{\Delta M}$ . . . . .	85
4.7	Augmented Plant . . . . .	86
4.8	Closed loop sensitivity plot with controller designed using probabilistic framework for 500 random samples of $\Delta \in \mathbf{\Delta}$ . . . . .	87
4.9	Closed loop sensitivity plot with $\mathcal{H}_2/\mathcal{H}_\infty$ controller designed using YALMIP for 500 random samples of $\Delta \in \mathbf{\Delta}$ . . . . .	87
4.10	Closed loop eigenvalues plot with controller designed using probabilistic framework for 500 random samples of $\Delta \in \mathbf{\Delta}$ . . . . .	88
4.11	Closed loop eigenvalues plot with $\mathcal{H}_2/\mathcal{H}_\infty$ controller designed using YALMIP for 100 random samples of $\Delta \in \mathbf{\Delta}$ . . . . .	88
4.12	Sensitivity plot of the nominal controller. . . . .	90
4.13	Sensitivity plot of the probabilistic controller. . . . .	90
4.14	Implementation of head position and control signals for $\mathcal{H}_2/\mathcal{H}_\infty$ method	91
4.15	Implementation of head position and control signals for probabilistic method . . . . .	91
5.1	The center of the servo tracks does not exactly coincide with the center of rotation of the disk . . . . .	95
5.2	Schematic timeline for irregular sampling (circles) and regular control (crosses) updates . . . . .	103
5.3	Control architecture for either regular sampling and actuation or irregular sampling and actuation . . . . .	109
5.4	Control architecture for regular actuation, but irregular sampling . . . . .	110
5.5	System structure for control design . . . . .	111
5.6	Block diagram of augmented plant for control design . . . . .	114
5.7	The optimal performance weighting function . . . . .	122
5.8	Bode diagram of controllers design for the nominal system . . . . .	123

5.9	Closed loop sensitivity plot for the nominal system . . . . .	123
5.10	Closed loop sensitivity plot for 500 random realizations for the system with $K_{LQG}$ controller . . . . .	125
5.11	Closed loop sensitivity plot for 500 random realizations for the system with probabilistic $H_2$ controller . . . . .	125
5.12	Closed loop sensitivity plot for 500 random realizations for the system with nominal $H_{Prob}$ controller . . . . .	126
5.13	Empirical Bode magnitude plot of the sensitivity function for $I - I -$ $K_{prob}$ and $I - I - K_{LPTV}$ controller . . . . .	126
5.14	Closed loop sensitivity function at the output of the controller for LPTV and nominal plant . . . . .	128

# Acronyms

BMI	Bilinear Matrix Inequality
DSA	Dual-stage actuation
HDD	Hard Disk Drive
LMI	Linear Matrix Inequality
IRC	Integral Resonant Control
LQG	Linear Quadratic Gaussian
NRRO	Non-Repeatable Runout
PES	Position Error Signal
RMS	Root Mean Square
RRO	Repeatable Runout
SDM	Sensitivity Decoupling Method
TMR	Track Mis-registration
TPI	Track Per Inch
VCM	Voice Coil Motor

# Chapter 1

## Introduction

### 1.1 Overview of Precision Servo System

Nanopositioning systems are precise Mechatronics system designed to move objects with a resolution down to a few nanometers [1]. Nanopositioning systems have numerous applications in the field of space technology, defense, biotechnology, information technology, chemical industries, photonics and test application in the semiconductor devices [2,3]. For instance, inventions of the scanning tunneling microscope (STM) [4] and the atomic force microscope (AFM) [5] have fundamentally changed research in numerous areas to measure the characteristics of the materials. Positioning systems with atomic-scale resolution are also used in the scanning probe microscope (SPM) [6] to atomic and molecular scale. Moreover, in the semiconductor industry, novel nanopositioning tools are needed for the positioning of wafers, mask alignment, and semiconductor inspection systems [7]. Furthermore , ultra-precise nanopositioning systems, sensors, actuators and motion controllers are prime elements for many



new applications such as next-generation space telescopes [8] and molecular biology [9]. For these applications, fast response with a very little overshoot, high bandwidth, large travel range with very high resolution and extremely high precision are the desired characteristics. They pose new challenges for the control of nanopositioning devices [10–12].

With the advent of technology of nanoscience and nanotechnology in the past two decades, nanopositioning systems have received a considerable attention from both science and industry. There is an added impetus to design of nanopositioning systems, since they have a critical role in achieving a high speed and accuracy in the Hard Disk Drives (HDD). Nanometer-scale precision will soon be required for the servo system of HDD to increase the capacity of hard disk drives [13]. Data density in HDD is defined in units of bits per square inch ( $b/in^2$ ). The commercially produced drives have achieved the storage density less than  $1 Tb/in^2$ . The HDD industry projects to achieve storage density of  $10 Tb/in^2$  in the near future [14]. This requires to control the reading/writing head positioned with an accuracy of about  $1 nm$ . To attain this density in magnetic recording disk drives, it is necessary to improve the edge of technology for the servo system in terms of developing actuators with the higher performance and advanced control techniques.

### 1.1.1 HDD Servo System components

Servo control techniques play a vital role in increasing aerial density by providing positioning algorithms which results in higher track per inch (TPI). Although, hard disk

drives have improved enormously in terms of storage capacity and data access time over the past decades, their main functional principle has not changed substantially.

Fig.1.1 shows the schematic of a typical hard disk drive system. It consists of one or more disk platters, a spindle motor, an E-block, suspensions, sliders, magnetic read/write (R/W) heads, a voice coil motor (VCM), and a pivot. Data is stored in

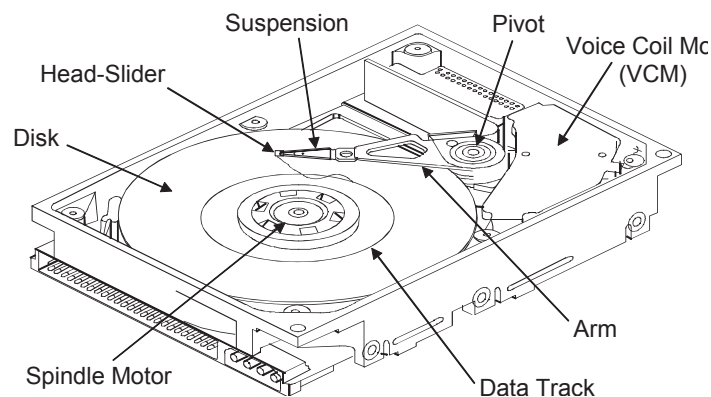


Figure 1.1: Schematic of a hard disk drive

concentric data tracks on circular disks of magnetic media. During operation, the spindle motor spins the disk as fast as 5,400 to 10,000 RPM. It generates a high speed airflow between the slider and disk surface. The sliders fly on a formed air-bearing surface (ABS) [15]. The suspension carries the slider and R/W head. It makes from a thin flexible structure to balance the uplifting aerodynamic force due to the spinning disk. The dynamic balance can keep the slider at a constant flying height of several nanometers over the contours of the disk surface regardless of its undulation and roughness. In addition, the suspension is assembled onto the arms of the E-block that lies between the VCM and suspension and it contains the pivot point. The VCM moves its arm by rotating the E-block around its pivot. Then, it

positions the head at the right radial location for data reading from or writing to disk data tracks.

In order to perform closed-loop feedback control for HDDs, the head position relative to the track must be provided to servo systems. Such a head position feedback signal is referred to as position error signal (PES) and is generated when the read heads pass over the special magnetic patterns called the servo patterns. As shown in Fig. 1.2, servo patterns are written in designated areas on the disk surface known as servo sectors.

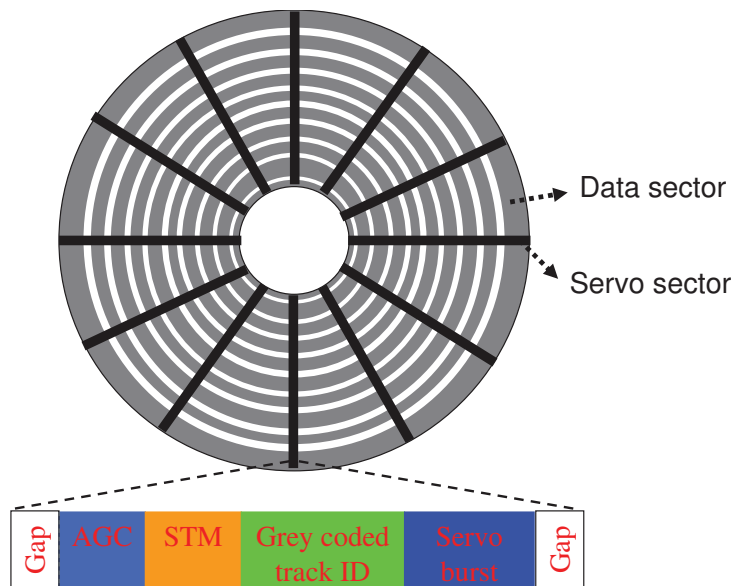


Figure 1.2: Embedded servo sectors and different fields in a servo sector

Different fields in a servo sector are also shown in Fig. 1.2 and each of them contains a specific pattern of magnetization. Usually, these fields [15] are DC-gap field, automatic gain control (AGC) field, servo timing mark (STM) field, grey coded track ID field and PES burst pattern field. Among these fields, only the grey coded track ID field and PES burst pattern field are directly utilized to generate PES. The

grey coded track ID field contains the information about the track number, while the PES burst pattern is decoded to measure the off-track displacement of the read head from the track center, i.e, the fraction of track-pitch.

### 1.1.2 Dual-Stage Actuation Servo Systems

Dual-stage actuation (DSA), which combines the traditional VCM with an additional micro-actuator, has been proposed as a means of enhancing servo tracking performance by increasing the servo bandwidth. The configurations of dual-stage actuators can be categorized into three groups according to the location of the secondary actuator: actuated suspension, actuated slider and actuated head. Fig. 1.3. In all these

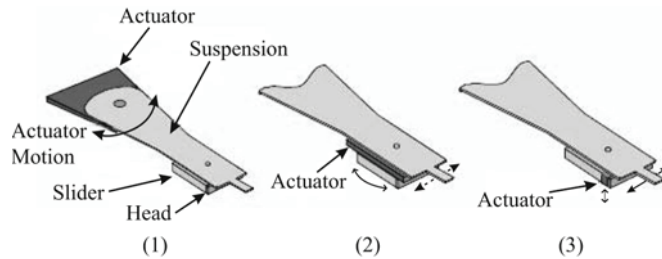


Figure 1.3: Dual-stage servo configurations. Reprinted with permission,(1) Actuated suspension. (2) Actuated slider. (3) Actuated head

configurations, the actuation forces are generated by piezoelectric, electrostatic, or electromagnetic microactuators. In this thesis, we will focus on the control design of DSA servo systems with actuated suspensions. Fig. 1.4 shows the picture of a PZT-actuated suspension provided by Hutchinson Technology, Inc(HTI). Two piezoelectric actuator, shown in yellow, are placed near the suspension. They generate a push-pull action when driven by differential voltages. Meanwhile, a leverage mechanism is utilized to convert and amplify this small actuation displacements into large

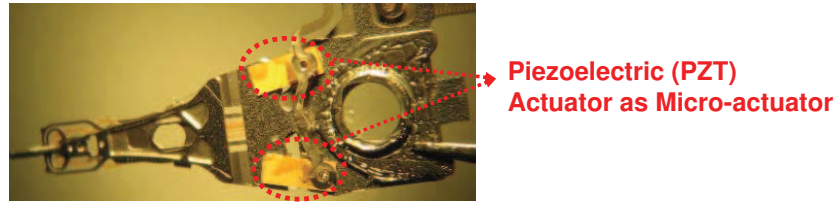


Figure 1.4: Picture of a PZT-actuated suspension (provided by Hutchinson Technology, Inc..)

head motion. Since dual-stage HDDs have two actuators, a DSA servo system can be represented by a dual-input-single-output (DISO) system as shown in Fig.1.5(a). Since the PZT actuators may also excite some suspension resonance modes, the dual-stage actuators can be further represented as a DISO system with common suspension resonance modes as shown in Fig.1.5(b). For the DSA servo control design, we have to substitute the DISO plant  $G_p$  shown in Fig. 1.5(b) into the plant  $G$  in Fig.1.6. As a result, the feedback controller in the servo architecture turns out to be a single-input-dual-output (SIDO) system.

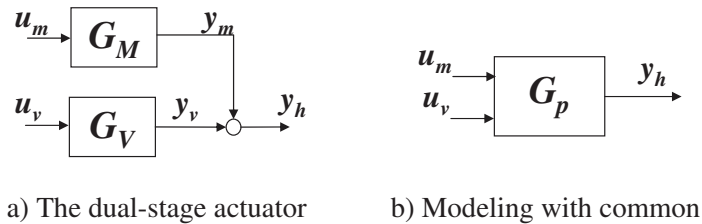


Figure 1.5: The block diagram of the dual-stage actuators

## 1.2 Servo Control Architecture

HDD servo control systems involve three types of control task [16]: track-following control, track-seeking control and settling control. The head positioning track-seeking

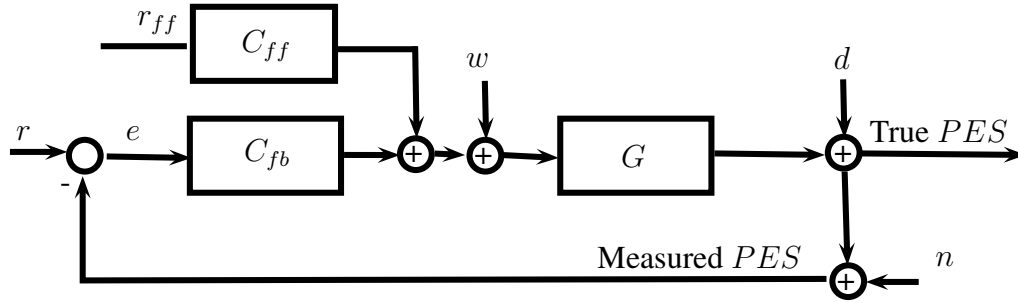


Figure 1.6: Block diagram of HDD servo system

control moves the R/W head as fast as possible from one track to another when commanded by the system. As the head approaches the desired track, a settling control allows the smooth settling of the head within a small distance from the track while minimizing the excitation of mechanical vibration. Once the head is within a sufficiently small distance from the desired data track, its motion is regulated by track-following control. So that, it can follow the center of the data track as precisely as possible during the operation of reading or writing data. This thesis will focus on the track-following control synthesis. A typical hard disk drive servo control system can be represented by the block diagram shown in Fig. 1.6.  $G$  is the disk drive actuator plant;  $C_{fb}$  and  $C_{ff}$  are the feedback and feedforward controllers, respectively;  $r$  denotes the reference input, which is zero in a track-following control mode and a desired position trajectory in a track-seeking control mode;  $d$  represents all of disturbances including repeatable runout (RRO) and repeatable runout non-repeatable runout (NRRO) contributing to PES;  $w$  is the effect of airflow disturbance on the PES which is called windage;  $r_{ff}$  is a reference input to the feedforward controller;  $TruePES$  is the absolute position of the R/W head and  $MeasuredPES$  is the PES after being contaminated by noise  $n$ .

## 1.3 Motivations

The amount of worldwide data storage is estimated to be 600 *exabyte* which is equivalent to 600 *million* HDD each with a capacity of 1 *TB*. More than 52% of this data storage requirement is met by using HDDs [17]. Continuing this trend by the growth of internet, cloud computing and other similar technologies means a growing demand for the higher data storage capacity and consequently the number of HDDs produced. To meet such an increasing demand, it is important to increase not only the production volume but also the storage density in each HDD.

Achievable track density depends on the performance of the head positioning servomechanism of HDD, i.e., how well the R/W head is made to follow the center of a data track. The most important performance measure in HDD servo is Track Mis-registration (TMR) which is the variance of the deviation of R/W head from the center of a data track [15]. Writing and readback of data with bit error rate less than required tolerance level, demands for  $3\sigma$  of TMR to be less than 10% of track pitch (distance between the center of two adjacent tracks). Assuming a bit aspect ratio (ratio between bit length and bit width) of 2:1, storage density of 10 *Tb/in<sup>2</sup>* demands track density of 2,200,000 TPI. This translates into a TMR less than 1.16 nanometer to meet the requirements for 10 *Tb/in<sup>2</sup>* storage density. Such high performance must be achieved in a robust manner because of the plant uncertainty in HDD dynamic systems.

HDDs are normally produced in huge batches. Although, all of them have shared the same nominal properties, each drive has slightly different dynamic response. In

addition, changes in servo system dynamics over time and in different operating conditions are unavoidable. After a servo control is embedded in disk drive systems, for each individual disk drive, it is not feasible to fine-tune the controller parameters. Hence, the same controller should stabilize and perform well on all these disk drives. Consequently, the main challenge in designing HDD servo controller is to improve the nominal performance; meanwhile, the controller should be able to make the closed loop system robust against variations in dynamics. Such an approach was not essential in the past when TMR tolerance was not very stringent. The trend in increasing the data density now makes use of new approaches in the hardware such as using dual-stage servo systems and new modern controller techniques such as robust controller for HDD. Classic control design techniques such as PID control combined with lead-lag compensators yield sufficient tracking performance in older generation hard drives. Using the notch filter in the cascade with the actuator driver has been widely used in head positioning servomechanism of HDDs [15, 18–20]. However, the notch filter creates rapid changes of phase near resonant frequencies leading to degradation in the phase margin and robustness. The solution using notch filter is also sensitive to variations in resonant mode parameters of actuator. Implementing such a filter with fixed notch frequencies also does not consistently yield good performance. This is because, the manufacturing tolerance and discrepancies in the resonance frequency exist even in the same batch of mass produced actuators. Such shortcoming can be solved by using an adaptive notch filter [21, 22]. However, the order of the notch filter transfer function becomes very large if we have to suppress several resonant modes; which results in a higher computational complexity for implementing the adaptive



algorithm. Some researchers used an adaptive mechanism without explicit use of a notch filter [23] in the cost of increased complexity in design and implementation.

In many systems, the sampling frequency is adjusted by hardware constraints and the servo designer does not enjoy the liberty of choosing any arbitrarily high sampling frequency. The head positioning servomechanism in HDD units is an example of systems with sampling restriction. In such case, if a resonant mode exists near the Nyquist frequency, the digital realization of notch filter fails to be effective in suppressing that resonance. Multi-rate realization of the notch filter is a possible solution in those cases [24]. It can also be noted that the authors of [25] used another approach to suppress actuator vibration by properly shaping the input signal such that the actuator output remains vibration-free. However, the method requires an accurate model of the actuator, and robustness is compromised when servo control is to be designed for mass-produced actuators.

From the control design point of view, advanced techniques such as linear quadratic Gaussian (LQG) and linear loop-transfer recovery (LTR) [18, 26], adaptive control [27, 28], iterative learning control [29] are proposed. In addition to some robust control techniques such as Robust  $\mathcal{H}_2$ , mixed  $\mathcal{H}_2/\mathcal{H}_\infty$  and  $\mu$ -synthesis have been studied for HDD servo control [30–32]. However, classical robust multi-objective framework suffers from a number of theoretical limitations due to its deterministic nature. These limitations can be generally divided into two main groups, namely computational complexity and the issue of conservatism. Various robust control problems have been proved to belong to the category of “intractable” problems, which is generally denoted as “NP-hard” [33]. In general, the design of robust output-feedback controllers

leads to bilinear (or rather bi-affine) matrix inequality terms (BMIs) [34], which are NP-hard in nature [35]. Available algorithms to solve such problems are typically based on the iterative methods which are computationally expensive, specially for higher-order plants. To overcome the conservatism, Conway et al. in [36] proposed an approach on utilizing parameter dependant Lyapunov function to design single robust controller for polytopic parameter uncertain system which led to improvement in the performance of HDD. However, due to the limitations in the existing numerical solvers, this method is just applicable to problems of modest size with few number of uncertainties. The problem even would be more complicated when it deals with time varying systems.

Since the control theory for linear time-invariant (LTI) systems has been well studied, most of HDD servos are designed based on a regular sampling rate, i.e. equidistant sampling intervals. However, sometime an irregular sampling rate caused by irregular PES sampling is unavoidable in new generation of HDDs. Irregular sampling will be a more frequent problem when disks are prewritten with servo patterns as in case of discrete-track HDD or bit patterned media HDD [37] [38]. Moreover, false PES demodulation, due to incorrect servo address mark (SAM) detection [39] or damaged servo patterns in several servo sectors, makes the feedback PES unavailable in those servo sectors, resulting in an irregular sampling rate. So far, not much attention has been paid to these irregular sampling rates in previous work.

## 1.4 Research Objectives

In this thesis, several challenges on the control design of nano-positioning systems are studied. We mainly focus on the robust control design methodologies. The robustness is in terms of parametric uncertainties of the nominal plant and sampling time variation. The proposed approaches are less conservative and more computationally efficient than the conventional robust control design approaches. The HDD servo system is used as an example in the simulation and implementation of these controllers to evaluate the performance of the proposed methods. This section briefly presents the main contributions of this thesis.

### 1.4.1 Integral Resonant Control to Suppress Micro-Actuator Resonance

The resonant modes of the micro-actuator is one of the major obstacles to achieve a high bandwidth. In order to set the necessary bandwidth to be sufficiently high, the servo designer must have the resonant vibrations suppressed, so that, the necessary precision requirements are met. The conventional approach is to use notch filters in cascade with the actuator to provide high attenuation at frequencies of these resonances. In this thesis:

- An effective method of suppressing vibration of the flexible modes of a piezoelectric micro-actuator based on the principle of the integral resonant control is presented.

- The application of this approach to suppress the secondary stage resonant mode for the dual-stage HDD is investigated.
- The effectiveness of the design is underscored through simulations and experimental verifications.

### 1.4.2 Probabilistic Approach for Design of Robust Control

Designing a nano-positioning controller using a robust control approach based on semi-definite programming (SDP) has received considerable attention. However, these approaches are too conservative and computationally complex to deal with a system with parametric uncertainty. To overcome these limitations of robust control design, a new framework known as the probabilistic approach is introduced. In probabilistic robust control design, randomized algorithms are employed to handle uncertainty and convex optimization is used to compute the design parameters of the controller. In this thesis:

- A multi-objective robust controller is designed which minimizes the worst case root mean square (RMS) value of the desired output subject to the closed-loop stability in the presence of parametric and dynamic uncertainties.
- A sequential algorithm based on ellipsoid iteration is utilized to handle parametric uncertainty. Dynamic uncertainty is also represented as linear fractional transformation (LFT) and by the virtue of small gain theorem, the stability of closed-loop system is guaranteed.

- Two sources of conservatism are avoided: embedding the original non-linear parametric uncertainty into affine structure (converting the original uncertain system into a polytopic uncertain system) and using a single Lyapunov matrix to test all the objectives.
- The proposed controller is implemented on a HDD and shows drastic improvement in the track following performance compared to the classical robust approaches.

### 1.4.3 Design Controller Under Irregular Sampling

Sampled-data systems with a known constant sampling interval have been extensively studied over the past decades and the systems can be analyzed in the discrete time. When the sampling interval is inconsistent, the situation becomes complicated. For a system with irregular sampling, there are two meaningful schemes for updating the control action. In the first scheme, the control action is updated as quickly as possible after a measurement is obtained, which causes the control rate to be irregular as well. In the second scheme, the control action is updated at a regular rate. In this thesis:

- Irregular Sampling and actuation behavior is modeled by applying a novel discretization method to a continuous-time model.
- A robust probabilistic control design methodology under irregular sampling is proposed. This approach is based on a non-sequential randomized technique, called scenario probabilistic design.

- Proposed method is used to address the problem of the track following controller design in a HDD with irregular sampling.

## 1.5 Outline of the Thesis

Chapter 2 presents the modeling and identification of a generalized dual-stage actuator which consists of nominal model, uncertain parameters and disturbances. These models are later used for controller design and simulations in the rest of this thesis. Chapter 3 provides an introduction to the integral resonant control (IRC) and shows the steps used to design the compensator for a piezoelectric micro-actuator. Moreover, it presents the applicability of this approach in DSA of HDD. In Chapter 4, a discrete time multi-objective robust controller is designed using a probabilistic robust approach to handle different parametric and dynamic uncertainties. An iterative algorithm based on ellipsoid iteration is used to find the probabilistic robust feasible solution. The Chapter 5 presents a novel discretization method for a system with different irregular sampling and actuation schemes. In addition, the details of the probabilistic controller design with the scenario approach for the discrete-time systems are presented. Chapter 6 concludes this thesis by summarizing the results and major achievements. Recommendations for future work are also discussed.

# Chapter 2

## Modeling of HDD

### 2.1 Introduction

In order to design a controller for a dynamic system, it is necessary to have a model that adequately describes the dynamic characteristics of the system. This chapter presents basic methodologies for system identification of dual-stage servo systems, which will be utilized in the coming chapters of this dissertation.

There are two approaches to obtain plant models such as analytical derivation and system identification. The analytical model is developed from the law of nature. Hence, the knowledge from physics of the plant is essential for deriving the model. The system identification determines a mathematical model for a system based on experimental verification data. In this approach, the plant is taken as a black box and it only measures its input and output characteristics. A large variety of methods have been developed to determine a system model of HDD servo system in either the time domain [40, 41] or frequency domain [20, 42–44]. This chapter gives a brief

introduction to the type of VCM and PZT used in this thesis. Then, it describes the modeling process to obtain mathematical plant models for both the VCM and PZT actuators. Various types of plant uncertainties are modeled for the servo system, so that the stability robustness and performance robustness can be considered in controller design and closed-loop system analysis. Disturbance of the servo system is identified based on the time domain analysis.

In addition, dual-stage control structures as well as guidelines for control design of the dual-stage actuation system will be described in this chapter. A case study example is used to demonstrate the dual stage actuator design and limit of performance of the modeled HDD. Finally, a simulation case study is conducted using a new secondary actuator designed in Institute of Materials Research and Engineering (IMRE) and NUS and a commercial drive model to predict the achievable TPI.

## 2.2 Experimental Setup

In order to design controllers for any dual-stage actuation servo system, the plant models of both VCM and secondary actuator PZT need to be obtained using time or frequency domain system identification technique. In the experimental studies of HDD servos, the system identification using persistent excitation of swept sine signal is a popular method to obtain the plant model. Fig. 2.1 illustrates the experimental setup used to determine the frequency response of both actuators. The setup consists of a Dynamic Signal Analyzers (DSA)<sup>1</sup>, a Laser Doppler Vibrometer (LDV)<sup>2</sup>, VCM

---

<sup>1</sup>NI PXI 4461 , National Instrument , USA

<sup>2</sup>Polytec OFV 5000, Polytec, Waldbronn, Germany.



and PZT power amplifier and spindle motor driver. The device under test (DUT) is a 3.5" HDD. The rotational speed is fixed at 7200 *rpm* using the spindle motor driver and all experiments are carried out on a vibration free table.

In the head positioning servomechanism of HDD, position feedback is obtained from the read-back signal produced by sensing the special magnetic patterns written on disks. Since, the PES of the servo mechanism is not directly available, an LDV is used to measure the radial motion of read/write head slider. So, a hole was cut through the case of the drive to make laser shine into the drive. It should be noted that these modifications affected the response of the drive and may have detrimental effect on the attainable performance of the servo system.

The DSA is used for generating excitation signals as well as measurement of response. The acquisition of the output signals is carried out using a high-performance and high-accuracy analog I/O device. The board has two digital to analog converters (DAC) and two analog to digital converters (ADC), though only one ADC is used. Each channel has its own sigma-delta converter with 24-bits of resolution and a maximum sampling rate of 100 ks/s.

The excitation signal and the LDV output are fed into two channels of the DSA. The magnitude and phase of the LDV output are compared to the measured stimulus signal to calculate the Frequency Response Function (FRF). The integration time and settling time are set at 10 cycles and also resolution for each sweep is set as 400 points. While measuring the frequency response of the VCM, the input to the PZT is set to zero and vice versa. For implementation of the compensator, the setup is

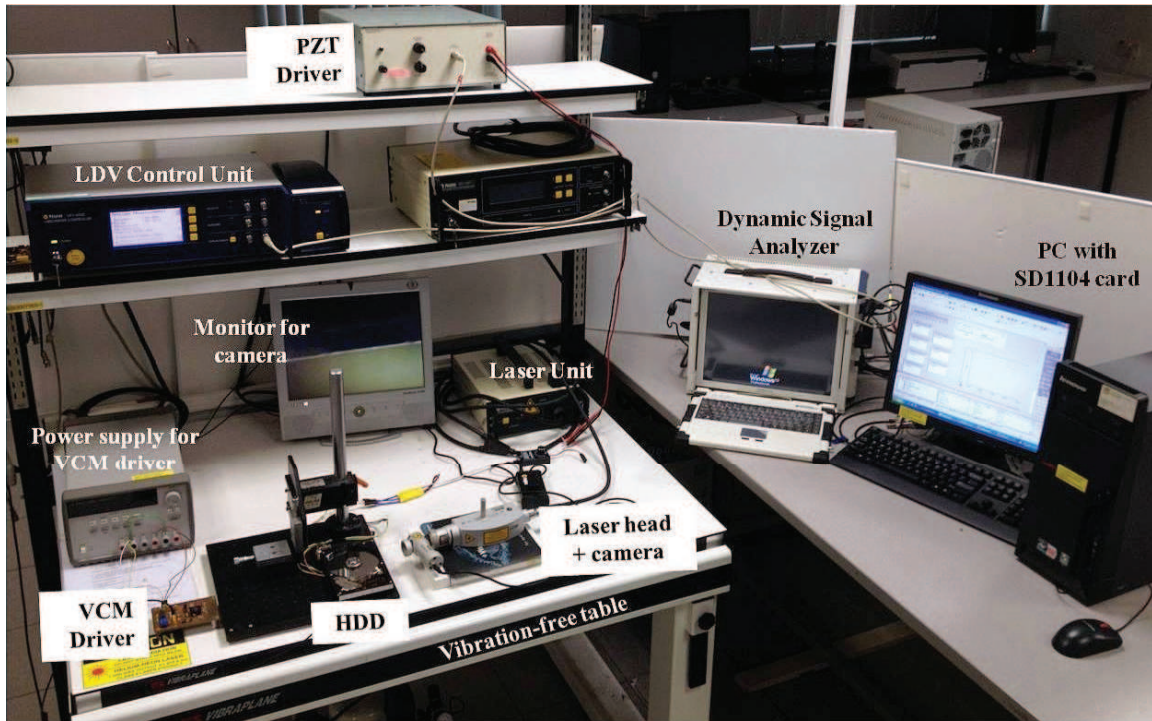


Figure 2.1: Experimental setup for model identification and implementation of compensator

modified by replacing the DSA with a real-time controller card <sup>3</sup>. The arrangement for model identification experiment and implementation are illustrated in Fig 2.2.

<sup>3</sup>DSpace DS1103, a product of dSPACE GmbH, Paderborn, Germany

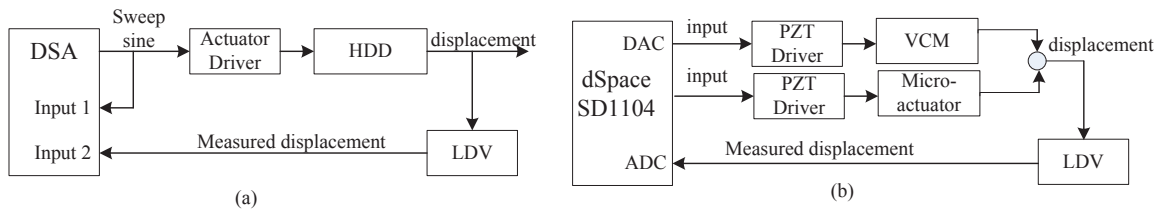


Figure 2.2: Arrangement for (a) identification experiment and (b) implementation

## 2.3 Dual-Stage Actuator Modeling

The frequency response of the VCM, shown in Fig. 2.3, is measured from the input of its current amplifier to the slider motion. Since, the magnitude of the VCM's frequency response covers a wide range, the frequency response data of the VCM drive is collected over three different ranges. As shown in Table 2.1, they have the different excitation level and LDV resolution. By collecting the frequency response data over three different ranges, a swept sine signal with sufficiently large amplitude can be injected into the VCM. The sufficiently large voltage signal can be obtained from the LDV, so that the signal to noise ratio remains sufficiently large for each frequency ranges. This is for improving the accuracy of the measured frequency response.

The experimental data shows several distinct resonance modes. Hence, it is appropriate to describe the transfer function between each input-output pair as sum of  $N$  modes. The transfer function of VCM is as follow:

$$G_{VCM} = G_{pade}(s) \sum_{i=1}^4 \frac{A_{vi}}{s^2 + 2\zeta_{vi}\omega_{vi}s + \omega_{vi}^2} \quad (2.1)$$

In total, four resonant modes are modeled. It gives a model of order of 9, including the delay which is modeled using first order Pade's approximation.

Fig. 2.4 shows the measured frequency response as well as the modeled frequency response of the PZT micro-actuator. In total, three resonant modes are modeled and the resulting model has an order of 7, including the delay which is modeled using first order Pade approximation.

Table 2.1: Setting of DSA and LDV

Frequency range	Excitation level (DSA)	LDV resolution
10 – 100Hz	1mVpk	1.0μmV
100 – 3000Hz	10mVpk	500nmV
3000 – 10,000Hz	30mVpk	200nmV
10,000 – 25,000Hz	1000mVpk	100nmV

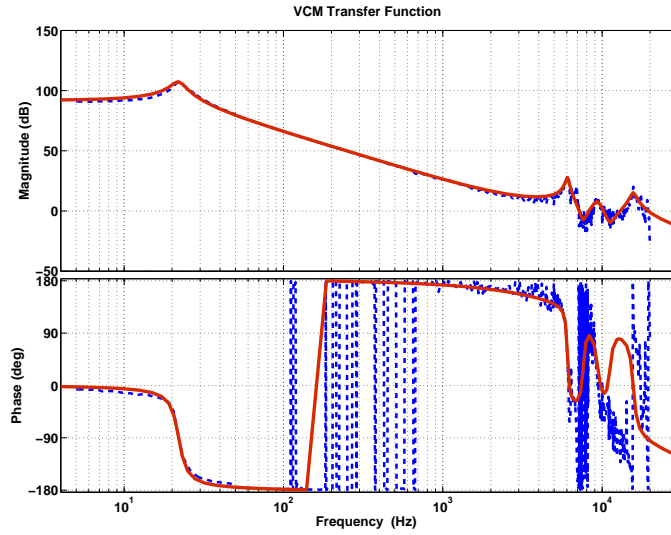


Figure 2.3: Measured and identified frequency response for VCM actuator

Table 2.2: Parameters of the identified VCM model

n	$\omega_{vi}$ (rad/sec)	$\zeta_{vi}$	$A_{vi}$
1	$2\pi \times 22$	0.08	7.6e8
2	$2\pi \times 6063$	0.02	-1.5e9
3	$2\pi \times 9358$	0.06	-1e9
4	$2\pi \times 15693$	0.02	-4.5e9

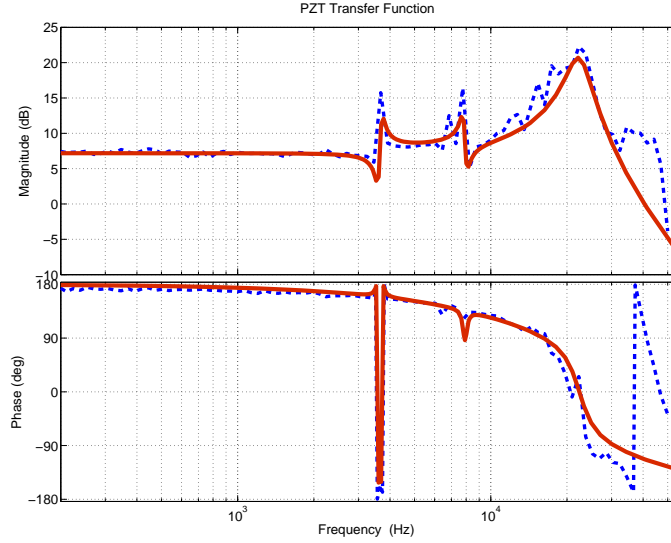


Figure 2.4: Measured and identified frequency response for PZT actuator

Table 2.3: Parameters of the identified PZT micro-actuator model

n	$\omega_{mi}$ (rad/sec)	$\zeta_{mi}$	
1	$2\pi \times 3690$	0.02	-6e7
2	$2\pi \times 7845$	0.02	2.4e8
3	$2\pi \times 22360$	0.01	4.5e10

$$G_{PZT} = \sum_{i=1}^3 \frac{A_{mi}}{s^2 + 2\zeta_{mi}\omega_{mi}s + \omega_{mi}^2} \quad (2.2)$$

The dual-stage actuator system is modeled as a double-input-single-output system resulted from combining the VCM and PZT in a parallel architecture. With the identified disturbances presented in the following section, the complete dual-stage servo system is modeled as the block diagram illustrated in Fig. 2.9

## 2.4 Uncertainty Model Characteristic

Model uncertainty is inherent in all dynamic systems. Since, HDDs are fabricated in batches, the dynamic properties of each drive has slightly different with the nominal model. It is infeasible to fine tune the parameter of the controller for each individual disk drive when servo control is embedded in disk drive systems. Therefore, the same controller should stabilize and perform well for all of these disk drives. This raises the issue of performance robustness and stability robustness of servo system in the HDDs. In this section, different types of plant uncertainties are modeled for the dual-stage system.

### 2.4.1 Modeling Dynamic Uncertainty

For the experimental data of the dual-stage actuator, variations in the dynamic behavior with an unknown cause or structure can be represented by a multiplicative dynamic uncertainty description. That is well suited for representing unstructured dynamical variations [45].

$$\mathbf{P}_m = P|P = P_0(1 + W_m\Delta_m), \|\Delta_m\| \leq 1 \quad (2.3)$$

In 2.3 ,  $P_0$  is used to denote the nominal model, and  $W_m$  is a weighting function, which models the size and shape of the multiplicative perturbation. The stable (and possibly structured) norm bounded dynamic perturbation  $\Delta_m$  is a bounded perturbation that models the dynamic variations in the frequency response measurements. To complete the multiplicative unstructured uncertainty description, both the nominal

model  $P_0$  and a stable and stably invertible weighting function  $W_m$  in 2.3 need to be derived from the experimental data.

### 2.4.2 Modeling Parametric Structured Uncertainty

More detailed information on structural variations in the location and damping of the resonance modes of the dual-stage actuator should be captured using a structured uncertainty description. Assuming uncertainty on stiffness and damping parameters, it is possible to describe variations of the MA and the VCM dynamics as transfer functions that include series combinations of second order uncertain modal transfer functions, with parameters that are affine functions of constant perturbations.

$$\begin{aligned} G_{VCM}(s) &= \sum_{i=1}^{m_1} \frac{A_{vi}}{s^2 + 2\bar{\zeta}_{vi}\bar{\omega}_{vi}s + \bar{\omega}_{vi}^2} \\ P_{PZT}(s) &= \sum_{i=1}^{m_2} \frac{A_{mi}}{s^2 + 2\bar{\zeta}_{mi}\bar{\omega}_{mi}s + \bar{\omega}_{mi}^2} \end{aligned} \quad (2.4)$$

Where  $m_1$  and  $m_2$  are the total number of uncertain modes. The uncertain coefficients in 2.4 are assumed to be affine functions of constant but unknown perturbations.

$$\begin{aligned} \bar{\zeta}_{vi} &= \zeta_{vi}(1 + p_{\zeta_{vi}}\delta_{vi}) \\ \bar{\zeta}_{mi} &= \zeta_{mi}(1 + p_{\zeta_{mi}}\delta_{mi}) \\ \bar{\omega}_{vi} &= \omega_{vi}(1 + p_{\omega_{vi}}\delta_{vi}) \\ \bar{\omega}_{mi} &= \omega_{mi}(1 + p_{\omega_{mi}}\delta_{mi}) \end{aligned} \quad (2.5)$$

where  $\zeta_{vi}, \zeta_{mi}, \omega_{vi}$  and  $\omega_{mi}$  are the nominal values of the coefficients,  $p_{\zeta_{vi}}, p_{\zeta_{mi}}, p_{\omega_{vi}}, p_{\omega_{mi}}$  are constant weighting coefficients,  $\delta_{vi}, \delta_{mi}, \delta_{vi}, \delta_{mi}$  are structured perturbations of unity magnitude. Both the nominal coefficients and the weighting coefficients need to be identified from the experimental data. Chapter 4 illustrates on how both dynamic unstructured and parametric structured uncertainty models for dual-stage actuators can be derived on the basis of experimental frequency domain data.

## 2.5 Identification of Disturbance

In the HDD disturbances are separated into the repeatable runout (RRO) and non-repeatable runout (NRRO). RRO mainly results from the spindle motor vibration. Hence, the disk eccentricity and non-ideal servo track writing is synchronous with the disk rotation speed. All other runout excluding RRO is referred to as NRRO. Furthermore, non-repeatable runout can be in turn categorized into torque disturbance, windage, non-repeatable disk motions and measurement noises. The torque disturbance, which is mainly caused by the bias force of the flexible cable, pivot friction and air-turbulence impinging on the voice coil motor, is typically a low frequency disturbance. Windage, which is due to air-turbulence directly exciting suspension resonance modes, is primarily a high frequency disturbance. Non-repeatable disk motions, which directly affect the position of R/W head relative to the servo track, result in additional track runout. Measurement noise, representing the effects of PES demodulation noise, includes electrical noise and A/D quantization noise.

In this section, disturbances are analyzed using PES measurement of a commercial



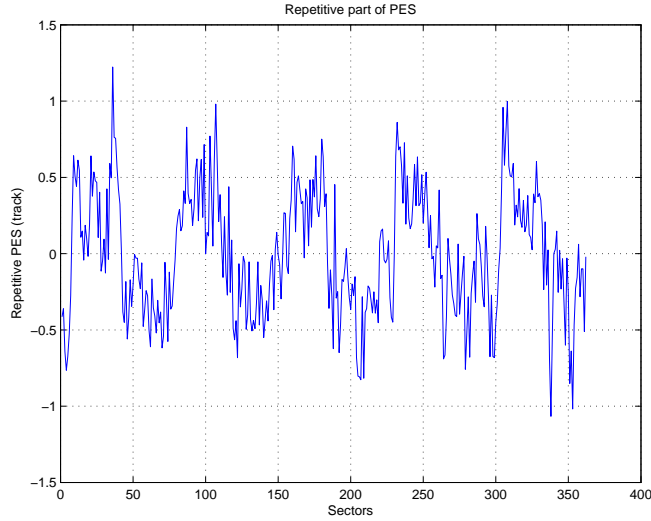


Figure 2.5: Repetitive part of PES

HDD. The repeatable portion of the mechanical disturbance can be obtained by averaging the PES from a number of revolutions of HDD. PES at 90 consecutive revolutions are measured during track following. The RRO at each sector is computed by averaging all of the PES values measured at that sector. Fig.2.5 shows the RRO over different sectors.

The remaining part of the PES is referred as NRRO. As shown in the Fig. 2.6, NRRO disturbances are classified into windage ( $w$ ), output disturbance ( $d$ ) and noise ( $n$ ). They contribute to servo error, PES. In separating  $w$ ,  $d$ , and  $n$ , it is assumed that  $n$  and  $d$  are white noise and  $w$ ,  $d$ , and  $n$  are completely uncorrelated with each other. Therefore, input-output relation in servo system is expressed in (2.6) and its Power Spectral Density (PSD) becomes (2.7). In this study,  $Pw$  arisen from  $w$  is used

in calculation for convenience.

$$PES_t = SPw + SG_r d - Tn \quad (2.6)$$

$$PES = PES_t + n = S(Pw + G_r d + n)$$

$$S_{PES} = |S|^2(|P|^2 S_w + |G_r|^2 S_d + S_n) \quad (2.7)$$

where  $PES_t$  is true PES in Fig. 2.6,  $G$ ,  $T$  and  $S$  are plant transfer function, closed loop transfer function and sensitivity transfer function, respectively. Here, Windage and measurement noise are modeled as white noises with the variance  $\sigma_w^2$  and  $\sigma_n^2$ , respectively. The track runout, caused by disk vibrations and spindle vibrations, is modeled as a color noise generated by feeding a white noise  $d_r$  input to the filter  $G_r(s)$ . The disturbance models  $\sigma_w^2$ ,  $\sigma_n^2$  and  $G_r(s)$  can be identified from the closed-loop PES power spectrum density with the power spectrum density decomposition techniques [40]. Fig. 2.7 shows the complete identified model of the NRRO disturbance of the HDD and the calculated value for each parameter is as follows :

$$\begin{aligned} \sigma_w^2 &= 2.0000e - 05 \\ \sigma_n^2 &= 0.0014 \end{aligned} \quad (2.8)$$

$$G_r = \frac{37.7s^2 + 3.584e05s + 8.5e09}{s^3 + 5404s^2 + 2.161e08s + 5.249e11}$$

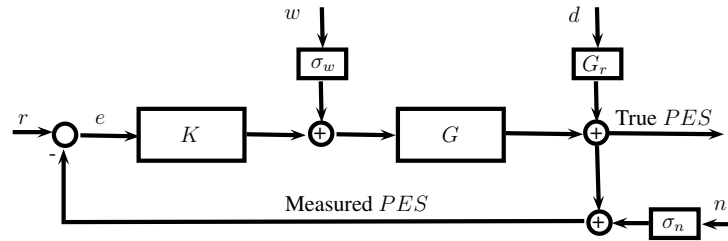


Figure 2.6: Block diagram of HDD servo system

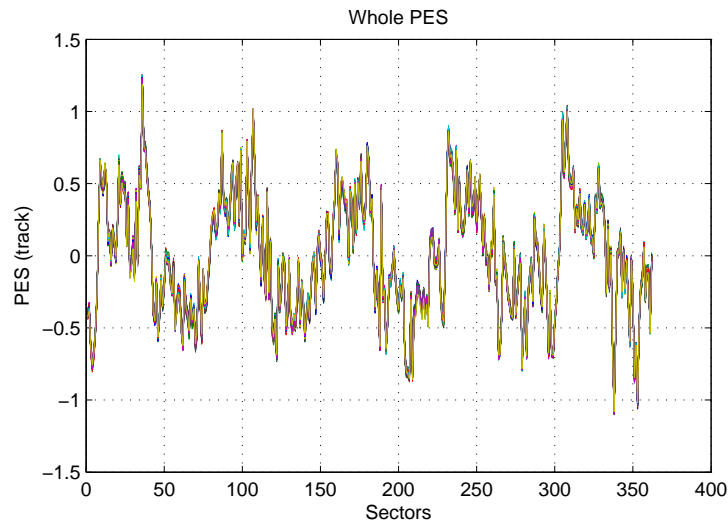


Figure 2.7: PES for 90 revolutions

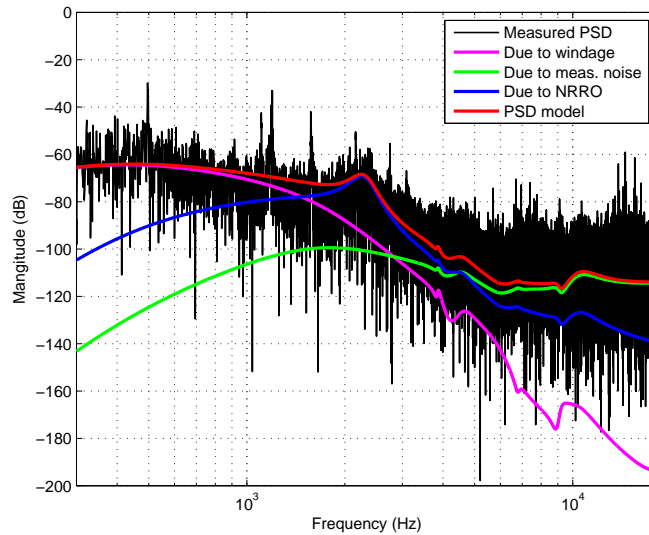


Figure 2.8: Total PSD, and PSD due to windage, measurement noise and NRRO

## 2.6 DSA Track-Following Control Design

One of the main characteristics of a dual-stage controller in HDDs is that there are two control outputs but there is only one position feed-back signal available that includes the contribution of both actuators. The relative displacement between the two actuators is not measured in an actual disk drive. Several different control design techniques for dual-stage actuators have been developed in recent years [19, 46, 47].

As mentioned in Chapter 1, servo control techniques play a vital role in increasing areal density by providing positioning algorithms which results in higher track per inch (TPI). Here, through an example, the limitation of the current commercial HDDs' performance is demonstrated. In this example a well known classical controller design such as sensitivity decoupling method (SDM) and lead lag controller are used which is currently used by industry in the dual stage HDD. Next, a simulation case study is conducted using a new secondary actuator designed in IMRE/NUS and on a commercial drive to predict the achievable TPI. An appropriate sampling rate needed to achieve  $10 \text{ Tb/in}^2$  areal density.

### 2.6.1 Sensitivity Decoupling Method

There are several techniques for designing dual-stage track-following controllers, which involve a form of decoupling control and sequential designs of multiple SISO compensators. The SDM [48, 49] allows a separate controller design for the VCM and the PZT. The control structure for dual-stage controller's design using this method is shown in Fig. 2.9.  $G_{VCM}$  and  $G_{PZT}$  are the VCM and PZT model transfer functions,

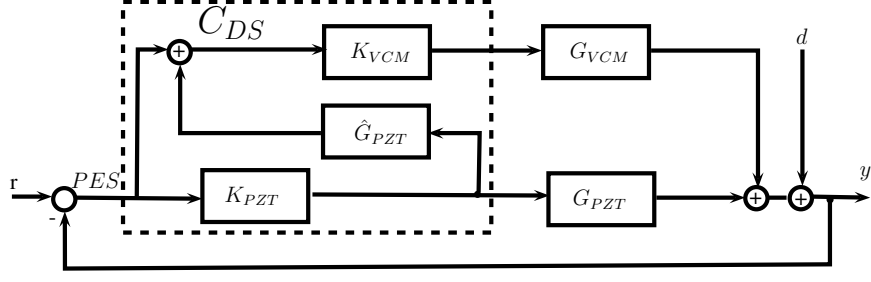


Figure 2.9: Block diagram of the track-following controller design.

respectively.  $K_{VCM}$  and  $K_{PZT}$  are the  $VCM$  and  $PZT$  loop controllers, respectively.

PES represents the motion of the head relative to the center of data track, while  $y$  is respectively the absolute position of the head. For most PZT actuated suspensions, the estimate of PZT displacement can be obtained by multiplying the PZT control input with the simplified PZT model,  $\hat{G}_{PZT}$ , as show in Fig. 2.9. The sensitivity function  $S_T = \frac{y}{d}$  of the overall system is shown in (2.9).

$$S_T = \underbrace{\frac{1}{1 + K_{MA}G_{PZT}}}_{S_{PZT}} \underbrace{\frac{1}{1 + K_{VCM}G_{VCM}}}_{S_{VCM}} \quad (2.9)$$

where  $G_{(VCM,PZT)}$  and  $K_{(VCM,PZT)}$  represent the plant dynamics and the controller for both actuators, respectively. A coupling factor  $K$  is defined by

$$K = \frac{1 + K_{MA}\hat{G}_{PZT}}{1 + K_{MA}G_{PZT}} \quad (2.10)$$

where  $\hat{G}_{PZT}$  is a model of the PZT actuator. An obvious choice for  $\hat{G}_{PZT}$  would be the 4th order model depicted in Fig. 2.4. However, to limit the complexity of the controller,  $\hat{G}_{PZT}$  is approximated by a simple DC gain  $g_{PZT}$ . The higher frequency resonance modes of the PZT do not have a significant impact on  $S_{VCM}$  because of

a high frequency roll-off that is included in  $K_{VCM}$ . Hence,  $K \approx 1$  and both control loops can be decoupled and designed separately. The overall controller of the system can be reformulated as (2.11).

$$C_{DS} = \begin{bmatrix} (1 + g_{pzt}K_{MA})K_{VCM} \\ K_{MA} \end{bmatrix} \quad (2.11)$$

### 2.6.2 Controller Design Results

The sampling frequency is chosen to be  $36.4 \text{ kHz}$  for both the VCM loop and the PZT loop which are identical to original sampling rate of the drive. Fig. 2.10 and Fig. 2.11 show the designed controller and sensitivity function for the VCM and PZT loop. For the VCM loop, the gain cross over frequency is designed to be at  $700 \text{ Hz}$ . The resulting gain margin and phase margin are  $11.7 \text{ dB}$  and  $50.7^\circ$ , respectively. Thereafter, the PZT controller  $K_{PZT}$  is designed as a band pass filter including 3 notch filters to suppress the PZT-actuator resonance mode. The gain crossover frequency is designed to be at  $3 \text{ kHz}$ . The resulting gain margin and phase margin are  $7.3 \text{ dB}$  and  $61^\circ$  respectively. The designed VCM and PZT controller,  $K_{VCM}$  and  $K_{PZT}$ , are used in the block diagram of the dual-stage control system in Fig. 2.10. The gain crossover frequency, gain margin and phase margin are respectively  $2.01 \text{ kHz}$ ,  $7.7 \text{ dB}$  and  $41^\circ$ .

The PES test is important in designing HDD servo system as it's  $3\sigma$  value is directly related to best achievable track density of HDDs. Table 2.4 show use the result of the PES tests for the servo system with different design controllers and sampling rate. It should be mentioned that for each design a number of iteration

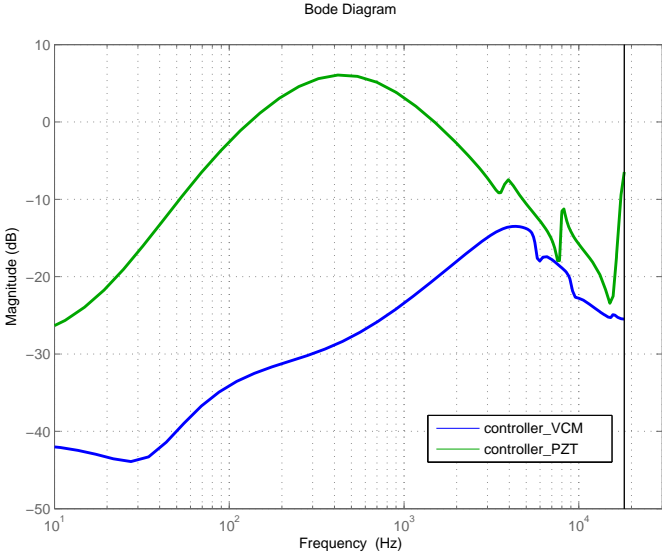


Figure 2.10: Controller frequency for VCM and PZT

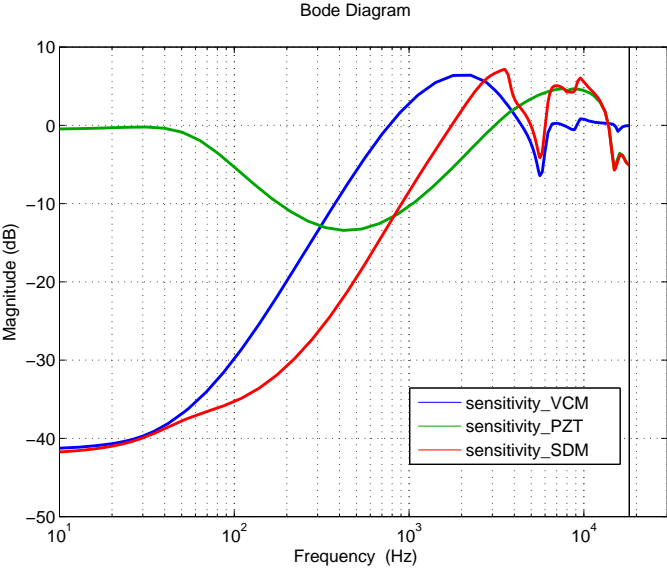


Figure 2.11: Frequency of sensitivity function

Table 2.4: The result of the designed controller designed for a commercial HDD with different sampling rates

SensingRate (kHz)	$3\sigma$ PES (nm)	Controller Band width(kHz)
36.4	8.39	2.01
60	7.97	2.69
80	7.15	3.16

have been done to achieve the best possible performance. The  $3\sigma$  values for 36.4 kHz is 8.39 nm. By increasing the sampling rate to 60 kHz and 80 kHz the servo bandwidth would increase to 2.69 kHz and 3.16 kHz respectively which causes the improvement of the controller accordingly. The best achievable  $3\sigma$  value among all design is achieve at 80 kHz but it is not sufficient to achieve 2200 kTPI ( $3\sigma=1.16$  nm ).

### 2.6.3 Actuated Slider to Achieve a High Bandwidth

As can be seen in the Fig. 2.4 for current PZT actuator, the natural frequency of the first resonant mode is at about 5 kHz. It is very difficult to push the open loop servo bandwidth higher than 5 kHz, even with increased sampling rates. The type of secondary actuator, which is currently used in the HDD, is actuated suspension. In this structure, two piezoelectric elements are attached to each carriage arm. One of the key limitations of this actuated suspension is that the excitation of suspension modes in appears in the output of the PZT actuator. To address this problem, the PZT element can be moved closer to the head-gimbal assembly (HGA) and only the



HGA is moved during actuation. The actuator can be placed between suspension and slider. In theory this kind of actuators can have a clean dynamic response up to 100 kHz. This makes the PZT elements smaller and the head off-track motion can be generated by the PZT actuator more directly.

In this section, based on preliminary experimental results from an actuator, which designed in the IMRE/NUS, the feasibility to reach to 10 *Tbit/Inch*<sup>2</sup> is evaluated. This actuator is actuated slider type and the design targets are described as follow.

- Highly miniaturized:  $\leq 0.21mm^3$
- Maximum displacement:  $\geq 30nm$
- Actuator resolution:  $\leq 0.1nm$
- Resonant frequency:  $\geq 30kHz$  (or even  $50kHz$ )

The experimental frequency response of the micro-actuator is shown in Fig. 2.12. In this experiment, the actuator is clamped on a rigid iron bar and actuated with a sweep sine wave. The displacement of the actuator is measured by an LDV. The model is identified based on the measurement result. A simulation runs based on the dynamic of the claimed actuator to evaluate the limit of the performance. It has to be mentioned that it is too optimistic to assume that installation does not affect the dynamic of the actuator. The main resonant mode of the actuator is located at  $85kHz$  with an almost flat response till  $40kHz$  which makes it easy to control. As such, extremely high bandwidth servo control can be realized using this micro-actuator as a secondary actuator. Different sampling rate and controller design are

Table 2.5: Controller designed results of NUS/IMRE micro-actuator with different sampling rates

Sensing Rate (kHz)	$3\sigma$ PES (nm)	Controller Band width(kHz)
36.4	3.28	3.51
60	1.73	4.89
80	1.11	5.81

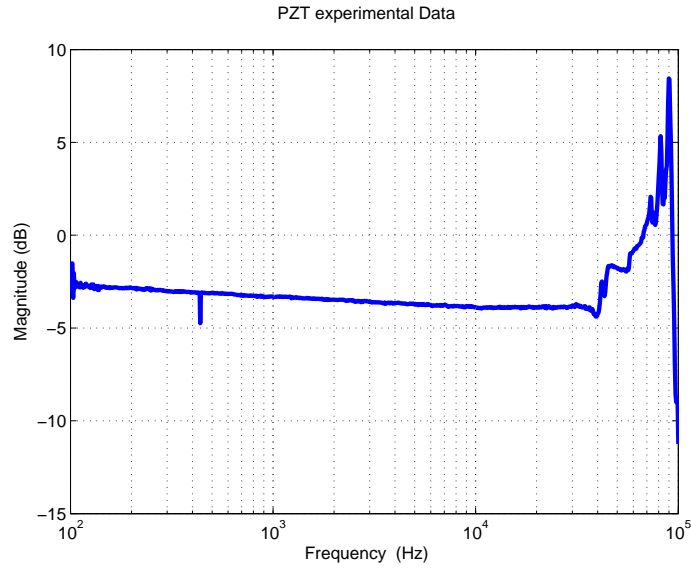


Figure 2.12: Experimental measurement of the frequency response of designed PZT used and their results are presented in Table. 2.5. The sampling rate increases from 40  $kHz$  to 80  $kHz$  and the dual stage controllers are redesigned in MIMO configuration, using a probabilistic method which will be described in chapter 4. Fig. 2.13 shows the sensitivity function of the controllers with different sampling rates. By using a sampling rate of 80  $kHz$ , the open loop bandwidth can be increased up to 5.81  $kHz$ , while the phase margin is  $68^\circ$  and gain margin is  $7.02dB$  and  $3\sigma$  of the controller is 1.11  $nm$ . Based on this simulation result, the required performance of the 10  $Tbit/inch^2$  is achievable by using this actuator and sampling rate of 80 $kHz$ .

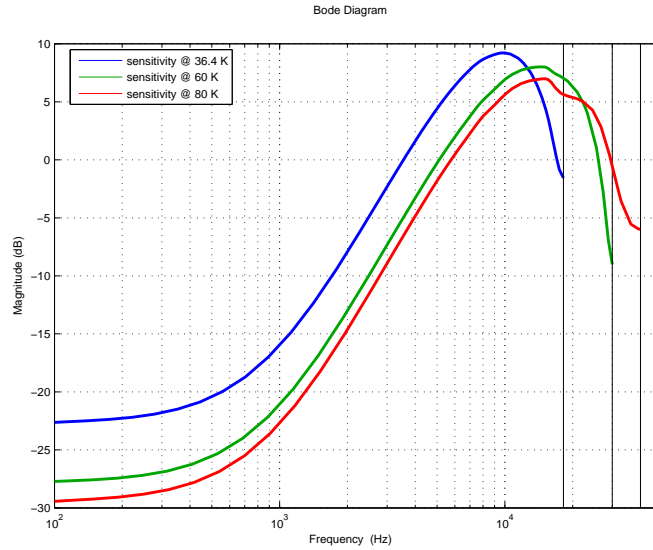


Figure 2.13: Sensitivity of the simulation results for IMRE/NUS micro-actuator

## 2.7 Conclusion

In this chapter, we consider a modeling of the dual actuator for hard disk drive servo systems. Parametric modeling of nominal model is presented along with the method to find the uncertainty of these parameters. The different source of disturbance is identified and modeled using of the PES of a commercial HDD. Obtained transfer functions and disturbance model is used in following chapters to design the controllers for the simulations and real-time implementation. A simulation case study is conducted using a prototype new secondary actuator which designs in IMRE/NUS to analyze the achievable TPI. Based on this simulation, it seems that with appropriate choosing of the sampling rate this type of secondary actuator is a good candidate to achieve  $10 \text{ Tb}/\text{in}^2$  areal density.

# Chapter 3

## Integral Resonant Control to Suppress Micro-Actuator Resonance

### 3.1 Introduction

Actuator resonance is a major issue hindering positioning precision in micro- and nano-positioning systems operating at high speed [3]. The loss of precision is generally not significant if the system bandwidth is kept sufficiently below the lowest frequency of actuators resonant modes. However, the demand for increasing accuracy and precision forces the designers to push the bandwidth as high as possible and the resonant modes become obstacles to achieving the target.

One possible solution to this limitation is to use a notch filter in cascade with the actuator driver so that the gain is heavily reduced at the resonant frequency. This

method has been widely used in head positioning HDDs [15, 18–20]. However, the notch filter creates rapid changes of phase near resonant frequencies leading to degradation in phase margin and robustness. The solution using notch filter is also sensitive to variations in resonant mode parameters of actuator. Implementing such a filter with fixed notch frequencies also do not consistently yield good performance as, due to manufacturing tolerance, discrepancies in the resonance frequency exists even in the same batch of mass produced actuators. Such shortcoming can be overcome by using, say, an adaptive notch filter [21, 22]. However, the order of the notch filter transfer function becomes very large if we have to suppress several resonant modes; causing, in turn, an increase in computational complexity for implementing the adaptive algorithm. Some researchers have used an adaptive mechanism without explicit use of a notch filter [23] but again at the cost of increased complexity in design and implementation.

In many systems, the sampling frequency is fixed by hardware constraints and the servo designer does not enjoy the liberty of choosing any arbitrarily high sampling frequency. The head positioning servomechanism in HDD units is an example of systems with sampling restriction. In such case, if a resonant mode exists near the Nyquist frequency, the digital realization of notch filter fails to be effective in suppressing that resonance. Multi-rate realization of the notch filter is a possible solution in those cases [24]. It can also be noted that the authors of [25] used another approach to suppress actuator vibration by properly shaping the input signal such that the actuator output remains vibration-free. However, the method requires an accurate model of the actuator, and robustness is compromised when servo control is to be designed

for mass-produced actuators.

Unlike all the solutions mentioned above, which are implemented in cascade, there are methods that use feedback compensation with sensors, e.g., strain gauge, accelerometer, etc.; and the sensor signals are used to generate the feedback signal. These active methods for controlling resonant vibrations of flexible machine components have always been an important area of research. However, direct measurements of displacement and velocity at an arbitrary location are impractical in real-life problems due to the difficulty in finding a suitable inertial frame of reference. An accelerometer can provide an inexpensive and reliable means of measuring the acceleration of the vibrating element, and hence the methodology of delayed acceleration feedback became a practical solution as described in Ref. [50]. A SISO delayed-acceleration feedback controller to mitigate free multi-mode vibrations of a flexible cantilever beam was proposed in [51] in which one sensor and one piezoelectric actuator are used to reduce vibrations of a flexible cantilever beam. Vibration feedback was also applied in suppressing resonance in HDD actuator units in the work reported in Refs. [52–54]. However, the use of an additional sensor is not practical in some applications. An additional sensor not only incurs cost, it may also have an undesirable loading effect as these micro-actuators are very small in size. In micro- and nano-positioning systems where position feedback is already available, we can do away with the additional sensor if the position feedback can be used to dampen the vibration modes. This approach resulted in the so called positive position feedback (PPF) control [55, 56]. Limitations of this method are: (i) the sensor must be collocated or nearly collocated with the actuator and (ii) it is difficult to tune the controller for suppression of multi-

ple modes. Another feedback-based active damping method is resonant control Pota et al. [57], which is high-pass in nature and hence not desirable in some applications as it amplifies sensor noise. Additionally, the approach of integral resonant control (IRC), proposed in [58], adds high frequency roll-off and thus removes the shortcoming of the resonant control of [57]. The IRC controller was successfully applied to a piezoelectric tube actuator for fast nano-scale positioning [59, 60], vibration reduction and precise tip-positioning of a flexible manipulator [61], etc. Further, in [62], damping of piezoelectric tube scanner is achieved by self sensing, i.e., by connecting the piezoelectric tube (actuator) in a capacitive bridge circuit to measure scanner oscillation. The work presented in this chapter applies IRC, in a new development, to suppress resonance of a piezoelectric (PZT or Lead Zirconate Titanate) micro-actuator used in dual-stage actuation for HDD units.

The structure of this chapter is as follows. Section 2 provides an introduction to the IRC and shows the steps used to design the compensator for a piezoelectric micro-actuator. As the full elaborate explanation on the IRC scheme can be found in the published literature [58–61], we merely include a brief description here for the sake of completeness. Section 3 presents the dynamics of the piezoelectric micro-actuator used in the HDD head positioning system, the design objectives and the IRC compensator designed. The effectiveness of the compensator in suppressing resonant modes is illustrated using simulation as well as practical implementation. A suitably concise description of the implementation platform is also given. Finally, some concluding comments and plans for future work are stated in the last section.

## 3.2 Integral Resonant Control: An Overview

The principle of operation of the IRC compensator can be explained using the block diagram in Fig. 3.2a. The transfer function  $G(s)$  in this diagram represents the dynamics of the PZT micro-actuator that shows plurality of lightly damped vibration modes and can be described, for  $M$  such modes, as 3.1

$$G(s) = \sum_{i=1}^M \frac{A_i}{s^2 + 2\zeta_i\omega_i s + \omega_i^2} \quad (3.1)$$

This transfer function has  $M$  pairs of complex conjugate poles, each pair for one resonant mode, and  $(M-1)$  pairs of complex conjugate zeros.

The feed-through term ( $D_f$ ) in the IRC Fig.3.2.a is a constant. The difference between plant output and the output of the feedthrough block is fed back through the controller  $C(s)$  in order to increase damping of the vibration modes. The objective is to determine the feed-through term  $D_f$  and the controller  $C(s)$  such that damping factors of the resonant modes are increased. The external input  $r$  is the actuating signal for the micro-actuator  $G(s)$ , which is generated by an outer loop for position control. An equivalent realization of the same compensator in conventional feedback structure is shown in Fig.3.2.b; the equivalent controller  $C_C(s)$  is derived from the IRC configuration of Fig.3.2.a and is given as

$$C_c(s) = \frac{-C(s)}{1 - D_f C(s)} \quad (3.2)$$



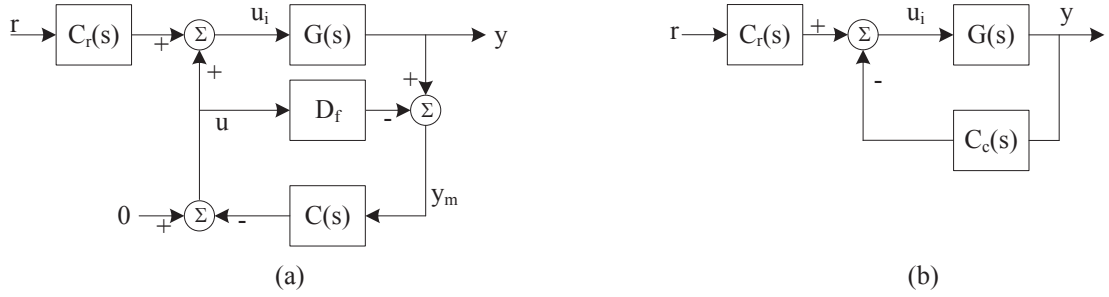


Figure 3.1: Compensator in IRC configuration (a) and in conventional feedback configuration (b)

The transfer function  $C_r(s)$  can be used to compensate for change in DC gain, if any, due to the inclusion of IRC. Moreover, it can be used to provide high frequency roll-off if the resonant modes at very high frequencies are not adequately damped by the IRC alone. In the present work, this filtering effect of  $C_r(s)$  is not used and we use a constant to compensate the change in DC gain.

### 3.3 Effect of Feed-through Term $D_f$

An augmented system  $G_m(s) = G(s) - D_f$  is formed by the feedthrough term  $D_f$ . Poles of  $G_m(s)$  are same as the poles of  $G(s)$  but has more zeros than  $G(s)$ . Let the transfer function  $G(s)$  of the micro-actuator have  $M$  pairs of lightly damped complex conjugate poles and  $M - 1$  pairs of complex conjugate zeros. It can be said intuitively that a zero appears at a frequency between two adjacent pole frequencies. It was proven analytically in [58] for transfer function with poles on the imaginary axis, i.e.,  $G_3(s) = \sum_{i=1}^M \frac{A_i}{s^2 + \omega_i^2}$  for  $A_i > 0$ . That analysis can be extended to plants with non-zero damping factor or resonant modes modeled by stable complex poles [58]. The

$i$	$A_i$	$\omega_i(\text{rads})$	$\zeta_i$
1	$0.1698 \times 10^9$	$2\pi(6.669 \times 10^3)$	0.0185
2	$0.4779 \times 10^9$	$2\pi(10.862 \times 10^3)$	0.0438
3	$0.9394 \times 10^9$	$2\pi(14.136 \times 10^3)$	0.0460

Table 3.1: Parameters used for illustration of frequency of under damped zeros.

proof is not included in this chapter. Rather we show the pole-zero map of a specific case of plant with three lightly damped resonances, i.e.,  $G_3(s) = \sum_{i=1}^M \frac{A_i}{s^2 + 2\zeta_i\omega_i s + \omega_i^2}$ ; parameters of the model are given in the table below (see Tab. 3.1). Two zeros of  $G_3(s)$  are at  $\omega_{z,1} = 2\pi(7.507 \times 10^3)\text{rad/s}$  and  $\omega_{z,2} = 2\pi(12.140 \times 10^3)\text{rad/s}$ , respectively. It shows that  $\omega_1 < \omega_{z,1} < \omega_2$  and  $\omega_2 < \omega_{z,2} < \omega_3$ , i.e., the frequency of a zero of the transfer function lies between frequencies of two adjacent poles. Bode magnitude plot of  $G_3(s)$  is also shown in Fig. 3.7. Experimental frequency response shown in §3.4.1 conforms to this argument.

When the transfer function  $G(s)$  with  $M$  pairs of complex conjugate poles and  $(M-1)$  pairs of complex conjugate zeros is augmented with the parallel feed-through term ( $D_f$ ), the transfer function of the augmented system is 3.3

$$C_m(s) = G(s) - D_f = \frac{P(s)}{Q(s)} - D_f = \frac{P(s) - D_f Q(s)}{Q(s)} \quad (3.3)$$

The poles of  $G_m(s)$  are identical to the poles of  $G(s)$ . But the augmentation modifies the locations of the zeros and increases the number of complex conjugate zeros by a pair. By selecting  $D_f$  appropriately, we can place this additional pair of zeros at a desirable location. In IRC design, the parameter  $D_f$  is selected in a way such that the zero is introduced at a frequency lower than the lowest resonant frequency. Lets

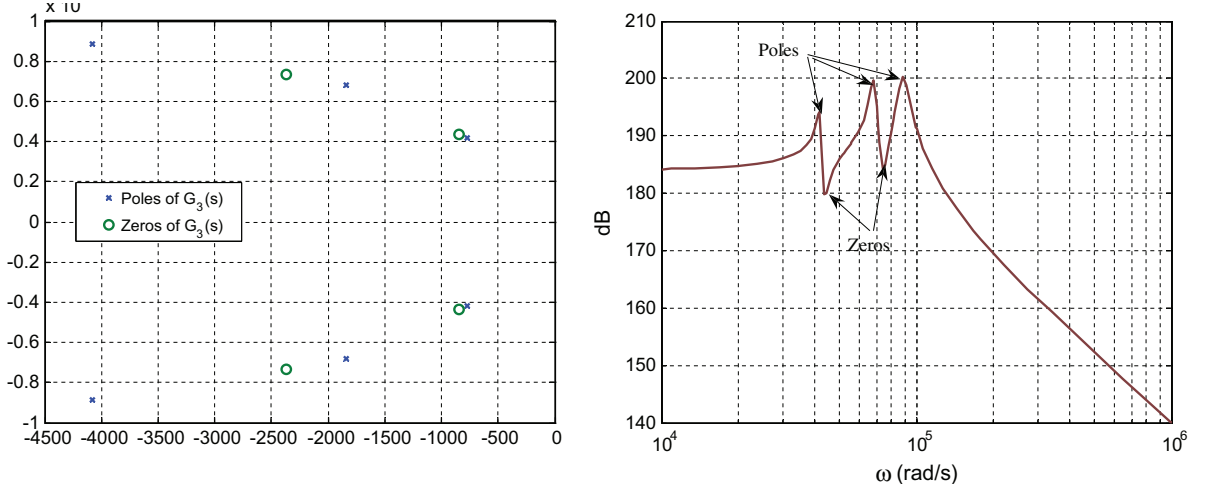


Figure 3.2: Pole-zero map (left) and Bode magnitude plot (right) of micro-actuator with three resonant modes

illustrate the idea using the nominal second order model of micro-actuator  $G_2(s) =$

$$\frac{K_{dc}\omega_p^2}{s^2 + 2\zeta\omega_p s + \omega_p^2}.$$

Two poles of  $G_2$  are at  $p_{1,2} = -\zeta\omega_p \pm j\omega_p\sqrt{1 - \zeta^2}$  and the DC gain of the micro-actuator is  $K_{dc}$ . After augmentation, the modified transfer function is 3.4

$$\begin{aligned} G_{2,m}(s) &= \frac{K_{dc}\Omega_p^2 - D_f(s^2 + 2\zeta\Omega_p s + \omega_p^2)}{s^2 + 2\zeta\Omega_p s + \omega_p^2} \\ G_{2,m}(s) &= -D_f \frac{s^2 + 2\zeta\Omega_p s + \omega_p^2(1 - \frac{K_{dc}}{D_f})}{s^2 + 2\zeta\Omega_p s + \omega_p^2} \end{aligned} \quad (3.4)$$

Denominator and hence the poles  $G_m(s)$  and  $G(s)$  are identical. In addition,  $G_m(s)$  has two zeros located at  $z_{1,2} = -\zeta\omega_p \pm j\omega_p\sqrt{(1 - \frac{K_{dc}}{D_f}) - \zeta^2}$ . These zeros are complex if the condition  $(1 - \frac{K_{dc}}{D_f}) > \zeta^2$  is satisfied. The real part of the zeros is the same as the real part of the poles. One can choose  $D_f$  such that the imaginary part of the zero is smaller in magnitude than the imaginary part of the poles, i.e., damping factor of

zeros is larger than  $\zeta$  Let,

$$\sqrt{\left(1 - \frac{K_{dc}}{D_f}\right) - \zeta^2} = \alpha\sqrt{1 - \zeta^2}, \text{ where } \alpha < 1. \quad (3.5)$$

$$1 - \frac{K_{dc}}{D_f} - \zeta^2 = \alpha^2(1 - \zeta^2)$$

The parameter  $\alpha$  has a physical interpretation in terms of the placement of zero. We use  $\alpha$  as the design parameter instead of  $D_f$ . If one chooses the feed-through term  $D_f$  according to the above equation, the complex zeros will have higher damping than the poles. The feed-through term  $D_f$  satisfying the condition of Eq. 3.5b is,

$$D_f = \frac{K_{dc}}{(1 - \alpha^2)(1 - \zeta^2)} \quad (3.6)$$

As  $0 < \zeta < 1$ ,  $0 < \alpha < 1$  and  $K_{dc} > 0$  the feed-through term  $D_f$  is positive real.

### 3.3.1 Choice of $C(s)$

Closed loop poles of the compensated system are the roots of  $1 + C(s)G_m(s)$ . Several choices of the controller  $C(s)$ , for example, direct integral control  $C(s) = -\frac{K}{s}$ , leaky integrator  $C(s) = -\frac{K}{(s+p)}$ , or a constant  $C(s) = K$ , etc. have been suggested in [58] to implement IRC. The use of constant gain as  $C(s)$  is equivalent to positive position feedback (PPF) control. In our work, we use the leaky integrator, i.e., a real axis pole as the controller.

The characteristic equation for the nominal 2nd order model with leaky integrator as

controller is, Eq. 3.7

$$1 + K \frac{-D_f(s^2 + 2\zeta\Omega_p s + \omega_p^2(1 - \frac{K_{dc}}{D_f}))}{(s + p)(s^2 + 2\zeta\Omega_p s + \omega_p^2)} \quad (3.7)$$

In the equation,  $\zeta$ ,  $\omega_p$  and  $K_{dc}$  are parameters of the nominal 2nd-order model. The feed-through term  $D_f$  is determined according to Eq.3.6. We choose the real axis pole at a frequency smaller than the natural frequency of the dominant mode. The gain  $K$  of the controller can be found using standard design tools such as root locus, shown in Fig.3.3. In this figure,  $p_1$  and  $p_2$  are the poles of  $G_m(s)$ ,  $z_1$  and  $z_2$  are the zeros of  $G_m(s)$ , and the controller pole is placed at  $-p$ . With increasing controller gain, the complex conjugate poles initially move away from the imaginary axis and the damping increases until it reaches a point of maximum damping. Further increase in gain beyond that point pushes the poles towards imaginary axis and damping is reduced. We can select the gain where the damping reaches its maximum for the chosen values of  $D_f$  and  $p$ . Two loci originating from the poles of  $G_m(s)$  eventually terminate (for  $K = \infty$ ) at the zero introduced by feed-forward augmentation. The imaginary part of these zeros is directly related to the design parameter,  $\alpha$ . Smaller the value of  $\alpha$  we choose, further the zeros are placed from the poles. This means that smaller value of  $\alpha$  allows the poles to be shifted further away from the imaginary axis resulting in greater damping as illustrated in Fig. 3.4.

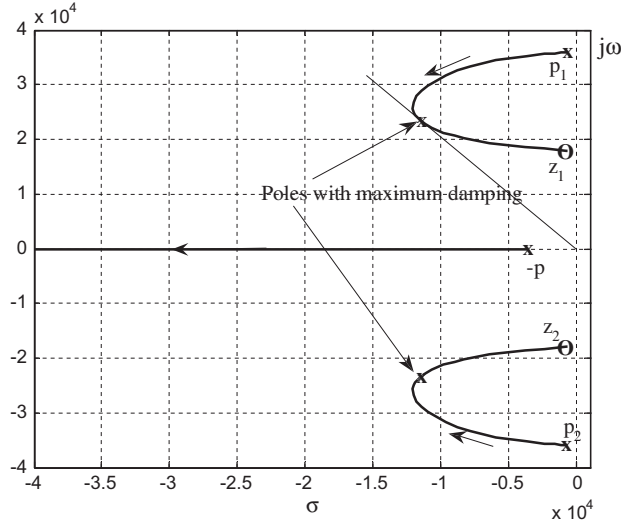


Figure 3.3: Root locus with leaky integrator for the nominal plant model

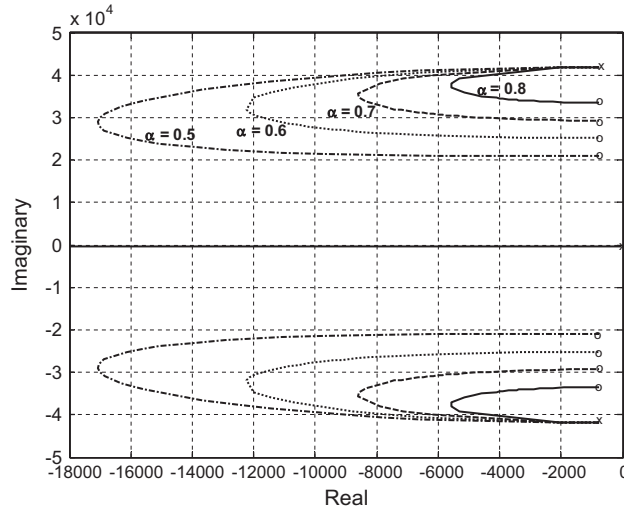


Figure 3.4: Root locus with leaky integrator for the nominal plant model

### 3.3.2 IRC Design for Micro-Actuator with Multiple Resonant Modes

For actuators with multiple resonant modes, we consider the lowest frequency resonant mode, i.e., a nominal 2nd-order model to design the IRC compensator. The feed-through term  $D_f$  is obtained using  $D_f$  EQ. 3.6, where  $\zeta_1$  is the damping coefficient

of the first resonant mode and  $K_{dc}$  is the DC gain of the nominal model. The same reduced order nominal model is used for the root locus approach to find the gain  $K$ . In this simplified approach, the compensator is designed to improve the damping of the lowest frequency resonant mode only. The PZT micro-actuator used in the present work has five resonant modes of large amplitude. After augmentation, the transfer function  $G_m(s)$  has five pairs of complex poles and five pairs of complex zeros. According to the root locus analysis, the loci starting at the complex poles will terminate at the complex zeros and the locus starting at the pole of  $C(s)$  will move along the negative real axis. As the IRC parameters are chosen to increase the damping of the first resonant mode, it does not guarantee increased damping of the high frequency modes. However, the real axis pole of the IRC contributes to high frequency roll-off attenuating those modes.

Design steps:

- 1) Select design parameter  $\alpha$  ( $0 < \alpha < 1$ ) and determine the feedthrough term using Eq. 3.6.
- 2) Obtain the modified transfer function  $G_m(s) = G_2(s) - D_f$  where  $G_2(s)$  is the nominal 2nd order transfer function representing only the first resonant mode. Its DC gain is equal to the DC gain of the original micro-actuator model  $G(s)$ .
- 3) Express the chosen controller  $C(s)$  in the form of  $C(s) = -K\bar{C}(s)$  and define the open loop transfer function as  $L(s) = -K\bar{C}(s)G_m(s)$ .
- 4) Determine the value of gain  $K$  using root locus.

### 3.3.3 Inclusion of Command Input for the Micro-Actuator

In order to realize micro- or nano-positioning system, the IRC compensated micro-actuator is to be controlled by a command input from the outer loop position control system. The DC gain from the external input to the output of micro-actuator compensated with IRC may differ from the DC gain of the uncompensated micro-actuator. The DC gain can be adjusted using a feed-forward block  $C_r(s)$  shown in Fig. 3.2b. If the high frequency roll-off contributed by the IRC is not sufficient, a low-pass filter may be included in the feed-forward block, i.e.,

$$C_r(s) = K_f \frac{\omega_{p1}}{s + \omega_{p1}} \quad (3.8)$$

The gain  $K_f$  is chosen to adjust the DC gain and  $\omega_{p1}$  to increase overall high-frequency roll-off, if required. Closed loop transfer function from command input  $r$  to the micro-actuator output  $y$  (Fig. 3.2b) is,

$$C_{yr}(s) = C_r(s) \frac{G(s)}{1 - G(s)C_c(s)} \quad (3.9)$$

For IRC using leaky integrator, the controller  $C_c(s)$  is  $C_c(s) = \frac{-K}{s+p+KD_f}$ .

### 3.3.4 IRC for Suppression of Micro-Actuator Resonance in Dual Stage Actuator

The applicability of this approach is also investigated in suppressing the secondary stage resonance in HDD servomechanisms which use a dual-stage actuator with voice



coil motor (VCM) as the primary stage, and piezoelectric micro-actuator as the secondary. As stated in chapter 2 the sensitivity decoupling design method (SDM) [63] allows a separate controller design for the VCM and the PZT. In this section an extended version of SDM is used for dual-stage controller design with IRC in the secondary loop.

Drawing inspiration from the original idea of SDM, Fig. 3.5 shows a block diagram of the dual-stage controller design using the extended sensitivity decoupling method (ESDM). The new architecture is extended in such a way as to decouple the sensitivity function in the presence of the integral resonant controller for the PZT actuator. The displacement of the PZT and VCM actuator is estimated using a simplified model  $\hat{G}_{PZT}$  and  $\hat{G}_{VCM}$  respectively. The closed-loop sensitivity transfer function  $S_T(z)$  (from  $r$  to  $y$ ) of the closed loop system in Fig. 3.5 is given by:

$$S_T = \frac{1}{1 + C_{VCM}(s)G_{VCM}(s)} \frac{1}{1 + C_{PZT}(s)G_{IMC}(s)} \quad (3.10)$$

where

$$G_{IMC}(z) = \frac{C_{FF}(s)G_{PZT}(s)}{(1 + (G_{PZT}(s) - D_f)C_{IMC}(s))} \quad (3.11)$$

Thus the block diagram in Fig. 3.5 can be rearranged to be its equal block diagram as shown in Fig. 3.6. As a result, the design of the dual-stage servo controller can be decoupled and designed separately: the VCM-loop sensitivity function,  $S_{VCM}(s)$ , is designed to compensate the lower frequency disturbances; and in the PZT loop, further disturbance attenuation is achieved by  $S_{PZT}(s)$ . The controller is consist of a

lead-lag compensator cascaded with two notch filters for the VCM. This design have a good error rejection in the low frequency as well as to increase the phase margin at the open-loop gain crossover frequency.

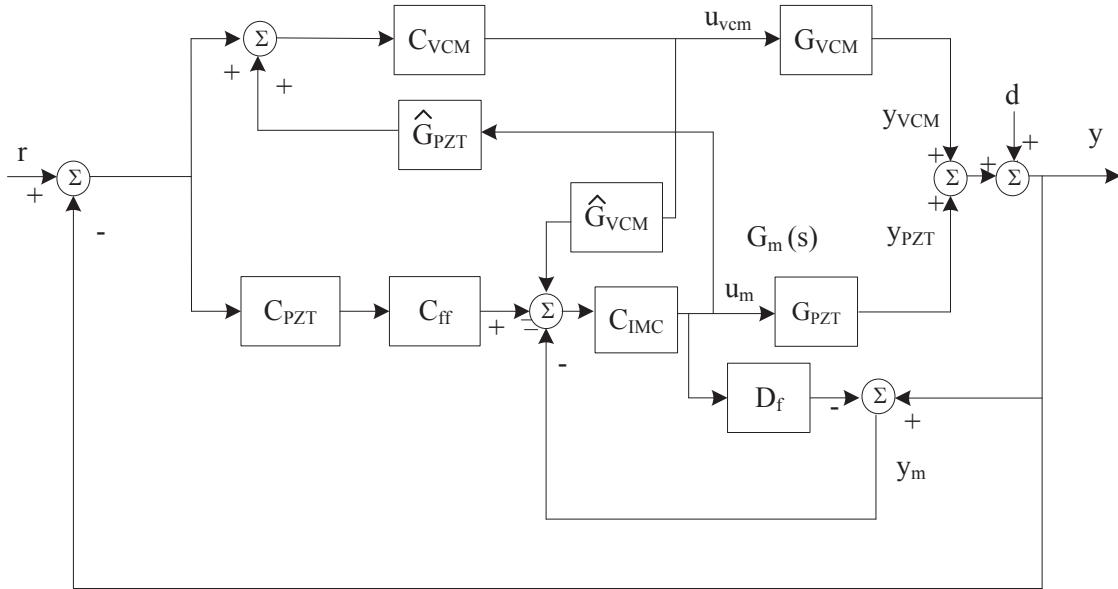


Figure 3.5: Block diagram of the PZT IRC controller design using the sensitivity decoupling method.

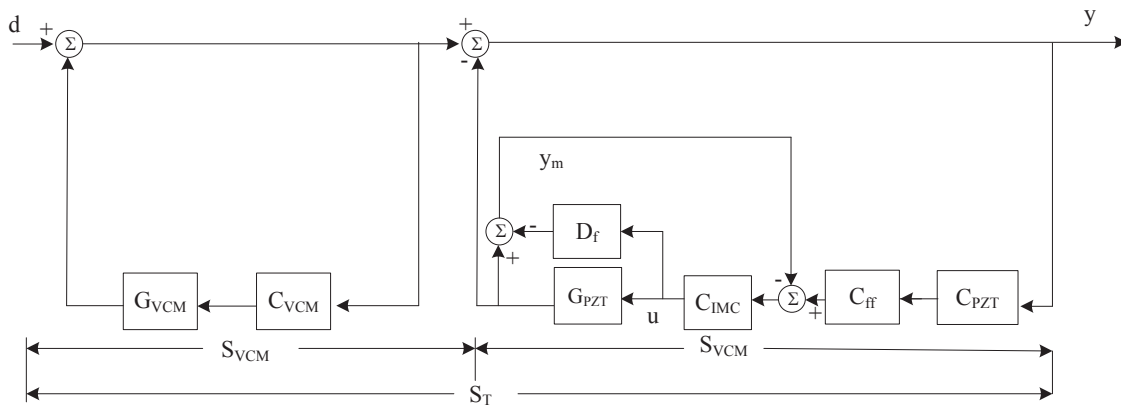


Figure 3.6: Equivalent sensitivity function block diagram.

## 3.4 Results

In this section, we present the results of frequency-domain and time-domain simulation of IRC compensated PZT micro-actuator. Through these results, we evaluate the effectiveness of the IRC in reducing residual vibration. Results from practical implementation are given at the end of this section.

### 3.4.1 Identification of PZT Micro-Actuator Model

The model of the micro-actuator of a commercially produced HDD is identified from its frequency response obtained using the experimental setup shown in Chapter 2.

For identification experiment, the swept sine signal and the measured displacement signal are fed to the two input channels of the DSA, which generates the frequency response of the system. The experimental response is shown in Fig. 3.7. The model identified from the frequency response data is given below which is used for design and all simulations presented in this Chapter,

$$G(s) = G_p(s)G_{pade}(s) = 10^9 \left( \frac{-s + 1.717 \times 10^5}{s + 1.717 \times 10^5} \right) \sum_{i=1}^5 \frac{A_i}{s^2 + 2\zeta_i \omega_i s + \omega_i^2} \quad (3.12)$$

In addition to modeling the five dominant resonant modes, the delay in the system is also modeled as a first order Pade function. Besides the experimental frequency response, Fig. 3.7 also shows the simulated frequency response of the micro-actuator model. The parameters of the resonant models are shown in Tab. 3.2. The frequency response shows a resonant mode with large magnitude at  $18.3kHz$ . In order to cancel this mode using a digital notch filter, one must choose sampling frequency

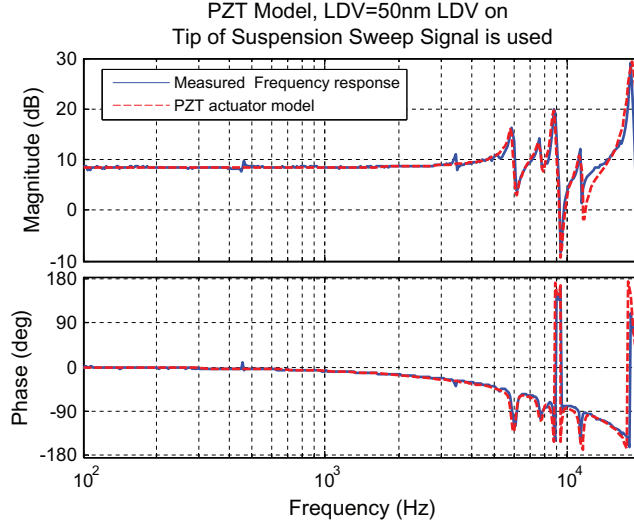


Figure 3.7: Measured frequency response of the PZT micro-actuator and the response of identified model.

$i$	1	2	3	4	5
$A_i$	0.28392	0.26991	0.93697	0.65432	22.47259
$\omega_i(\text{Rad}/s)$	$2\pi \times 5.87$	$2\pi \times 7.68$	$2\pi \times 8.8$	$2\pi \times 11.3$	$2\pi \times 18.3$
$\zeta_i$	0.02	0.02	0.015	0.02	0.02

Table 3.2: Parameters of the identified PZT micro-actuator model.

higher than  $36.6\text{kHz}$ . Unfortunately, the choice of sampling frequency in HDD is constrained by physical limitations of number of servo sectors per revolution and rotational speed of the disks. This physical limitation in HDD makes IRC attractive as an effective solution for suppression of resonance of the micro-actuator. It is shown in this chapter, using simulation and practical implementation, that IRC implemented with  $40\text{kHz}$  sampling suppresses sufficiently the resonances of the micro-actuator. It will be difficult to achieve similar performance using a notch filter implemented with the same sampling frequency. It should be noted that a notch filter will perform better if we are free to choose the sampling frequency arbitrarily high. Another advantage of IRC is its low order dynamics despite the presence of plurality of resonant modes. The

order of the notch filter compensator must be increased to compensate more number of flexible modes. We design a 10th-order notch filter to cancel all five resonant modes of the micro-actuator used in this work. The IRC approach, on the other hand, results in a 1st-order filter to achieve comparable performance.

### 3.4.2 Design and Evaluation of IRC Compensator for Secondary Actuator

The identified model of the PZT micro-actuator has its lowest resonant frequency at  $5870Hz$  with damping coefficient of 0.02 and a dc gain of 2.6297. Accordingly, the nominal model used in our design is,

$$\begin{aligned} G_2(s) &= K_{dc} \frac{(2\pi \times 5870)^2}{s^2 + 2 \times 0.02 \times (2\pi \times 5870)s + (2\pi \times 5870)^2} \\ &= \frac{2.6297 \times 1.36 \times 10^9}{s^2 + 1475s + 1.36 \times 10^9} \end{aligned} \quad (3.13)$$

We wish to place the zero at approximately half of this resonant frequency. Using  $\alpha = 0.5$ , we determine  $D_f$  according to Eq. 3.6 and found it to be  $Df \cong 3.28$ . The augmented transfer function is

$$\begin{aligned} G_2(s) &= \frac{2.6297 \times 1.36 \times 10^9}{s^2 + 1475s + 1.36 \times 10^9} - 3.28 \\ &= -3.28 \frac{s^2 + 1475s + 2.69 \times 10^8}{s^2 + 1475s + 1.36 \times 10^9} \end{aligned} \quad (3.14)$$

The effect of augmentation is shown in Fig. 3.8. Introduction of a pair of complex zeros at  $2.6kHz$  provides a phase lead. Without the negative sign, the phase would be zero at low frequency, increasing due to the anti-resonance and have phase lead

up to the resonance which gets the phase back to zero. Additional  $-180^\circ$  due to the negative sign in  $G_{2,m}(s)$  makes the phase of the augmented transfer function vary between  $-180^\circ$  and  $0^\circ$ . The same argument applies to the phase of  $G_m(s)$ , also shown in Fig. 3.8.

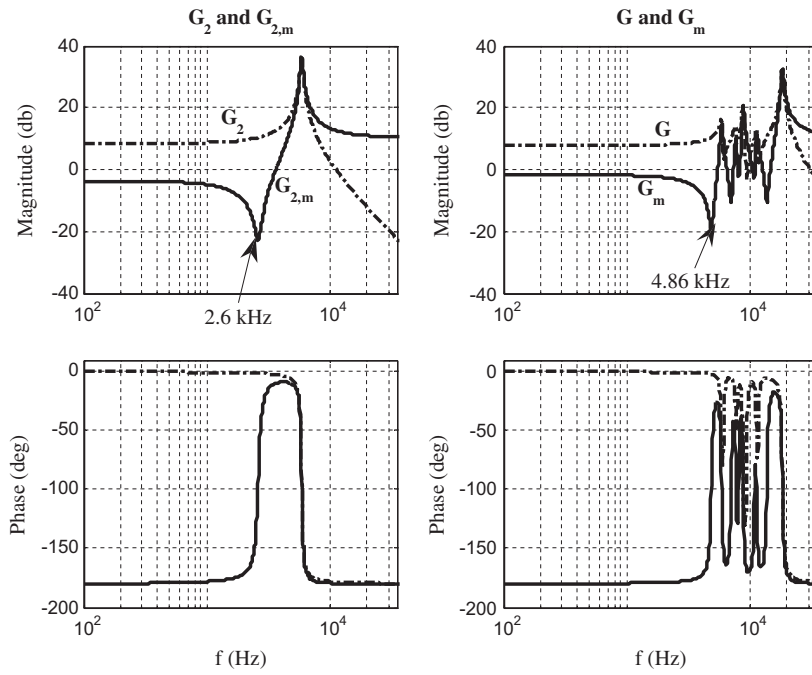


Figure 3.8: Effect of augmenting the transfer function with  $D_f$  in parallel.

When the micro-actuator model with all five resonant modes is augmented using the same value of  $D_f$ , a complex conjugate zero is introduced in the augmented transfer function  $G_m(s)$  at a frequency lower than the lowest resonant frequency. However, the frequency of the zero introduced is shifted upward to  $4.86\text{kHz}$  from  $2.6\text{kHz}$  obtained with the nominal model.

It should be noted that the phase of the modified transfer function,  $G_m(s)$  or  $G_{2,m}(s)$ , is bounded between  $-180^\circ$  and  $0^\circ$ . Any controller providing  $+90^\circ$  phase lead can

produce excellent phase margin and infinite gain margin. An integrator as IRC controller ( $C(s) = -\frac{K}{s}$ ) in negative feedback provides  $+90^\circ$  phase at all frequencies and a leaky integrator ( $C(s) = -\frac{K}{s+p}$ ) adds a phase lead of  $+90^\circ$  for  $\omega \gg p$ . We choose the leaky integrator with the real axis pole placed at  $p = -100$ , i.e., ( $C(s) = -\frac{K}{s+p}$ ). The gain  $K$  is obtained using root locus method. The Bode plots of the open loop transfer functions are shown in Fig. 3.9; the one on the left ( $G_{2,OL}$ ) is for the case with the second order actuator model while the one on the right ( $G_{OL}$ ) is for actuator model consisting of all resonant modes. The augmented transfer function has a constant gain at low frequency. The  $-20\text{db/decade}$  slope (shown by a dotted line on the magnitude plots) of the open loop transfer function is contributed by the IRC controller.

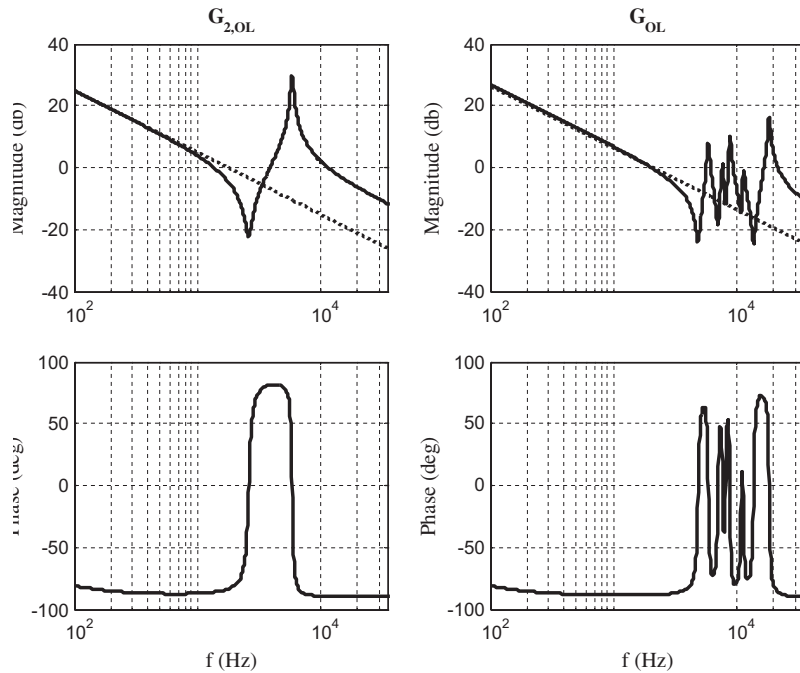


Figure 3.9: Bode plot of the open loop transfer function.

$i$	1	2	3	4	5
Resonant frequency $f_i(kHz)$	5.87	7.68	8.8	11.3	18.3
Attenuation (dB)/IRC without LPF	12.37	12.13	18.74	13.53	28.54
Attenuation (dB)/IRC with LPF	14.85	16.19	23.61	20.06	37.48

Table 3.3: Damping of the five modes of the micro-actuator.

Bode magnitude plot of the transfer function  $G_{yr}(s)$  is shown in Fig. 3.10. In this result, the  $C_r(s)$  of Fig. 3.2b is used for DC gain adjustment only; no low pass filter is included. The IRC compensator is designed to dampen the lowest frequency (5870 Hz) resonant mode. As seen in Fig. 3.10, damping factor is also increased for other high frequency modes but not as good as in the case of the mode at 5870Hz. The high frequency roll-off of the real axis pole in IRC also attenuates these modes. If the high frequency modes are not sufficiently attenuated, inclusion of low-pass filter (LPF) in  $C_r(s)$  is required. Attenuations of different resonant modes, with and without the LPF in  $C_r(s)$ , are given in Tab 3.3. The addition of LPF provides greater attenuation at the resonant frequencies. However, we have not used LPF in the simulation and experimental results presented in this chapter.

It is clear from Fig. 3.10 that the 10th-order notch filter performs better than IRC in suppressing the resonant modes. The main advantage of IRC lies in the simplicity in implementation and computational burden. We think that the IRC is less sensitive to parametric variations in resonant modes and have done some numerical investigations to assess the performance of IRC compensation in the face of such parametric variations. The evaluation done so far is still short of being comprehensive.

Step responses of the uncompensated micro-actuator, the micro- actuator compen-



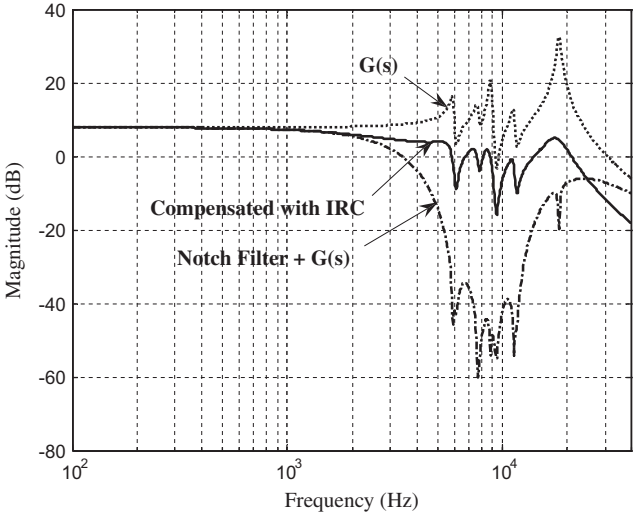


Figure 3.10: Simulated Bode (magnitude) plots of uncompensated and compensated micro-actuator.

sated with IRC and the micro-actuator with cascade notch filter are shown in Figs. 3.11 and 3.12. The response is smoother with the 10th-order notch filter than that with the IRC compensation, but the response with IRC is comparable.

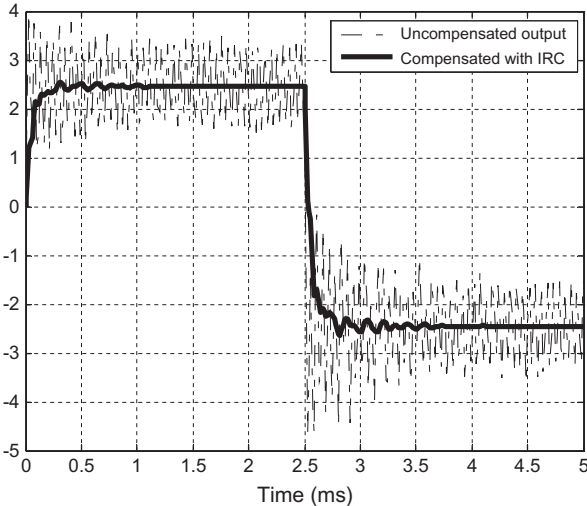


Figure 3.11: Simulated time-domain response of micro-actuator with and without IRC compensator.

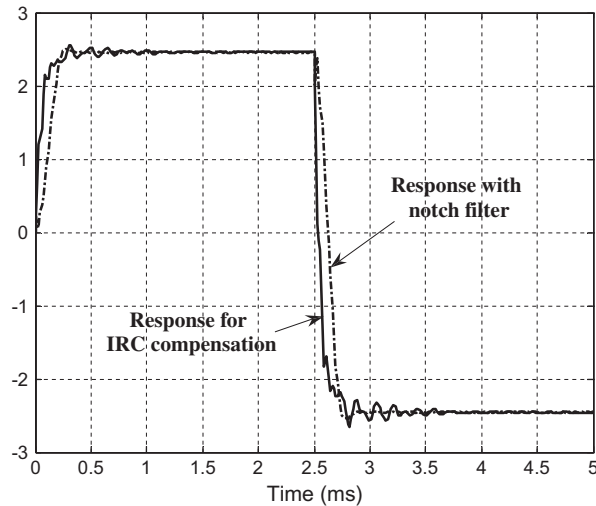


Figure 3.12: Comparison between simulated responses with IRC and with 10th-order notch filter.

### 3.4.3 Results for Dual-Stage Actuator

The simulation results presented in previous section are obtained using the PZT micro-actuator alone, in other word in a dual stage actuator this happened when the VCM actuator is clamped mechanically to eliminate its effect on the displacement of read/write head slider. In reality, the dual-stage actuator in HDD is a two-input single-output system where the displacement of the slider is sum of contributions from both actuators. While the present simplification used in the experiment reported in [64] serves to demonstrate the effectiveness of IRC in suppressing resonance it does not yet completely represent the true scenario of dual stage servomechanism of HDD. In our understanding, the displacement attributed to the VCM is significantly smaller during the track-following mode where the main control is exerted by the secondary stage. In this section the result of extension of the IRC approach developed and presented to a two-input single-output actuator used in HDD units.

The model of the VCM presented in chapter 2 is used for this simulation. For the

VCM, the notch filters are used to attenuate the first two resonance modes of  $5.5kHz$  and  $8.8kHz$ . The gain crossover frequency of the VCM transfer function is  $850Hz$ . The micro-actuator shows a dominant resonant mode at  $18.3kHz$ . So, we use  $40kHz$  sampling frequency is used to implement the notch filter, the IRC compensator and the controllers for VCM and PZT. The designed IRC controller is  $C(s) = K/(s+100)$  with  $D_f = 7.31$  and  $K = 2480$ . The sensitivity (S) and complementary sensitivity (T) functions of the closed loop are shown in Fig.3.13. We can see from this figure that the close loop bandwidth is around  $1.8kHz$ , which is an acceptable range for compensation of the RRO and NRRO disturbances.

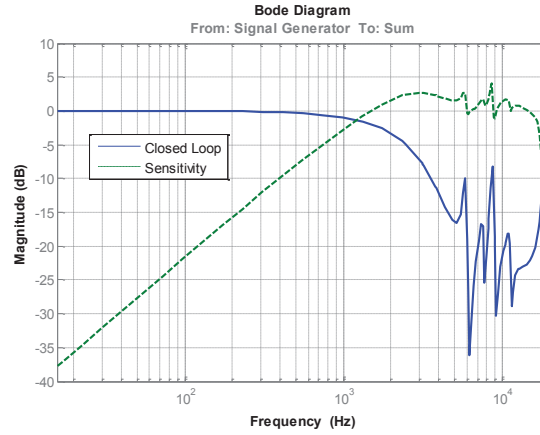


Figure 3.13: Sensitivity and complementary sensitivity function.

To further test the robustness of the designed controller, 500 randomly uncertain plants for the PZT actuator are chosen and the loop is closed for each of them. We have assumed the  $\pm 3\%$  to  $\pm 15\%$  percent variation for each resonance mode ( $\omega_n$ ) and the damping factor ( $\zeta_n$ ) in our simulation. Stability margins were computed when the loop is opened at the feedback point. Fig. 3.14 and Fig. 3.15 the nominal as well as worst-case stability margins for the designed controller in the range of mentioned

variation. Moreover, time domain analysis is also carried out to evaluate the robust performance of the IRC design in terms of the worst-case changes of the resonance characteristic of the PZT actuator. But first, we study the nominal performance of the system using the step change in the reference input. As can be seen in Fig. 3.16a, the output reaches the 5% error bound in 0.27 ms and the overshoot is only 3% as the VCM moves at a slower rate, but the quick motion of the PZT enables the output to reach the target in a fairly short time. Step responses with perturbations of micro-actuator dynamics are simulated by considering the worst-case variation of the nominal value. The result, as shown in Fig. 3.16b, proves that the closed loop remains stable and the worst-case performance meets the demand requirement. It should be mentioned that the main resonance mode at the frequency of  $18.3kHz$  contributes to a slight oscillation in the step response of the system. This oscillation can be reduced by adding a low pass filter in the PZT loop but it will make the system slower.

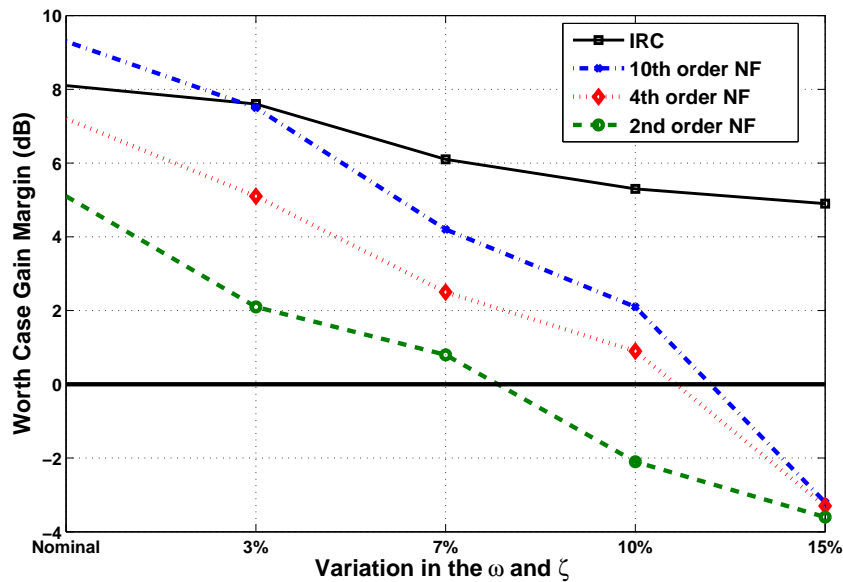


Figure 3.14: Comparison of the nominal and worst case gain margins

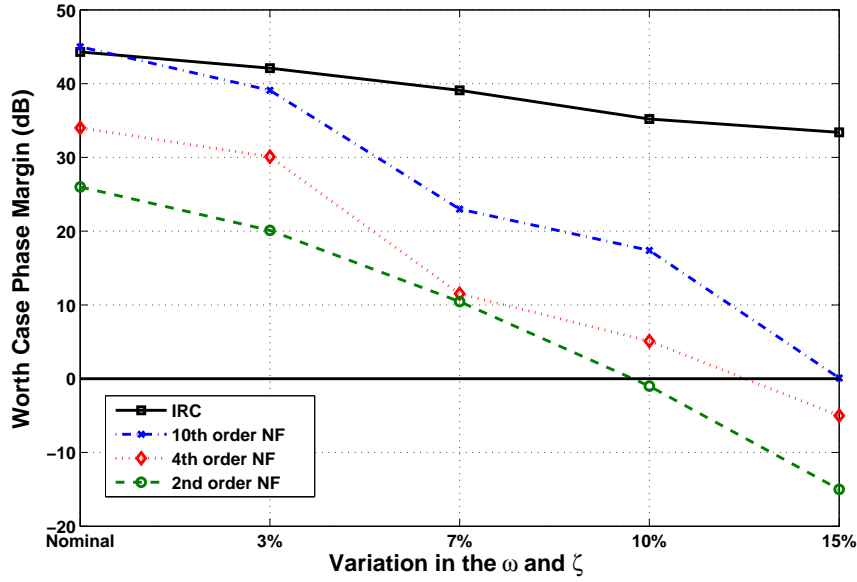


Figure 3.15: Comparison of the nominal and worst case phase margins

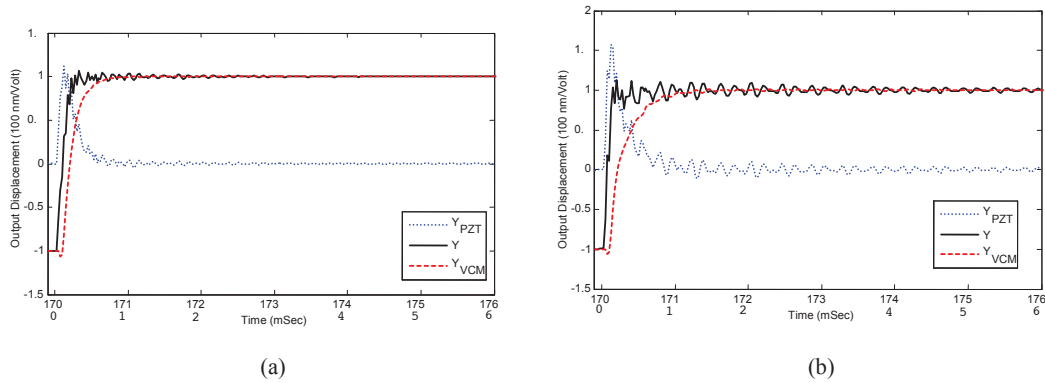


Figure 3.16: (a) Step response for nominal plant (b) Worst-case step response for the variation in PZT parameter

These results for the case that a notch filter controller is designed for the nominal plant tends to be unstable for some instances of the uncertainty set, which clearly proves the necessity of the robust controller for the disk drive servo design. Simulation results show that IRC is more robust than the 10th-order notch filter for parametric variations in resonant modes.

### 3.4.4 Experimental Results

For experimental verification, the designed IRC is implemented for compensating resonant vibration of the piezoelectric microactuator. Implementation is carried out using the same experimental setup described in Chapter 2 except the DSA is replaced with a real-time controller board (dSpace SD1104) with a sampling frequency of 40 kHz. The reference input ( $r$ ) is a 50 Hz square wave with amplitude of 100 mV. The scale of measurement is set at 100 nm/V. The output of the LDV, i.e., the measured displacement of the micro-actuator, is shown in Fig. 3.17. This result proves the effectiveness of IRC in suppressing resonant vibration of the micro- actuator with a sampling frequency of 40 kHz only though the highest resonant frequency is at 18.3 kHz. The experiment is repeated with a 10th-order notch filter compensator and the corresponding output is shown in Fig. 3.18. The output with IRC is superimposed in this figure. It Should be mentioned that the main purpose of the simulation and experimental results presented in the Fig 3.16-3.18 are to to demonstrate the step response of the system. Since the input signal is a periodic square wave each rise and fall can be considered as a step to the system and in general in each cycle of the period, the system have almost the same response (except noise or disturbance). There are two time axis in the plots, the first on is the actually capturing time of the experimental setup and simulation. The other time axis is normalized one to show the step response time.

It should be note again that the time axis have to axis one is the experiment capturing time and the other is

All experimental conditions are kept identical for the two experiments. The performance of the 10th-order notch filter is not as good as we observed in simulation. In simulation, the notch filter is implemented as a continuous time transfer function. But in implementation, a digital notch filter is used. A digital notch filter realized with a sampling frequency of 40 kHz does not attenuate 18.3 kHz resonance very effectively. The choice of 40 kHz sampling frequency is to emulate the scenario when sampling frequency is upper bounded due to physical constraints of the system to be controlled, as in the case of HDD. The same sampling rate is found to be sufficient for implementing the IRC compensator. It underscores the effectiveness of IRC in suppressing resonant vibration in systems having restrictions on sampling frequency.

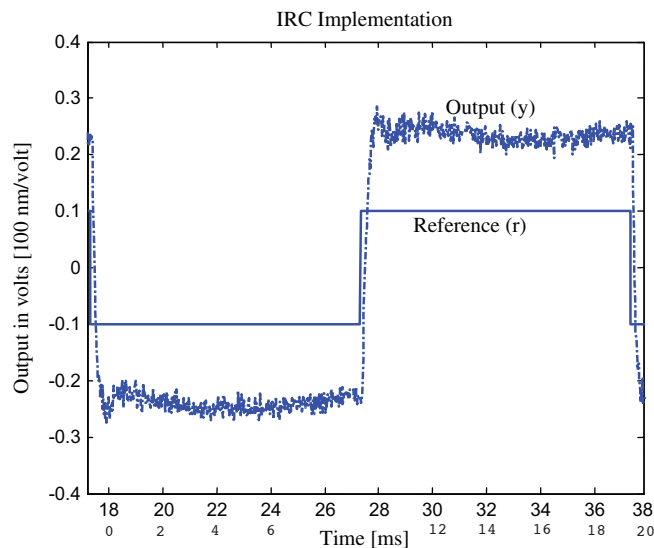


Figure 3.17: Experimental step response with IRC implemented using dSpace card.

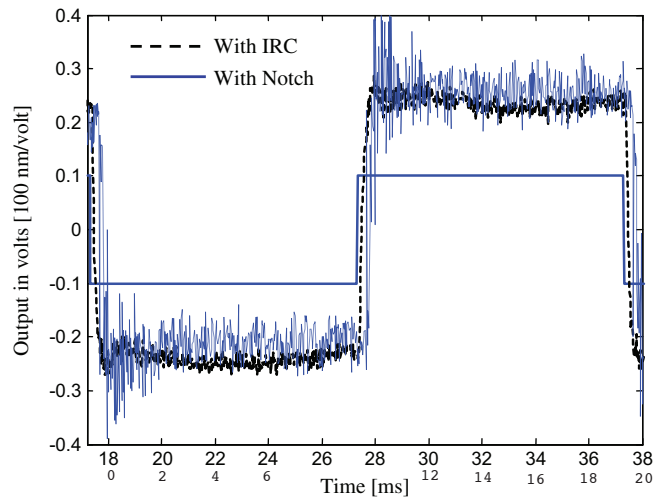


Figure 3.18: Experimental step response comparison between IRC and 10th-order notch filter.

### 3.4.5 Conclusion

This Chapter presents an effective method of suppressing vibration of the flexible modes of a piezoelectric micro-actuator which, nowadays, finds their usefulness in a wide range of applications; including its use as the secondary stage of dual-stage actuation used in many hard disk drive servomechanisms. Its effectiveness is underscored with the help of simulation and experimental results, where it is demonstrated that the performance of a 1st-order IRC compensator in suppressing resonances is comparable to the conventional approach using a much higher order notch filter. The proposed controller is also less sensitive to parametric variation as it does not need the exact knowledge of resonant frequency. Moreover, the IRC compensator can be implemented effectively in systems where the possible choice of the sampling frequency is upper bounded by physical constraints. Finally the IRC method to suppress the resonance of a PZT micro actuator which is used in a dual-stage actuation HDD. The configuration of IRC in a dual-stage model is described and an extended decoupling



sensitivity method is designed for such a structure. The effectiveness of using such a design is evaluated in simulation. The IRC controller is implemented on the dual stage actuator and the results prove that the IRC controller is less complex and more robust than the notch filter method.

# Chapter 4

## Probabilistic Approach for Design of Robust Control

### 4.1 Introduction

Most control designs are based on the use of a design model. However, the relationship between a model and the reality it represents is complex. A mathematical model provides a map from input to output of any real system and can be, at the most, an approximation of the true, physical reality of the system dynamics. Typical sources of discrepancy include unmodelled (usually high-frequency) dynamics, neglected nonlinearities in the modeling, effects of deliberate reduced-order models, and system-parameter variations due to environmental changes and torn-and-worn factors. These modeling errors adversely affect the stability and performance of a control system. As mentioned in chapter 1. to improve the performance of a nanopositioning system we have to consider many different control aspects which are not as critical comparing

to any other system.

In order to attain the nano-level accuracy, the controller design approach should be in a way to achieve the optimum performance for the nominal plant model and guarantee a performance level for the worst case scenario considering all possible uncertainties in the model. Although IRC scheme presented in the previous chapter was found to be more robust than conventional notch filter method for suppressing resonance, it has its own limitations. It cannot deal with multiple resonance mode uncertainty in a MIMO structure. In [65] Bhikkaji et al presented an extension of the IRC technique to resonant MIMO systems based on LMI approach. However, the procedure proposed in the paper for designing IRC controllers involves minimizing a nonlinear nonconvex cost function over a convex set. The nonconvex nature of the cost function makes the control design heavily reliant on the initial guess or the starting point of the nonlinear search used for minimizing the cost function. Moreover, there is no systematical way to guarantee the robust stability for the MIMO case. In this chapter, more generalized methods applicable to both SISO and MIMO systems with uncertainty are considered. There have been many attempts to address uncertainty in robust control community. LQG and Kalman filter can be considered as the earliest efforts. However, the most important breakthrough was the formulation of  $\mathcal{H}_\infty$  problem [66]. In the subsequent fifteen years, several classical optimal methods were developed such as the idea of structured singular value [67], Kharitonov theory of [68] and the optimization technique based on linear matrix inequality (LMI) [69]. Later on methods based on multi-objective optimization were introduced to design state feedback and dynamic output feedback [70, 71]. However, this approach turns

out to be conservative as all Lyapunov matrices are required to be the same for all objectives. The idea of using multiple Lyapunov matrices in robust design was first proposed in [72] and the control design based on this approach was presented in [73]. Most of these mentioned so far are unable to handle parametric uncertainty directly. A computationally tractable locally optimal output feedback controller is presented in [74] which can handle parametric uncertainty. However, computational complexity grows exponentially with the number of uncertain parameters.

To overcome these limitations of robust controller design, a new framework is introduced in robust control which is known as probabilistic approach is introduced in [75]. The main thrust of this approach is that solvability can be achieved through random sampling of constraints provided that a probabilistic relaxation of the worst-case robust paradigm is accepted. Such probabilistic relaxation consists of being content with robustness against the large majority of the situations rather than against all situations. In the probabilistic approach it is shown such large majority is under the control of the designer and can be made arbitrarily close to the set of 'all' situations. There are mainly two synthesis techniques in this framework: average performance synthesis and robust performance synthesis. In the former technique, first proposed in [76], a controller is designed such that, with high probability, the absolute error between average performance (with respect to the uncertainty set) and optimal achievable average performance is within a small desired level. The second approach is analogous to worst case design and employs sequential and non-sequential algorithms. Among the sequential algorithms gradient [77], ellipsoid [78] and cutting plane [79] iterations can be mentioned which can handle convex feasibility problems.

A comprehensive study of probabilistic robust theory [80] and [81].

The problem of designing track following controller for uncertain servo systems can be formulated as an optimization problem subject to a set of bilinear matrix inequalities (BMIs) [48]. However, in general, the optimization subject to a set of BMIs, which is non-convex, is difficult to solve. In the case of a relatively high order uncertain system such as HDD, most of the global approaches to the solution of the BMI problem are not practical due to the resulting large number of variables that enter bilinearly in matrix inequalities [46]. One of the proposed solutions is called local approach. The local approach takes advantage of the property that, by fixing a set of the bilinearly-coupled variables, the BMI problem becomes a convex optimization problem in the remaining variables. The algorithm iterates among two LMI optimization problems. Unfortunately, the convergence properties of this type of dual iteration approach are sensitive to the initial condition and the tolerances of the numerical LMI solvers. Moreover, in general, these algorithms are not guaranteed to converge either to the globally optimal solution or to a locally optimal solution for the originally formulated BMI problem. A computationally tractable locally optimal output feedback controller is presented in [74] which can handle parametric uncertainty. However, computational complexity grows exponentially with the number of uncertain parameters.

The main contribution of this chapter is to solve the robust multi-objective problem arising from the discrete-time track following dynamic output feedback control of a servo system. Sequential algorithm based on ellipsoid iteration is employed in order to efficiently address the problem. The main advantage of the probabilistic ap-

proach over the existing deterministic approaches to robust controller design is that it can handle very general uncertainty structures, where the uncertainty can enter the system in any, possibly non-linear, fashion. In addition to that, with this approach there is no need to solve simultaneously a number of LMIs, whose dimension grows exponentially with the number of uncertain parameters. It rather solves one LMI at each iteration. This turns out to be a very powerful feature when one observes that even for ten real uncertain parameters most of the existing LMI solvers will be unable to handle the resulting number of LMIs. Moreover, by using a similar idea proposed in [73] the design of controller with mixed objectives can be addressed without employing a unique Lyapunov matrix to test all objectives. A dual stage HDD is used as a benchmark to evaluate the performance and robustness of the proposed method.

## Notation

For a square matrix  $X$ ,  $X \succ 0$  ( $X \succeq 0$ ) means  $X$  is symmetric and positive definite (semidefinite).  $I_n$  denotes  $n \times n$  identity matrix. The  $\mathcal{H}_\infty$  norm of a transfer function matrix  $Q(s) \in \mathcal{RH}_\infty$  is denoted as  $\|Q\|_\infty$ . The symbol  $\lceil x \rceil$  is the minimum integer greater or equal to  $x \in \mathbb{R}$ . The symbol  $\star$  in LMIs denotes entries that come from symmetry. The direct sum of matrixes  $X_i$ , ( $i = 1, \dots, n$ ) is denoted as:

$$X_1 \oplus \dots \oplus X_n \triangleq \text{diag}(X_1, \dots, X_n)$$

To indicate that the matrixes  $(A, B, C, D)$  are a state space realization of a trans-

for function matrix  $Q(s)$ , we use the standard notation

$$Q(s) = \left[ \begin{array}{c|c} A & B \\ \hline C & D \end{array} \right] = C(sI - A)^{-1}B + D$$

## 4.2 Problem Formulation of Robust Track-Following Control

In this section, formulation of the problem of robust track following control design for a system with parametric and dynamic uncertainties is presented. The formulation is general enough to cover most of the track-following control problems. However, it has more emphasis on the problem encountered in the magnetic disk drive industry, such as single-stage or dual-stage control design. The HDD servomechanism uses a dual stage actuator with a VCM actuator for coarse movement and a piezoelectric micro-actuator for fine positioning of the read/write head.

Consider the generalized plant with state space representation

$$P : \begin{pmatrix} z_{\Delta} \\ z_o \\ y \end{pmatrix} = \begin{pmatrix} A & B_{\Delta} & B_o & B_u \\ \hline C_{\Delta} & 0 & D_{\Delta o} & D_{\Delta u} \\ C_o & D_{o\Delta} & D_{oo} & D_{ou} \\ C_y & 0 & D_{yo} & 0 \end{pmatrix} \begin{pmatrix} w_{\Delta} \\ w_o \\ u \end{pmatrix} \quad (4.1)$$

where  $u$  is the control input vector that includes input signals for VCM and micro-actuator,  $y$  is the measurement vector which in our problem is positioning error signal

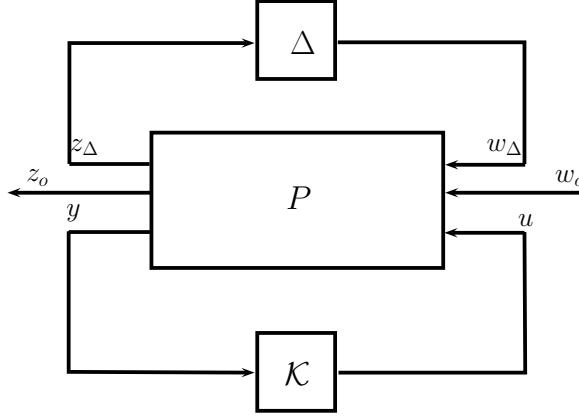


Figure 4.1: Generalized plant with uncertainty  $\Delta$

(PES),  $w_o$  is the vector of exogenous inputs such as airflow vibration and track runout and  $z_o$  is the controlled output vector which consists of PES signal. The symbol  $\Delta$  represents different uncertainties in the plant model and is described as

$$\Delta \doteq \text{diag} [\delta_1, \dots, \delta_n, \mathbf{\Delta}_V, \mathbf{\Delta}_M] \quad (4.2)$$

where  $\delta_i$ ,  $i = 1, \dots, n$  are parametric uncertainties such that  $|\delta_i| \leq 1$  and  $\mathbf{\Delta}_V$  and  $\mathbf{\Delta}_M$  are the set of stable rational transfer functions such that  $\|\Delta_{V,M}\|_\infty \leq 1$ . In the context of HDD, the performance criteria is to minimize RMS of PES signal in time domain while disturbance applied to the system is assumed to be Gaussian white noise. In order to minimize RMS of the PES for the uncertain plant, one should minimize the worst case (over the uncertainty set)  $\mathcal{H}_2$  norm of sensitivity transfer function multiplied by disturbance weighting function:

$$\text{minimize } RMS(PES) \Leftrightarrow \text{minimize}_{k \in \mathcal{K}} \max_{\Delta \in \mathbf{\Delta}} \|G_{z_o w_o}(k, \Delta)\|_2 \quad (4.3)$$



where  $G(s) = \mathcal{F}_l(P(s), k(s))$ ,  $\mathcal{F}_l$  represents lower fractional transformation and  $\mathcal{K}$  is the set of design parameters. The optimization problem in (4.3) is very difficult to solve using classical robust control techniques. In general, there are two approaches for solving this problem in classical robust control. The first approach is mixed  $\mathcal{H}_2/\mathcal{H}_\infty$  design ([71]) which is unable to solve the problem for the case of parametric uncertainty and hence, plant perturbation can significantly degrade performance of the closed loop system. The second approach is robust  $\mathcal{H}_2$  ([74]) that guarantees robust performance for parametric uncertainty but not for dynamic uncertainty. In order to overcome these shortcomings, probabilistic robust technique is used to handle parametric uncertainty while dynamic uncertainty is formulated as linear fractional transformation (LFT) and, using small gain theorem, stability of the closed loop system against dynamic uncertainty is guaranteed. The uncertainty  $\Delta$  is represented as in Fig.4.2 and the optimization problem of (4.3) is converted into the following form:

$$\text{minimize } \gamma \text{ subject to } \begin{cases} \|G_{z_o w_o}(k, \Delta_p)\|_2 < \gamma \\ \|G_{z_V w_V}(k, \Delta_p)\|_\infty < 1 \\ \|G_{z_M w_M}(k, \Delta_p)\|_\infty < 1 \end{cases} \quad (4.4)$$

where  $\Delta_p \in \mathbf{\Delta}_p \doteq \text{diag}[\delta_1, \dots, \delta_n]$  is the set of parametric uncertainties. The first constraint in (4.4) is related to the performance channel which minimizes RMS of the PES signal, the second and the third constraints guarantee the closed loop stability against dynamic uncertainty. The control algorithm to solve the optimization problem (4.4) is given in the next section.

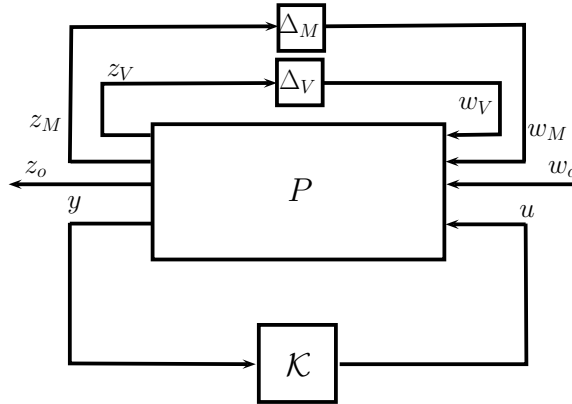


Figure 4.2: LFT form of structured uncertainties

### 4.3 Multi-Objective Robust Control Design based on Linear Matrix Inequality

This section discusses the design of controllers using MIMO design approaches. Compared to SISO design approaches, MIMO design approaches inherently account for the coupling dynamics of the plant and can expectedly achieve better performance. Furthermore, stability robustness can be explicitly considered during the design process by imposing some  $H_\infty$  norm bounds. The information about plant uncertainty type and perturbation range is therefore necessary for constructing a realistic uncertainty model. These methods formulate multiple objectives as a problem of some norm optimization or norm constraints that can be expressed as a set of linear matrix inequalities (LMIs). LMI has gained wide attention in control communities due to its elegant formulation. Moreover, the LMI problems can be solved efficiently using powerful and readily available software packages [82]. Another advantage of using the LMI formulations is that the multi-objective control problem can be treated as

a mixed-objective problem by introducing some constraints in the Lyapunov matrices [73].

### 4.3.1 Mixed $\mathcal{H}_2/\mathcal{H}_\infty$ Controller

In this subsection, formulation and synthesis of mixed  $\mathcal{H}_2/\mathcal{H}_\infty$  are discussed which considers simultaneously the robust stability by  $\mathcal{H}_\infty$  norm bounds and nominal performance by  $\mathcal{H}_2$  norm bound. AS this approach can deal with only dynamic uncertainties, parametric uncertainty is not considered here but is included in the next section. Moreover, the robust stability is guaranteed only for individual, not simultaneous, perturbations. In the mixed  $\mathcal{H}_2/\mathcal{H}_\infty$  approach, the aim is to design a controller  $K$  that exponentially stabilizes the closed-loop system for all dynamic uncertainty sets of  $\Delta_V$  and  $\Delta_M$ , and minimizes the nominal RMS value of  $z_0$  against Gaussian white noise  $w_0$ . In particular, the controller design method used here is based on convex optimization involving LMIs. An LMI based approach is proposed in [71] that guarantees quadratic stability of closed loop system. As a single Lyapunov matrix is used to test all objectives, this approach leads to an overly conservative controller. This problem is addressed by a new approach based on an extra instrumental variable which can be used to build a parameter dependent Lyapunov function [72]. LMI based methodologies of mixed  $\mathcal{H}_2/\mathcal{H}_\infty$  control design for linear systems using the extended characterization introduced in [73]. The goal is to design a dynamic output feedback controller in the form of

$$u = k(s)y = \left[ \begin{array}{c|c} A_k & B_k \\ \hline C_k & D_k \end{array} \right] y \quad (4.5)$$

that makes the closed loop system to satisfy (4.4) but does not take into consideration the parametric uncertainty. The problem is solved by optimization subject to LMI conditions for  $\mathcal{H}_2$  and  $\mathcal{H}_\infty$  norms (see [73]):

$$\underset{\mathcal{W}, \mathcal{P}, \mathcal{K}, \mathcal{G}, \gamma}{\text{minimize}} \gamma, \quad \text{subject to } \mathcal{M}(\mathcal{W}, \mathcal{P}, \mathcal{K}, \mathcal{G}, \gamma, \Delta_i) \succ 0 \quad (4.6)$$

where  $\mathcal{M}(\mathcal{W}, \mathcal{P}, \mathcal{K}, \mathcal{G}, \gamma, \Delta_i)$  is given by

$$\begin{aligned} \mathcal{M}(\mathcal{W}, \mathcal{P}, \mathcal{K}, \mathcal{G}, \gamma, \Delta_i) &= (\gamma^2 - \text{trace}(\mathcal{W})) \oplus \\ &\left[ \begin{array}{cc} \mathcal{W} & C_{cl}^o(\mathcal{K}, 0)\mathcal{G} \\ \star & \mathcal{G} + \mathcal{G}^T + \mathcal{P} \end{array} \right] \oplus \left[ \begin{array}{ccc} \mathcal{P} & A_{cl}^o(\mathcal{K}, 0)\mathcal{G} & B_{cl}^o(\mathcal{K}, 0) \\ \star & \mathcal{G}^T \mathcal{P}^{-1} \mathcal{G} & 0 \\ \star & \star & I \end{array} \right] \oplus \\ &\left[ \begin{array}{cccc} \mathcal{P} & A_{cl}(\mathcal{K}, \Delta_i)\mathcal{G} & B_{cl}^i(\mathcal{K}, \Delta_i) & 0 \\ \star & \mathcal{G}^T \mathcal{P}^{-1} \mathcal{G} & 0 & \mathcal{G}^T C_{cl}^i(\mathcal{K}, \Delta_i) \\ \star & \star & I & 0 \\ \star & \star & \star & I \end{array} \right] \end{aligned} \quad (4.7)$$

and  $\mathcal{P}^T = \mathcal{P}$  and  $\mathcal{W}^T = \mathcal{W}$  are decision variables,  $\mathcal{G}$  is a matrix with the same size as  $\mathcal{P}$ ,  $i = V, M$  and  $A_{cl}^i, B_{cl}^i, C_{cl}^i$  and  $D_{cl}^i$  are the closed loop matrixes for the related channels (PES, VCM and secondary actuator see Fig. 4.2).

The main advantages of the mixed  $\mathcal{H}_2/\mathcal{H}_\infty$  method is low computational cost in finding a solution to (4.7). As a result, the optimal solution is guaranteed on a given feasible condition. However, shortcoming of this method lies in the fact that it can neither deal with parametric uncertainties, nor guarantee robust performance. We address these issue by using a probabilistic approach which is presented in the next section.

$$A_{cl} := \begin{bmatrix} A + B_u D_c C_y & B_u C_c \\ B_c D_y & A_c \end{bmatrix}, \quad B_{cl} := \begin{bmatrix} B_w + B_u D_c D_{yw} \\ B_C D_{yw} \end{bmatrix}, \quad (4.8)$$

$$C_{cl} = \begin{bmatrix} C_z + D_{zu} D_c C_y & D_{zu} C_c \end{bmatrix}, \quad D_{cl} = \begin{bmatrix} D_{zw} + D_{zu} D_c D_{yw} \end{bmatrix} \quad (4.9)$$

## 4.4 Probabilistic Robust Controller

Now we present the probabilistic controller which is the main focus of this chapter. There are a number of approaches in control synthesis using probabilistic technique. The earliest systematic method for probabilistic controller synthesis is based on gradient iteration for solving linear quadratic regulator problem presented in [83]. This approach was later extended to robust LMIs in [77]. A limitation of gradient based method is that it needs a priori knowledge of the radius of the ball which is contained in the feasible set of robust LMI. This radius is used for defining the step size at each iteration. To overcome this problem, iteration method based on ellipsoid algorithm was used in [78] which is a localization based method. This approach benefits from

convexity of the cost function to be minimized and at each iteration, it shrinks the volume of an ellipsoid to find the probabilistic robust feasible solution.

In our approach, the goal is to minimize  $\mathcal{H}_2$  norm of PES subject to stability of the closed loop system in presence of parametric and dynamic uncertainties. The first step in this design is to define a violation function which has the following properties:

- 1)  $\tau(\theta, \Delta) > 0$  if and only if  $\mathcal{M}(\mathcal{W}, \mathcal{P}, \mathcal{K}, \mathcal{G}, \Delta) \not\subseteq 0$  for all  $\Delta \in \mathbf{\Delta}$  (parametric uncertainty is included).
- 2)  $\tau(\theta, \Delta) = 0$  otherwise.

A commonly used violation function for such problems is projection of the matrix inequality (4.7) onto the cone of positive semi-definite matrixes. With this function defined, the original problem (4.4) is reformulated into the following optimization problem:

$$\theta^* = \arg \underset{\theta \in \Theta}{\text{minimize}} \max_{\Delta \in \mathbf{\Delta}} \tau(\theta, \Delta) \quad (4.10)$$

where  $\theta^*$  is any parametrization of the solution set and  $\theta \in \Theta$  includes all decision variables.

The design procedure can be divided into two steps: updating design parameters and estimating the level of satisfaction of the violation function for the updated design parameters. The first step is deterministic while the second one is probabilistic. The given flowchart in Fig. 4.3 illustrates the proposed design procedure. In the first step, the initial ellipsoid  $E^0 = \{\theta \in \Theta : (\theta - k^0)^T F^{-1}(\theta - k^0) \leq 1\}$  with center  $\theta^0$  and

symmetric positive definite matrix  $F \in \mathbb{R}^{N \times N}$  ( $N$  is the dimension of the solution set) is chosen such that it includes the solution set. In the next step, the violation function is evaluated for the given design parameters by sampling the uncertainty set based on the given density function  $f_\Delta$ . The sample bound used is based on log-over-log bound ([84]); if the violation function is zero for *all* samples extracted from the uncertainty set, parameters are given as the probabilistic robust feasible solution. Otherwise, the ellipsoid is updated with smaller one which results from the intersection of the current ellipsoid with the half space  $H^i = \{\theta \in \Theta : \nabla^T \tau(\theta, \Delta)(\theta - \theta^{(i)}) \leq 0\}$  where  $\nabla^T \tau(\theta, \Delta)$  is the sub-gradient of  $\tau(\theta, \Delta)$  defined in [77]. The following theorem guarantees the convergence of the algorithm ([78]). Before giving the theorem, we state an assumption:

**Hypothesis 4.1** *For any design parameter  $\theta$  which is not in the solution set, there is a nonzero probability to generate a sample  $\Delta^{(i)}$  for which  $\tau(\theta, \Delta^{(i)}) > 0$ .*

**Theorem 4.1** *If at  $(i + 1)^{th}$  iteration the ellipsoid is updated as*

$$E^{(i+1)} = \{\theta \in \Theta : (\theta - \theta^{(i+1)})^T F_{i+1}^{-1} (\theta - \theta^{(i+1)}) \leq 1\}$$

where

$$\theta^{(i+1)} = \begin{cases} \theta^{(i)} - \frac{1}{N+1} \frac{F_i \nabla \tau(\theta^{(i)}, \Delta^{(i)})}{\sqrt{\nabla^T \tau(\theta^{(i)}, \Delta^{(i)}) F_i \nabla \tau(\theta^{(i)}, \Delta^{(i)})}} & \text{if } \tau(\theta^{(i)}, \Delta^{(i)}) \neq 0 \\ \theta^{(i)} & \text{if } \tau(\theta^{(i)}, \Delta^{(i)}) = 0 \end{cases}$$

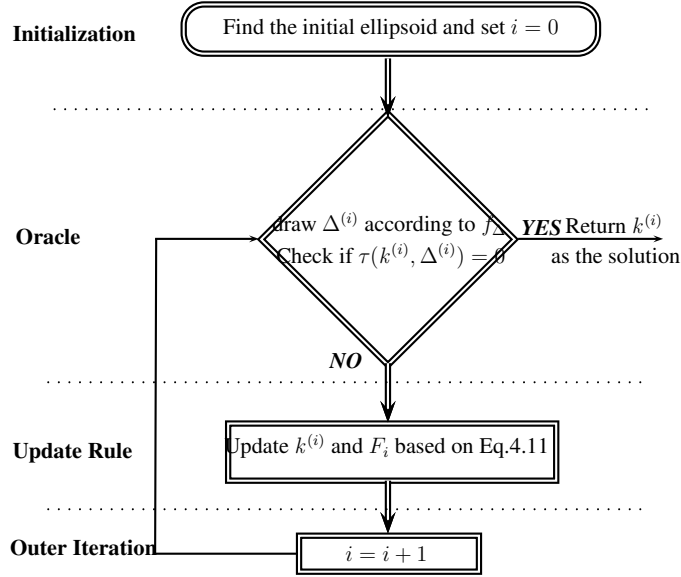


Figure 4.3: Probabilistic design procedure

$$F_{i+1} = \begin{cases} \frac{N^2}{N^2-1} \left( F_i - \frac{2}{N+1} \frac{F_i \nabla \tau(\theta^{(i)}, \Delta^{(i)}) \nabla^T \tau(\theta^{(i)}, \Delta^{(i)}) F_i^T}{\nabla^T \tau(\theta^{(i)}, \Delta^{(i)}) F_i \nabla \tau(\theta^{(i)}, \Delta^{(i)})} \right) & \text{if } \tau(\theta^{(i)}, \Delta^{(i)}) \neq 0 \\ F_i & \text{if } \tau(\theta^{(i)}, \Delta^{(i)}) = 0 \end{cases} \quad (4.11)$$

and Hypothesis.4.1 holds, then with probability one the algorithm given in Fig. 4.3 converges. Furthermore, the maximum number of iterations required to achieve convergence is bounded by  $2N \left\lceil \ln \frac{\text{vol}(E^0)}{\text{vol}(S)} \right\rceil$ ; where  $S$  is the solution set.

Finding the initial ellipsoid that contains the solution set is not a problem. The idea is to find the level set at zero (find  $\theta$  such that  $\tau(\theta, 0) = 0$ ) and bound the level set with a hyper-rectangle, and finally, find an ellipsoid which encircles the hyper-rectangle.



## 4.5 Simulation and Experimental Results

A robust controller is designed for the dual stage actuation servomechanism of an HDD available in the market following the probabilistic design approach mentioned in the previous section. The control objective is to design a controller that *robustly* stabilizes the closed loop plant in the presence of dynamic and parameters uncertainties. In the following subsections, we discuss different steps of this design.

### 4.5.1 Generalized Plant or Augmented Open-loop

The block diagram of the augmented open loop system is shown in Fig.4.7.  $P$  denotes the nominal plant,  $W_u$ ,  $W_\Delta$  and  $W_p$  are the weighting functions and  $\mathcal{K}(z)$  is the dynamic output feedback controller to be designed. The transfer function of VCM and micro-actuator are in the form of:

$$G_{VCM} = \sum_{i=1}^4 \frac{A_i}{s^2 + 2\zeta_i\omega_i s + \omega_i^2}$$

$$G_{MA} = \sum_{i=1}^2 \frac{A_{mi}}{s^2 + 2\zeta_{mi}\omega_{mi} s + \omega_{mi}^2}$$

where parameters  $\omega_i, \zeta_i, A_i, \omega_{mi}, \zeta_{mi}$  and  $A_{mi}$  are plant parameters. Table 2.2 shows the estimated nominal plant parameters. In this chapter the parameters  $\zeta_i$  and  $\omega_i$  are assumed to be uncertain and ranges of their variations are shown in 4.1. The parametric uncertainty is expressed in multiplicative form. It is worth noting that in order to solve this problem in classical robust framework, one has to change the

	$\zeta$	$\omega$
$G_{VCM}$	10%	5%
$G_{MA}$	10%	6%

Table 4.1: Parameter variation in the plant

original uncertain system into a polytopic uncertain system in which transfer function coefficients depend affinity on the uncertain parameters. Hence,  $\zeta_i\omega_i$  and  $\omega_i^2$  should be considered as new uncertain variables. Such a framework is associated with an evident conservatism which results in an over-conservative controller. However, in the probabilistic framework mentioned earlier, each and every parameter with uncertainty is treated individually. In this respect, the probabilistic framework is superior to the classical deterministic one.

Performance of the controller depends on the chosen weighting function. There is no general rule for choosing weighting functions  $W_p$  and  $W_u$ ; however, since the closed loop sensitivity transfer function roughly follows the inverse of the performance weighting function  $W_p$ , we should design  $W_p$  in a way that it has larger magnitude for low frequencies and tends to be smaller in magnitude for higher frequencies. The closed loop bandwidth can roughly be determined by the frequency in which  $W_p$  crosses the  $0dB$  line. The performance weighting function  $W_p$  is chosen to be in the form of

$$W_p = \left( \frac{s/\overline{S} + w_c}{s + w_c\underline{S}} \right)^k$$

for which  $w_c$  is the crossover frequency (desired bandwidth),  $\overline{S}$  determines the desired

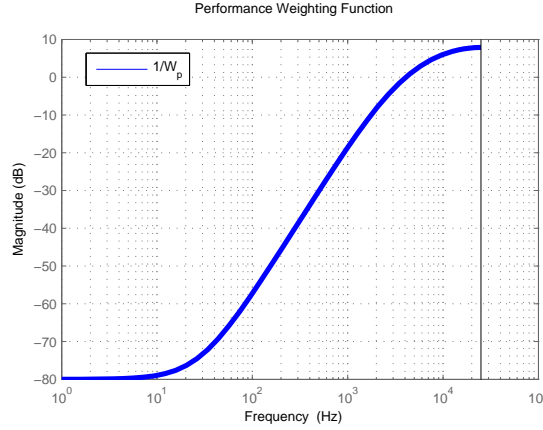


Figure 4.4: The optimal performance weighting function  $W_p$

bound on the sensitivity peak,  $\underline{S}$  determines the minimum level of the closed loop sensitivity function in low frequencies and finally,  $k$  determines the slope of the closed loop sensitivity function. Inverse of the performance weighting function  $W_p$  used in this chapter is shown in Fig.4.4. The function  $W_u$  is used to penalize amplitude of the control signal applied to the plant; it represents a vector with separate penalty function for VCM and micro-actuator. The control weighting functions  $W_{uv}$  and  $W_{um}$  are shown in Fig. 4.5. Finally,  $W_{\Delta V}$  and  $W_{\Delta M}$  defines the dynamic uncertainty weighting functions for the VCM and micro-actuator, respectively. Based on the plant identification presented in Chapter 2.  $W_{\Delta V}$  and  $W_{\Delta M}$  were designed as first-order systems shown in Fig.4.6.

### 4.5.2 Performance Verification

In order to design the controller, the generalized plant should be represented in the state space form. Then the algorithm which is presented in §4.4 is carried out using Matlab [85]. The number of uncertain parameters considered is 10; ranges of their

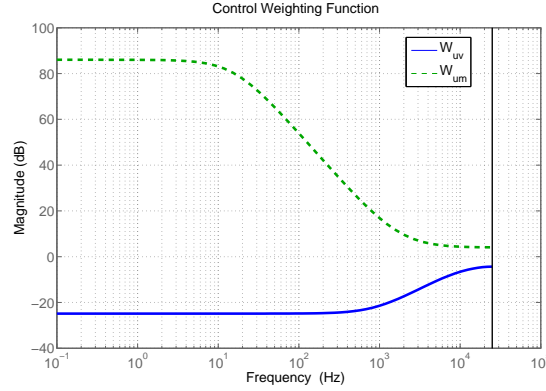


Figure 4.5: Control Weighting Function for VCM  $W_{uv}$  and PZT  $W_{um}$

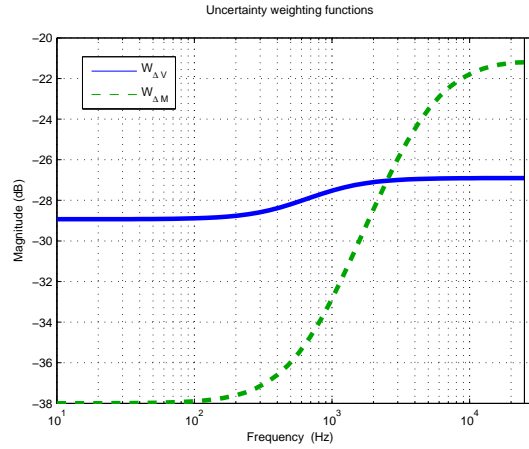


Figure 4.6: Uncertainty weighting functions for VCM  $W_{\Delta V}$  and PZT  $W_{\Delta M}$

variations are given in Table. 4.1. While sampling the uncertainty space, a uniform probability distribution is assumed due to its worst case nature. In order to reduce the number of outer iterations in the algorithm, the  $\mathcal{H}_2/\mathcal{H}_\infty$  problem is solved for the nominal plant using YALMIP [86] and the results are given to the randomized algorithm as the initial value. After a number of iterations which basically depend on initial probabilistic levels,  $\varepsilon$ ,  $\delta$  ( $10^{-5}$  and  $10^{-6}$  respectively) and  $r$ , algorithm comes up with the design parameters that make the closed-loop plant robustly stable (in probabilistic sense).

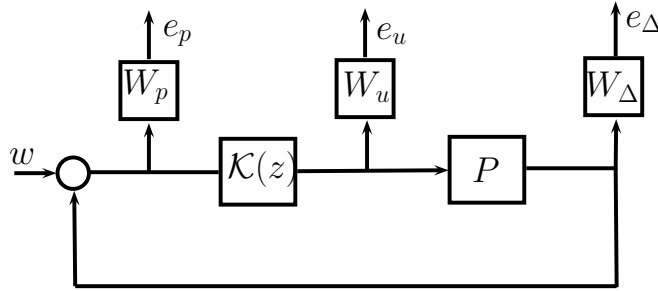


Figure 4.7: Augmented Plant

To further validate our design a posteriori analysis is carried out. With the controller designed, the loop is closed for each one of the 500 plants randomly chosen from the uncertainty set. Fig.4.8 shows closed loop sensitivity plots for the designed controller and Fig.4.9 demonstrates the same plot for the case where the nominal  $\mathcal{H}_2/\mathcal{H}_\infty$  controller is designed without considering any uncertainty. It is clear from these figures that the sensitivity functions of the probabilistic controller do not disperse significantly over the uncertain parameter set. However, the nominal  $\mathcal{H}_2/\mathcal{H}_\infty$  controller tends to vary more and even goes to instability for some realizations of the uncertainty set. It is also clear from the closed loop eigenvalues plotted in Fig.4.10 and Fig. 4.11 that the  $\mathcal{H}_2/\mathcal{H}_\infty$  design leads to instability for a number of realizations from the uncertainty set. Some of the closed loop eigenvalues move to the right half plane for some members of the plant models. On the contrary, the probabilistic approach remains stable for all cases.

Furthermore, stability margins (gain and phase margins) were computed for each of the randomly picked plant transfer functions. Table. 5.2 shows the nominal as well as worst case stability margins for the designed controller. Similar analysis with an  $\mathcal{H}_2/\mathcal{H}_\infty$  controller designed for the nominal plant shows that for some instances of

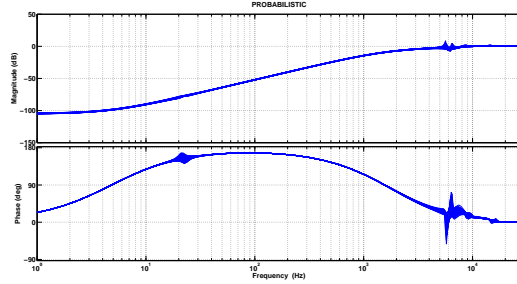


Figure 4.8: Closed loop sensitivity plot with controller designed using probabilistic framework for 500 random samples of  $\Delta \in \Delta$

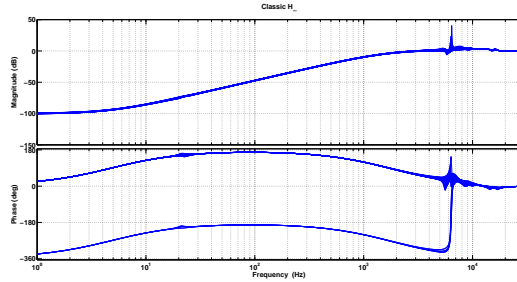


Figure 4.9: Closed loop sensitivity plot with  $\mathcal{H}_2/\mathcal{H}_\infty$  controller designed using YALMIP for 500 random samples of  $\Delta \in \Delta$

uncertainty set, the closed loop becomes unstable. It clearly proves the necessity for considering the uncertainties in full while designing a robust controller for the disk drive servo.

Performance of the designed controller in rejecting disturbances is evaluated using time-domain results. The disturbance model which has been presents in chapter 2 is used for this simulation. The achieved track misregistration (TMR), RMS and peak values of the control input signals for the nominal as well as worst case scenarios are given in Table. 5.4.2. It can be seen clearly that they do not change significantly for different members of the family of uncertain plants. Therefore, the designed controller satisfies the performance requirements in a robust manner.

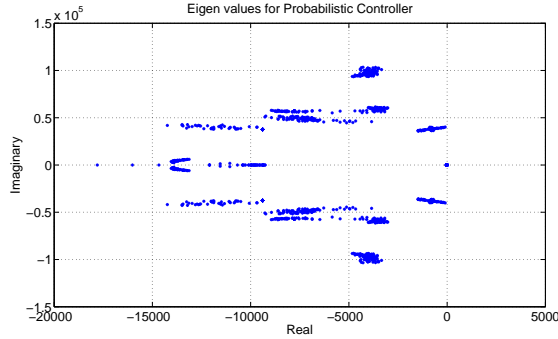


Figure 4.10: Closed loop eigenvalues plot with controller designed using probabilistic framework for 500 random samples of  $\Delta \in \Delta$

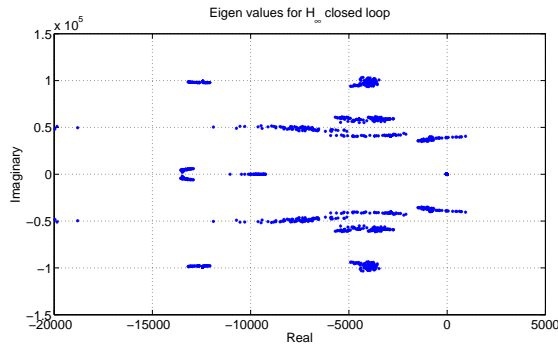


Figure 4.11: Closed loop eigenvalues plot with  $\mathcal{H}_2/\mathcal{H}_\infty$  controller designed using YALMIP for 100 random samples of  $\Delta \in \Delta$

### 4.5.3 Control Implementation

Simulation results in the previous section confirms that the designed controller achieves robust stability and performance in the presence of parametric variation in a dynamical system. The effectiveness of the design is further verified through experiment. The control algorithm is implemented in real time using the DSP based system with sampling frequency of  $50kHz$ . Since the problem is of regulation type, the output sensitivity transfer function, which shows the ability of the system in rejecting different output disturbances, is of vital importance.

The transfer function from reference input to the error which represents the output

<i>Design Approach</i>	<i>Gain Margin (dB)</i>		<i>Phase Margin (Degree)</i>	
	<i>Nominal</i>	<i>Worst Case</i>	<i>Nominal</i>	<i>Worst Case</i>
<i>Designed Probabilistic Controller</i>	8.6	3.37	46.02	37.95
<i>Nominal <math>\mathcal{H}_2/\mathcal{H}_\infty</math> Design</i>	7.95	-1.16	50.81	-39.16

Table 4.2: Comparison of the nominal and worst case stability margins

<i>TMR (nm)</i>		<i>RMS(<math>u_V</math>) (mV)</i>		<i><math>\ u_V\ _\infty</math> (mV)</i>	
<i>Nominal</i>	<i>Worst Case</i>	<i>Nominal</i>	<i>Worst Case</i>	<i>Nominal</i>	<i>Worst Case</i>
9.48	9.87	12.8	12.9	67.9	69.2

Table 4.3: Comparison of the nominal and worst case performance specifications

sensitivity function is experimentally measured using DSA for both nominal controller and the designed probabilistic controller. The result of this experiment along with simulation results are shown in Fig.4.12 and Fig. 4.13.

The step response is another important performance measure. The designed controller was evaluated with a 50 *Hz* square wave signal. Fig.4.14 and 4.15 show the output displacement for a step responses of 100 *nm* as well as the corresponding input signal to the VCM driver the PZT actuator. Each rise and fall in the reference signal is considered as a step trigger. The fluctuating signals on the step response is mostly due to disk rotation and the air-flow induced vibration. The simulation and experimental results match fairly and the small difference is due to small delay in the DSP system, LDV noise and repeatable disturbances due to disk rotation (the main component and its harmonics).



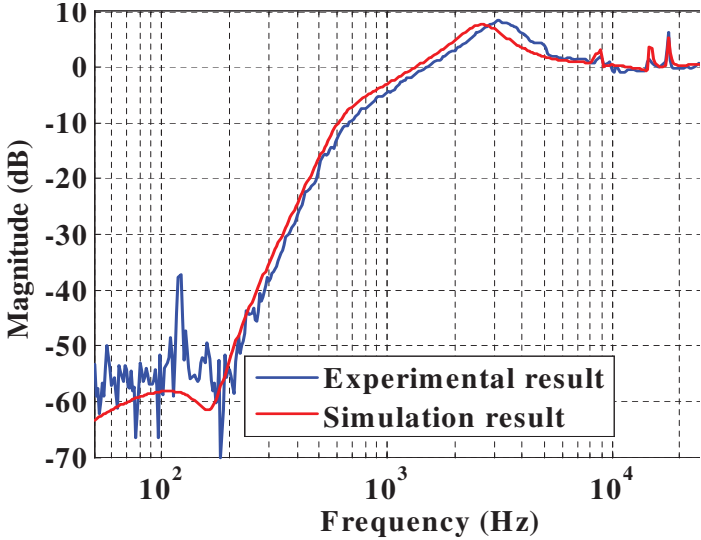


Figure 4.12: Sensitivity plot of the nominal controller.

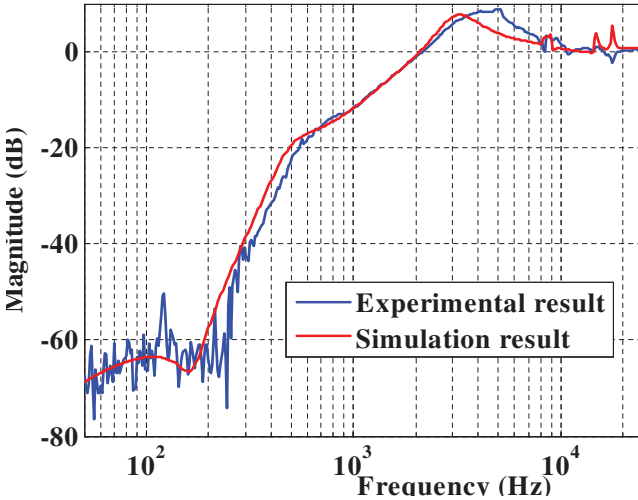


Figure 4.13: Sensitivity plot of the probabilistic controller.

## 4.6 Conclusion

Uncertainty in the dynamics of the plant is inevitable for any physical system. On the other hand, higher performance has always been in demand due to the rapid growth of technology of nanopositioning. In the classical robust controller design, performance

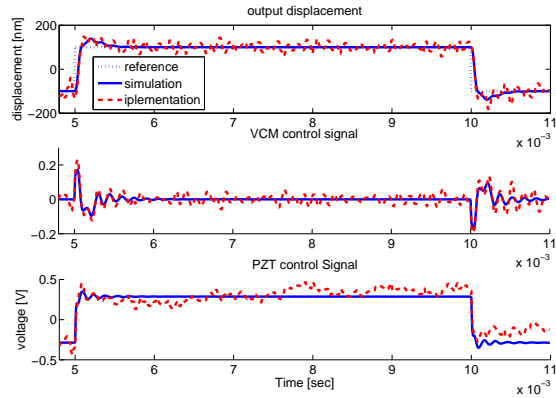


Figure 4.14: Implementation of head position and control signals for  $\mathcal{H}_2/\mathcal{H}_\infty$  method

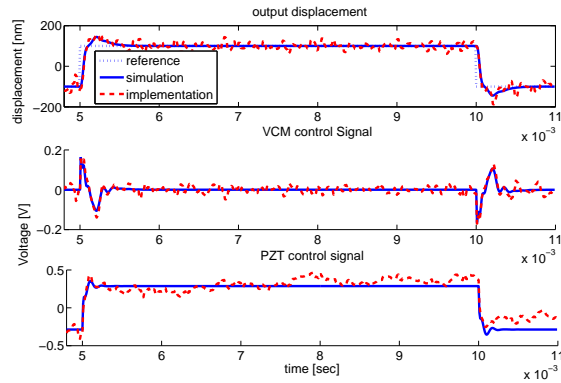


Figure 4.15: Implementation of head position and control signals for probabilistic method

is sacrificed considerably in order to achieve robustness specially in cases where parametric uncertainty is included non-linearly into plant description. However, for the approach presented in this chapter and which benefits from probabilistic concepts and randomization, no conservatism has been introduced. Furthermore, one shortcoming of classical robust design comes from considerable computational complexity in handling parametric uncertainty. To the best of our knowledge, the best classical robust controller which can handle parametric uncertainties is the design procedure based on local BMI optimization [74]; However, the computational complexity of this approach increases exponentially with the number of uncertain parameters. The

approach based on probabilistic robust design and randomized algorithms has broken the curse of dimensionality thanks to randomization. As a result, the algorithm presented in this chapter is computationally tractable and computational complexity does not depend on the dimension of the uncertainty set (the number of uncertain parameters).

This chapter presents the results of designing a discrete time multi-objective robust controller using the probabilistic robust approach to handle different parametric and dynamic uncertainties in the hard disk drive servomechanism. An iterative algorithm based on ellipsoid iteration is used to find the probabilistic robust feasible solution. The design is less conservative compared to classical robust approaches in a way that the original non-linear parametric uncertainty is treated as it is and is not embedded into affine structure. Furthermore, multiple Lyapunov matrixes are used for different objectives. In disk drive, performance is of great importance; the control algorithm, while handling different uncertainties, should not be conservative. In this design, by allowing a small probability that the objective function being violated, the performance of the resulting controller is close to the nominal controller. Effectiveness of the design algorithm is also verified through experiment.

# Chapter 5

## Design Controller under Irregular Sampling

### 5.1 Introduction

Sampled-data systems with a known constant sampling interval have been studied extensively over the past decades and the systems can be analyzed in the discrete time. When the sampling interval is be inconsistent or variable, the situation is more complicated. Time-varying sampling is applied to many practical systems. For instance networked control systems which have emerged as a hot research area provide a convincing background, where conflicts may exist and inevitably degrade control performance due to external traffic and the limitation of the network resource. Under such conditions, it may improve the system performance that the sampling period varies with the network condition. Recently, there are also considerable research efforts on time-varying sampling periods [87], [88]. Suplin et al. [89] and Gao et al. [90]

studied sampled data  $H_\infty$  control with non-uniform sampling.

Conventionally the servo system of HDD is modeled as an LTI system and, therefore, LTI control design tools are used for the design of the servo controller [15]. However, time invariance of the HDD servo system is not a valid assumption as the sampling rate in HDD may vary due to various reasons. Irregular sampling will be a more frequent problem when disks are prewritten with servo patterns as in case of discrete-track HDD or bit patterned media HDD [37] [38]. In these cases, the center of the rotation of the disk does not coincide with the center of the servo tracks as illustrated in Fig.5.1. With such misalignment between the center of the disk and the center of rotation, there can be considerable variations in the sampling rate of the position error signal (PES) [38]. Irregular sampling may also be the result of other problems, e.g., media defects in servo sectors, the fast disk motion causing incorrect detection of servo address mark (SAM) etc. contributing to false PES demodulation. The feedback PES is unavailable in those servo sectors, resulting in an irregular sampling [39].

In general, there are two possible ways to update the control action for a system with irregular sampling. In the first scheme after a measurement is obtained, the control action is updated as quickly as possible making the control update rate to be irregular as well. In the other scheme, the control action is updated at a fixed, regular rate. In the case of the HDD second scheme is more appropriate since the output of the controller is usually passed through one or more notch filters, and the notch

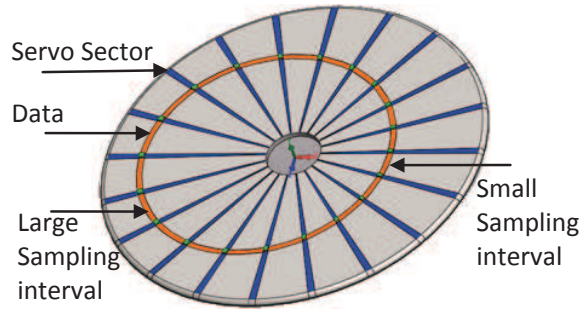


Figure 5.1: The center of the servo tracks does not exactly coincide with the center of rotation of the disk

filters can be designed independent of the sampling rate variation if this scheme is used.

In the recent past, designing robust track following controller using optimization technique based on semi-definite programming (SDP), known in engineering as LMI (Linear Matrix Inequality), has received considerable attention from researchers and industries [91]. These methods show promising results to improve performance by reducing overall track misregistration (TMR). However, if the number of parametric uncertainties increases these methods become computationally complex and conservative [36]. In the case of a linear system with irregular sampling rate, most of the parameters in the state space realization of the system become uncertain and it may not be possible to find an analytical solution with the currently available LMI solvers. Moreover, even if we limit the size of uncertainty set the solution become too conservative and not tally to initial problem.

These limitations of robust control design can be overcome by, a newly introduced framework known as probabilistic approach which is discussed in the previous

chapter. There are two controller synthesis techniques in this framework: average performance synthesis and robust performance synthesis. The former was first proposed by Vidyasagar in [76]. In this approach, the controller is designed in a way that, with high predefined probability, the absolute error between average performance (with respect to the uncertainty set) and optimally achievable average performance is kept within a desired (small) level. The second approach is analogous to worst case design and it employs sequential and nonsequential algorithms. Among the sequential algorithms gradient [77], ellipsoid [78] and cutting plane [79] iterations can be mentioned which can handle convex feasibility problems. The scenario approach of Calafiore and Campi [92, 93] is a non-sequential technique which can solve in a probabilistic sense any general uncertain convex optimization problems.

This chapter presents a robust probabilistic control design methodology in case of irregular sampling. This approach is based on a scenario probabilistic design which is a non-sequential randomized technique for achieving probabilistic robustness in design. This method is used to address the problem of the design of HDD track following controller in presence of irregular sampling. Simulation results show that the designed controller can achieve required performance while maintaining good robustness.

The chapter is organized as follows. The discretization methods for three different schemes of sampling and actuation are discussed in Section 2. It is also explained in this section how to form LPTV discrete-time models of systems with these sampling and actuation characteristics of a continuous-time model. Section 3 presents the details of the probabilistic controller design with the scenario approach for the discrete-time systems resulting from irregular sampling. Section 4 examines the per-

formance of a HDD in track-following mode for each of the three sampling and actuation schemes. Finally, conclusions are given in Section 5.

## 5.2 Model of Servo System under Irregular Sampling

In this section, we describe each of the three difference schemes of sampling and explain the discretization methods to obtain the LPTV discrete-time models of systems with these sampling and actuation characteristics from a continuous-time model. Throughout this section, the continuous-time state space model of the system is given by

$$\dot{x}_c(t) = A_c x_c(t) + B_c u_c(t) \quad (5.1)$$

$$y_c(t) = C_c x_c(t) + D_c u_c(t) . \quad (5.2)$$

The signals  $x_c(t)$ ,  $u_c(t)$ , and  $y_c(t)$  respectively have dimension  $n_x$ ,  $n_u$ , and  $n_y$ . The computational delay associated with the controller will be denoted as  $\delta$ . We also define for  $T > 0$

$$A_d(T) := e^{A_c T}, \quad B_d(T) := \left( \int_0^T e^{A_c \tau} d\tau \right) B_c .$$



Note in particular that these matrices are the discrete-time state space matrices that result when discretizing the continuous-time state dynamics using a zero-order hold with period  $T$ . Throughout this section, we will use a zero-order hold approach to discretizing the model.

### 5.2.1 Regular Sampling and Actuation

The first case considers a system where measurements are generated at a regular rate and the control signal is updated at the same rate. Due to computational delay( $\delta$ ), the control signal is not updated at the same time as measurements are obtained. We will assume for simplicity that  $\delta < T$ , where  $T$  is the sample period.

The simplest approach to discretizing this system is used the `c2d` command in MATLAB. To incorporate the computational delay, either the `InputDelay` or `OutputDelay` property of the continuous-time model should be set to  $\delta$  before using the `c2d` command. Since  $\delta < T$ , this method introduces either  $n_u$  or  $n_y$  extra states to the model as part of the discretization process, depending on whether the `InputDelay` or `OutputDelay` property was used.

We now describe an alternate discretization method that does not introduce any extra states. We first choose  $t = 0$  so that the control is updated at time instances

$$t_{u,k} = kT, \quad k \in \mathbb{Z}$$

which means that the measurements are obtained at time instances

$$t_{y,k} = (k + 1)T - \delta, \quad k \in \mathbb{Z} .$$

Note that we have shifted the time index associated with the measurements by one step.

We now define

$$x_k := x_c(t_{u,k}) \tag{5.3}$$

$$u_k := u_c(t_{u,k}) \tag{5.4}$$

$$y_k := y_c(t_{y,k}) . \tag{5.5}$$

The zero-order hold assumption yields that

$$u(t) = u_k, \quad t \in [t_{u,k}, t_{u,k+1})$$

which means that (5.1) is discretized as

$$x_{k+1} = A_d(T)x_k + B_d(T)u_k . \tag{5.6}$$

To find the discrete-time representation of the measurements, we first note that

$$t_{y,k} = t_{u,k} + (T - \delta)$$

which means that

$$y_k = C_c x_c(t_{u,k} + (T - \delta)) + D_c u_c(t_{u,k} + (T - \delta)) .$$

By the zero-order hold assumption

$$u_c(t_{u,k} + (T - \delta)) = u_k$$

$$x_c(t_{u,k} + (T - \delta)) = A_d(T - \delta)x_k + B_d(T - \delta)u_k$$

which implies that

$$y_k = [C_c A_d(T - \delta)]x_k + [C_c B_d(T - \delta) + D_c]u_k . \quad (5.7)$$

Note that (5.6) and (5.7) constitute an LTI discrete-time model. This model describes the continuous-time model (5.1)–(5.2) under a zero-order hold on the input without introducing any additional states during the discretization process.

However, there is one subtle detail that remains: with the convention we have chosen for defining  $y_k$ , we cannot use any arbitrary control scheme to control this model. In particular, for continuous-time causality to hold,  $u_k$  can only depend on  $y_{k-1}, y_{k-2}, y_{k-3}, \dots$ , i.e. a discrete-time controller satisfies continuous-time causality if and only if it is *strictly* causal in the discrete-time domain.

### 5.2.2 Irregular Sampling and Actuation

We now consider the case when the measurements are sampled at an irregular (but periodic) rate and the control action is updated as quickly as possible after a measurement is obtained. In particular, we consider the case when the measurements are obtained at time instances  $t_{y,k}$ ,  $k \in \mathbb{Z}$  where the sequence

$$T_k := t_{y,k} - t_{y,k-1}$$

is periodic with period  $N$ . For simplicity, we assume that  $T_k > \delta$ ,  $\forall k \in \mathbb{Z}$ . The time instances when the control is updated will be denoted by  $t_{u,k}$ ,  $k \in \mathbb{Z}$ . Due to computational delay, we have the relationship

$$t_{y,k-1} = t_{u,k} - \delta .$$

Notice that, as in Section 5.2.1, we have shifted the time index associated with the measurements by one step. Also note that we have the relationship

$$t_{u,k+1} - t_{u,k} = T_k .$$

We now define  $x_k$ ,  $u_k$ , and  $y_k$  as in (5.3)–(5.5) and notice that, by the zero-order hold assumption

$$x_{k+1} = A_d(T_k)x_k + B_d(T_k)u_k . \tag{5.8}$$

Since  $T_k$  varies with time, these dynamics are time-varying. However, because  $T_k$  is periodic with period  $N$ , we see that  $A_d(T_k)$  and  $B_d(T_k)$  are periodic with period  $N$ , i.e. these dynamics are LPTV.

To find the discrete-time representation of the measurements, we first note that

$$t_{y,k} = t_{u,k} + (T_k - \delta)$$

which means that

$$y_k = C_c x_c(t_{u,k} + (T_k - \delta)) + D_c u_c(t_{u,k} + (T_k - \delta)) .$$

Using the zero-order hold assumption along with the method in Section 5.2.1, we obtain

$$y_k = [C_c A_d(T_k - \delta)]x_k + [C_c B_d(T_k - \delta) + D_c]u_k . \quad (5.9)$$

Note that (5.8) and (5.9) constitute a discrete-time state space model. Also note that all of the model parameters are periodic with period  $N$ , which implies that this state space model is LPTV. This model describes the continuous-time model (5.1)–(5.2) under a zero-order hold on the input with sampling and actuation conditions described at the beginning of this section. As in Section 5.2.1, a discrete-time controller satisfies continuous-time causality if and only if it is *strictly* causal in the discrete-time domain.

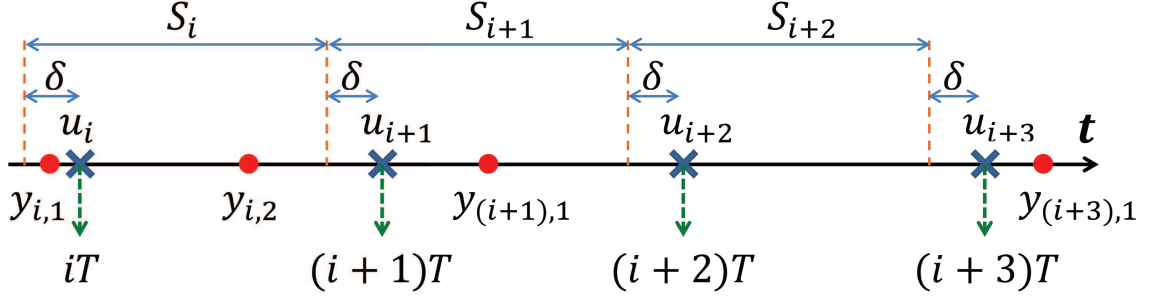


Figure 5.2: Schematic timeline for irregular sampling (circles) and regular control (crosses) updates

### 5.2.3 Irregular Sampling with Regular Control Updates

We now consider the case when the measurements are sampled at an irregular (but periodic) rate. However, unlike Section 5.2.2, the control action is updated at a regular rate. Figure 5.2 shows a schematic timeline that represents the instances measurements (shown by circles) arrive and control signal (shown by crosses) is updated. We choose  $t_0 = 0$  so that the control is updated at time instances

$$t_{u,k} = kT + t_0, \quad k \in \mathbb{Z}.$$

In this system architecture, the role of computational delay is fundamentally different than in the previous sections. In particular, since the control updates are scheduled in time rather than the control being updated as quickly as possible after receiving a measurement, we treat the computational delay as the constraint that  $u_k$  can only depend on any measurements that arrive in the time interval  $(-\infty, t_{u,k} - \delta]$ . Equivalently, the value of  $u_k$  will be updated at time step  $k + 1$  by measurements that

arrive in the time interval

$$S_k := (t_{u,k} - \delta, t_{u,k+1} - \delta] .$$

We now define  $x_k$  and  $u_k$  as given in (5.3)–(5.4). Since the control is updated regularly in time, we discretize (5.1) as

$$x_{k+1} = A_d(T)x_k + B_d(T)u_k .$$

These dynamics are LTI and do not depend on the measurement characteristics of the system.

We now find the representation of a measurement at a time instant  $\bar{t} \in S_k$ . There are two cases to consider. The first case corresponds to  $\bar{t} \geq t_{u,k}$ . In this case, we obtain

$$\begin{aligned} y(\bar{t}) &= C_c x_c(\bar{t}) + D_c u_c(\bar{t}) \\ &= [C_c A_d(\bar{t} - t_{u,k})]x_k + [C_c B_d(\bar{t} - t_{u,k}) + D_c]u_k \end{aligned}$$

The second case corresponds to  $\bar{t} < t_{u,k}$ . In this case, we note that

$$\begin{aligned} x_c(\bar{t}) &= A_d(\bar{t} - t_{u,k-1})x_{k-1} + B_d(\bar{t} - t_{u,k-1})u_{k-1} \\ &= A_d(\bar{t} - t_{u,k-1})A_d^{-1}(T)[x_k - B_d(T)u_{k-1}] \\ &\quad + B_d(\bar{t} - t_{u,k-1})u_{k-1} . \end{aligned}$$

For notational convenience, we define

$$\bar{A} := A_d(\bar{t} - t_{u,k-1})A_d^{-1}(T)$$

$$\bar{B} := B_d(\bar{t} - t_{u,k-1}) - A_d(\bar{t} - t_{u,k-1})A_d^{-1}(T)B_d(T)$$

so that the previous expression can be written as

$$x_c(\bar{t}) = \bar{A}x_k + \bar{B}u_{k-1} .$$

This yields

$$\begin{aligned} y(\bar{t}) &= C_c x_c(\bar{t}) + D_c u_c(\bar{t}) \\ &= C_c \bar{A}x_k + C_c \bar{B}u_{k-1} + D_c u_k . \end{aligned}$$

Since this expression depends on  $u_{k-1}$ , we need to augment the state vector, i.e. we write the state dynamics of the discrete-time system as

$$\begin{bmatrix} x_{k+1} \\ u_k \end{bmatrix} = \begin{bmatrix} A_d(T) & 0 \\ 0 & 0 \end{bmatrix} \begin{bmatrix} x_k \\ u_{k-1} \end{bmatrix} + \begin{bmatrix} B_d(T) \\ I \end{bmatrix} u_k . \quad (5.10)$$

Again, these dynamics are LTI and do not depend on the measurement characteristics



of the system. The output at a time instant  $\bar{t} \in S_k$  corresponds to

$$y(\bar{t}) = \bar{C} \begin{bmatrix} x_k \\ u_{k-1} \end{bmatrix} + \bar{D}u_k \quad (5.11)$$

where

$$\bar{C} = \begin{cases} \begin{bmatrix} C_c \bar{A} & C_c \bar{B} \end{bmatrix}, & \bar{t} \in (t_{u,k} - \delta, t_{u,k}) \\ \begin{bmatrix} C_c A_d(\bar{t} - t_{u,k}) & 0 \end{bmatrix}, & \bar{t} \in [t_{u,k}, t_{u,k+1} - \delta] \end{cases} \quad (5.12)$$

$$\bar{D} = \begin{cases} D_c, & \bar{t} \in (t_{u,k} - \delta, t_{u,k}) \\ C_c B_d(\bar{t} - t_{u,k}) + D_c, & \bar{t} \in [t_{u,k}, t_{u,k+1} - \delta] \end{cases} \quad (5.13)$$

Although (5.11)–(5.13) describe the output at an arbitrary time instance, these relationships do not fully describe the system output corresponding to a given time index. In particular, since there is no fixed relationship between the times at which measurements are obtained and the times at which the control is updated, the number of samples in the time interval  $S_k$  is not necessarily constant over  $k$ . For simplicity, we will consider a situation in which 0, 1, or 2 measurements may be made in any time interval  $S_k$ . We thus have three cases to consider. In all three cases, we will force the discrete-time model to have two outputs.

We begin by considering the case when, for a particular value of  $k$ , there are two measurements made in the time interval  $S_k$ ; we denote the time instances correspond-

ing to these measurements as  $\bar{t}_1$  and  $\bar{t}_2$ . In this case, we choose

$$y_k = \begin{bmatrix} y(\bar{t}_1) \\ y(\bar{t}_2) \end{bmatrix}. \quad (5.14)$$

Note that  $y_k$  captures all of the information that the controller can use to update the value of  $u_k$  to  $u_{k+1}$ .

We now consider the case when, for a particular value of  $k$ , there are no measurements made in the time interval  $S_k$ . In this case, the controller should accept no inputs at time step  $k$ . Equivalently, the input into the controller should be zero. This motivates choosing

$$y_k = \begin{bmatrix} 0 \\ 0 \end{bmatrix}. \quad (5.15)$$

Choosing this form for  $y_k$  allows the system to have a time-invariant structure;  $y_k$  is acting here as a placeholder so that the discrete-time model has two outputs, even at time steps when the controller has no inputs.

Finally, we consider the case when, for a particular value of  $k$ , there is one measurement made in the time interval  $S_k$ ; we denote the time instance corresponding to this measurement as  $\bar{t}$ . In this case, we choose

$$y_k = \begin{bmatrix} y(\bar{t}) \\ 0 \end{bmatrix}. \quad (5.16)$$

As in the previous case, we are using zeros as placeholders so that the discrete-time model has two outputs, even at time steps when the controller only has one input.

Under the assumption that the sampling of the system is periodic, (5.10)–(5.16) define an LPTV discrete-time state space model. This model describes the continuous-time model (5.1)–(5.2) under a zero-order hold on the input with sampling and actuation conditions described at the beginning of this section. As in Section 5.2.1, a discrete-time controller satisfies continuous-time causality if and only if it is *strictly* causal in the discrete-time domain.

Under the assumption that the sampling of the system is periodic, (5.10)–(5.13) define an LPTV discrete-time state space model without loss of generality we can assume that the period of the system is large enough to model it as linear time varying system . This model describes the continuous-time model (5.1)–(5.2) under a zero-order hold on the input with sampling and actuation conditions described at the beginning of this section. As in the general case , a discrete-time controller satisfies continuous-time causality if and only if it is *strictly* causal in the discrete-time domain.

## 5.3 Controller Design under Irregular Sampling

### 5.3.1 Limits of Performance in HDD

This section presents optimal LQG control design with variance constraints for the discrete-time systems discussed in Section 5.2. As discussed in the introduction, the goal of the optimal LQG control design in this section is not to design a controller to

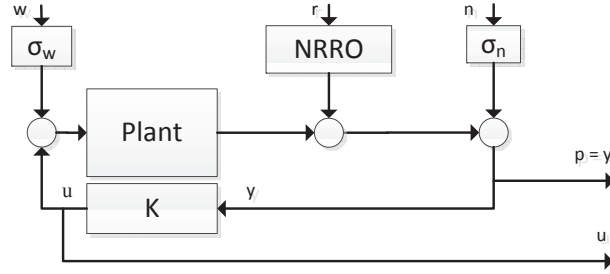


Figure 5.3: Control architecture for either regular sampling and actuation or irregular sampling and actuation

be implemented on an HDD, but rather to assess the limitations of performance of various hardware setups.

When the plant is modeled as an LPTV state space model whose entries are periodic with period  $N$ , the proposed controller will be also be LPTV. Although the output signals are not stationary when the plant and controller are both LPTV, their second-order statistics will be periodic, with period  $N$ . Thus, a good way to capture the performance of a controller is to compute the RMS and maximum  $3\sigma$  values of the relevant signals over a revolution of the HDD. Hence, the control objective throughout this chapter is to minimize the RMS of  $3\sigma$  value of PES while keeping the variance of control less than or equal to a value specified by the control designer. The architecture we use for control design when sampling and control update rate are either both regular or both irregular in time is shown in Fig. 5.3.

The signals  $r, w$  and  $n$  are independent white noises with unit variance that respectively model the effect of the non-repeatable runout (NRRO), windage, and measurement noise. The signals  $p, y$  and  $u$  are respectively the performance, measurement

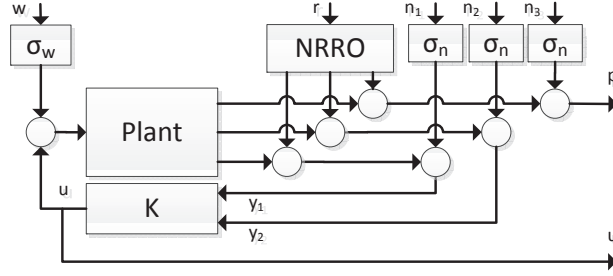


Figure 5.4: Control architecture for regular actuation, but irregular sampling and control signals, respectively. Note that the performance and measurement signals are both equivalent to the PES. The blocks  $K$ , NRRO,  $\sigma_n$  and  $\sigma_w$  are respectively the controller, the NRRO model, the standard deviation of measurement noise, and the standard deviation of the windage.

The control structure considered for a system with irregular sampling time and regular control update is shown in Fig. 5.4. As in Section 5.2.3, we assume that the number of measurements arriving between two consecutive control updates is less than or equal to two;  $y_i$  and  $\sigma_i$  are respectively the  $i$ -th component of  $y_k$  discussed in Section 5.2.3 and its corresponding measurement noise, for  $i \in \{1, 2\}$ . The signals  $w$ ,  $r$  and  $u$  have the same definition as the signals in Fig. 5.3. The signals  $p$  and  $n_3$  are respectively the performance signal and the noise contaminating  $p$ . Here,  $p$  represents the position error of the head at the time instances when the control signal is updated. Since these time instances do not coincide with the time instances at which the PES is measured, it is not, strictly speaking, the PES. However, it is a better measure of performance than the PES because it is sampled regularly in time. In particular, if we were to use the PES itself as the measure of performance, taking the mean of the PES variance would, from a spatial perspective, weight the mean towards the parts

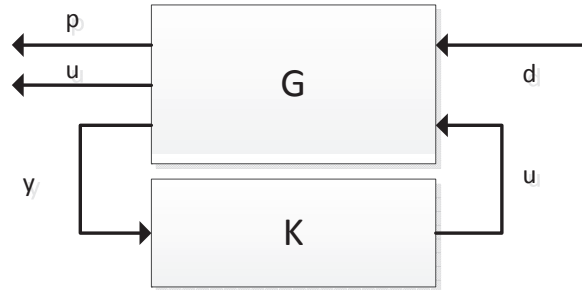


Figure 5.5: System structure for control design

of the disk for which measurements are more closely spaced. For example, if  $3/4$  of the PES measurements occur over half of a disk revolution, the mean PES variance would be strongly weighted toward the measurements in that half of the disk in which the measurements are closely spaced. Since making measurements more frequently tends to yield better optimal performance, the mean PES would be weighted towards the half of the disk in which the performance is best. As an added benefit of choosing our performance signal as  $p$  rather than the PES, the state space entries of the plant that correspond to the signal  $p$  are time-invariant.

Regardless of the sampling and actuation conditions, we can model the closed-loop system, which we denote as  $G_{cl}(K)$ , as the block diagram shown in Fig. 5.5. In this block diagram,  $K$  and  $G$  are respectively the controller and the open-loop model containing both the discretized plant and the discretized disturbance models. The signals  $d, p, y$  and  $u$  in Fig. 5.5 are respectively the disturbance, performance, measurement, and control signals. It is trivial to transform the block diagram in

Fig. 5.3 into the form in Fig. 5.5 by choosing

$$d = \begin{bmatrix} w \\ n \\ r \end{bmatrix} .$$

Similarly, it is trivial to transform the block diagram in Fig. 5.4 into the form in Fig. 5.5 by choosing

$$d = \begin{bmatrix} w \\ n_1 \\ n_2 \\ n_3 \\ r \end{bmatrix} , \quad y = \begin{bmatrix} y_1 \\ y_2 \end{bmatrix}$$

Since the control problem we are considering is the minimization of RMS of the  $3\sigma$  value of PES with a constraint on the mean control effort variance, we can formulate the problem as [94]

$$\begin{aligned} \min_K & \|\bar{L}_1 G_{cl}(K)\|_{\ell_{2sn}}^2 \\ \text{subject to: } & \|\bar{L}_2 G_{cl}(K)\|_{\ell_{2sn}}^2 \leq \gamma \end{aligned} \quad (5.17)$$

where  $\gamma$  is a prescribed upper bound on the mean control variance,  $G_{cl}(K)$  is the closed-loop system shown in Fig. 5.5, and the matrices  $L_1$  and  $L_2$  are chosen such that  $L_1 G_{cl}(k)$  and  $L_2 G_{cl}(K)$  respectively represent the closed-loop system from  $d$  to  $p$  and from  $d$  to  $u$ . The norm being considered in this problem is  $l_2$  semi-norm given

by

$$\|L_1 G_{cl}^{LPTV}\|_{\ell_{2sn}}^2 := \limsup_{l \rightarrow \infty} \frac{1}{2l+1} \sum_{k=-l}^l \text{tr } \mathcal{E} \left[ p_k^d (p_k^d)^T \right].$$

which, for single output systems, corresponds to the RMS standard deviation of that output signal when the input signal is white noise with covariance equal to the identity matrix. To solve this optimal control problem, we use the algorithm given by [94], which uses derivative information about the  $l_2$  semi-norm costs to achieve quasi-Newton convergence.

### 5.3.2 Probabilistic Control Design for HDD

The model of the system which described in the previous section resulted in a periodically time varying (LPTV) model of the HDD with a large period which is equal to the number of servo sectors in one revolution. As a result if we want to design an LPTV controller for the system the total number of controllers which is required to store in the memory of servo system become large. In a physical HDD, there is a limited amount of memory available to store the controller parameters and it is almost impossible to reserve so much memory for storing these parameters in real HDDs so the LPTV controller designed has some limitation in the implementation. In this section, we present an LTI  $H_2$  control design for a HDD model with irregular sampling and regular control action. We are assuming that the sampling time is uncertain parameter which in norm bounded. However by assuming uncertainty in the sampling time the problem falls into the category of the so-called "intractable" problems, which are practically unsolvable if the number of variables becomes sufficiently



large(which is the case in the HDD controller design problem). To address this issue we use the idea of probabilistic framework which described in the previous chapter in detail.

In probabilities robust control design which randomize algorithms are employed to handle uncertainty and convex optimization to compute the design parameters. We follow a two step design in order to obtain the final controller. In the first step, a classical  $H_2$  controller without considering any uncertainty is formulated. Next, we employ a randomized algorithm which called scenario approach [92, 93] to overcome the uncertainty presented in the problem. Our control objective throughout this chapter is to maximize the stability margins while keeping the position error signal, PES, as small as possible, in order to achieve high areal densities and low-readout error rates.

Consider the augmented open-loop plant shown in Fig. 5.6 with the state space representation.

$$P : \begin{bmatrix} z \\ y \end{bmatrix} = \left[ \begin{array}{c|cc} A & B_w & B_u \\ \hline C_{ew} & D_{ew} & D_{eu} \\ C_y & D_{yw} & 0 \end{array} \right] \begin{bmatrix} w \\ u \end{bmatrix} \quad (5.18)$$

The goal is to design a robust dynamic output feedback controller in the form

$$u = K(s)y = \left[ \begin{array}{c|c} A_k & B_k \\ \hline C_k & 0 \end{array} \right] y \quad (5.19)$$

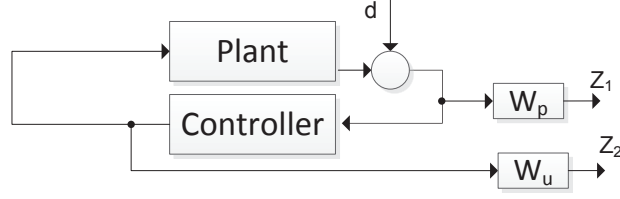


Figure 5.6: Block diagram of augmented plant for control design

which minimizes the worst case  $H_2$  norm from disturbance  $w$  to the output  $z$ . In other words, we are interested in solving the following optimization problem:

$$K = \arg \underset{K \in \mathcal{K}}{\text{minimize}} \|T_{zw}(K)\|_2 \quad (5.20)$$

where  $T_{zw}(K)$  is the closed loop transfer function from disturbance  $w$  to the output  $z$  and where  $\mathcal{K}$  is the set of all controllers that internally stabilize the closed-loop system. The optimization problem (5.20) can be reformulated in terms of linear matrix inequality (LMI) [73] as follows:

$$\underset{\mathcal{W}, \mathcal{P}, K, \gamma^2}{\text{minimize}} \gamma^2 \text{ subject to } \Omega(\mathcal{W}, \mathcal{P}, K, \gamma^2) \succ 0 \quad (5.21)$$

where

$$\Omega(\mathcal{W}, \mathcal{P}, \mathcal{K}, \gamma) = (\gamma^2 - \text{trace}(\mathcal{W})) \oplus \begin{bmatrix} \mathcal{W} & C_{cl}\mathcal{P} \\ \star & \mathcal{P} \end{bmatrix} \oplus \begin{bmatrix} \mathcal{P} & A_{cl}\mathcal{P} & B_{cl} \\ \star & \mathcal{P} & 0 \\ \star & \star & I \end{bmatrix} \succ 0 \quad (5.22)$$

where  $\mathcal{P} = \mathcal{P}^T$  and  $\mathcal{W} = \mathcal{W}^T$  are design variables and  $A_{cl}, B_{cl}$  and  $C_{cl}$  are closed loop matrixes. Introducing the uncertain in the sampling time in the formulated LMI Equation. (5.22) will make the problem extremely difficult to solve. Let us consider a set  $P^\Lambda$  of the discrete-time LTI generalized plant where  $\Lambda$  is the set of parametric uncertainties.

$$P^\Lambda : \begin{bmatrix} z \\ y \end{bmatrix} = \left[ \begin{array}{c|cc} A(\lambda) & B_w(\lambda) & B_u(\lambda) \\ \hline C_{ew}(\lambda) & D_{ew}(\lambda) & D_{eu}(\lambda) \\ C_y & D_{yw} & 0 \end{array} \right] \begin{bmatrix} w \\ u \end{bmatrix} \quad (5.23)$$

where the vector  $\Lambda \in \mathcal{R}^N$  represents an uncertain time-invariant parameter vector in an uncertainty set. the worst-case  $H_2$  performance minimization problem is rewritten as 5.24

$$\min_{K \in \mathcal{K}} \max_{\lambda \in \Lambda} \|T_{zw}(K, \lambda)\|_2 \quad (5.24)$$

This optimization problem which is known as *Worst-case design* is nonconvex, and therefore, it is difficult to solve exactly in the globally optimal sense. Obtaining worst-case solutions has been proven to be computationally hard; explicit results on the NP-hardness of several worst-case design problems are for instance found in [16, 20, 49]. In addition, a second criticism applies to a worst-case design: seeking guarantees against the worst-case can introduce undesirable conservatism in the design, since all the design focus is on a special ‘ill’ situation (the worst-case plant), which could as well be unrepresentative of the majority of admissible plants. In chapter 4

we discussed an alternative method to deal with *Worst-case design* based on probabilistic framework. Moreover two sequential stochastic algorithms based on iterative method namely gradient descent and ellipsoidal iterations is described . Although these algorithms are successful in many practical cases, these techniques present some limitations to deal with irregular sampling problem. These limitations are due to the fact that these methods are limited to convex feasibility problems, and have not yet been extended directly to deal with optimization. As a result optimal solution for the *Worst-case design* problem can be fined for certain simple dependencies of the cost function on uncertainty such as affine, polynomial or rational. In all other cases, the scenario approach offers a viable route to find a solution.

Here, we briefly study the so called scenario approach also known as random convex programs. Suppose that the goal is to solve uncertain convex problem in 5.21. For simplicity of notation Lets denoted the vector of variables as  $\theta = (\mathcal{W}, \mathcal{P}, \mathcal{K}, \gamma)$  ,  $\theta \in \Theta \subset \mathbb{R}^{n_\theta}$  . and  $f(\theta, \lambda) = eig_{max}(-\Omega(\theta, \lambda))$  and  $c^T\theta = \gamma^2$  where  $eig_{max}$  is the largest eigenvalue. So the problem 5.21 can rewrite as 5.25.

$$\begin{aligned} & \underset{\theta \in \Theta}{\text{minimize}} && c^T\theta && (5.25) \\ & \text{subject to} && f(\theta, \lambda) \leq 0 \text{ for all } \lambda \in \Lambda \end{aligned}$$

Similar to the previous probabilistic approach which describe in chapter 4, in the scenario probabilistic design paradigm we assume a probability measure *Prob* over

the uncertainty set  $\Lambda$ . Then, for a given probability level  $\epsilon \in (0, 1)$ , we seek a design parameter  $\theta$  that minimizes  $\gamma$  while satisfying all constraints but a small fraction of them whose probability is no larger than the prespecified level  $\epsilon$ . Specifically, we require that

$$\text{Prob}\{\lambda \in \Lambda \mid f(\theta, \lambda) \leq \gamma\} > 1 - \epsilon$$

It should be noted that this approach can be seen as a relaxation of the worst-case paradigm where one allows a risk level  $\epsilon$  and looks for a design parameter such that the performance specification  $f(\theta, \lambda) < \gamma$  is violated by at most a fraction  $\epsilon$  of the plants in the uncertainty family.

The reason for considering this probabilistic relaxation instead of the original worst-case design problem 5.24 is that problem 5.24 does not admit a numerically viable solution methodology in general. This section shows instead that a solution to the probabilistic design problem can be found at low computational effort, with complete generality.

One aspect that needs be remarked is that the probabilistic level  $\epsilon$  is chosen by the designer. By selecting  $\epsilon$  to be small, a design with characteristics similar to the worst-case design is obtained, while, by increasing  $\epsilon$ , a lower degree of robustness is accepted. The actual choice of the risk level  $\epsilon$  would then depend on the application at hand, and could for instance be  $10^{-6}$  if we are dealing with an airliner, or 0.01 if we are dealing with a washing machine.

Let us first specify more precisely our probabilistic setup. We assume that the support

$\Lambda$  for  $\lambda$  is endowed with a  $\sigma$ -algebra  $\mathcal{D}$  and that  $Prob$  is defined over  $\mathcal{D}$ . Moreover, we assume that  $\{\lambda \in \Lambda : f(\theta, \lambda) \leq 0\} \in \mathcal{D} \forall, \theta \in \Theta$ . Depending on the situation at hand,  $Prob$  can have different interpretations. Sometimes, it is the actual probability with which the uncertainty parameter  $\lambda$  takes on value in  $\Lambda$ . Other times,  $Prob$  simply describes the relative importance we attribute to different uncertainty instances.

We assume  $f(\theta, \lambda)$  to be convex for any fixed value of  $\lambda$ . In order to solve (5.25) using the scenario approach, we need to extract a multi-sample  $\lambda = \{\lambda^{(1)} \dots \lambda^{(N)}\}$  of cardinality  $N$  from the uncertainty set and form the following random convex program:

$$\begin{aligned} \hat{\theta}_N = \arg \underset{\theta \in \Theta}{\text{minimize}} \quad & c^T \theta \\ \text{subject to} \quad & f(\theta, \lambda^{(i)}) \leq 0, \quad i = 1, \dots, N. \end{aligned} \tag{5.26}$$

The following definition is used in order to define the probabilistic behavior of the solution obtained from (5.26).

**Definition 5.1 (Probability of Violation)** *The probability of violation of  $\theta$  for the function  $f(\theta, \lambda)$  is defined as:*

$$E_f(\theta) \doteq \text{Prob} \{ \lambda \in \Lambda : f(\theta, \lambda) > 0 \}. \tag{5.27}$$

$$\Lambda : f(\theta, \lambda) > 0 \tag{5.28}$$

The following lemma which is proved in ([95]) defines the explicit sample bound

$N$  which bounds the probability of violation of  $\widehat{\theta}_N$ .

**Lemma 5.1** *Suppose that the convexity assumption holds and let  $\delta, \varepsilon \in (0, 1)$  and  $N$  satisfy the following inequality:*

$$\sum_{i=0}^{n_\theta-1} \binom{N}{i} \varepsilon^i (1-\varepsilon)^{N-i} \leq \delta. \quad (5.29)$$

*Then if the optimization problem (5.26) is feasible with probability no smaller than  $1 - \delta$ , its optimal solution  $\widehat{\theta}_N$  satisfies  $E_f(\widehat{\theta}_N) \leq \varepsilon$ .*

There are a number of results in the literature for deriving the explicit sample size  $N$  which guarantees (5.29). The least conservative one which is reported in [93] is

$$N \geq \inf_{a>1} \frac{1}{\varepsilon} \left( \frac{a}{a-1} \right) \left( \ln \frac{1}{\delta} + (n_\theta - 1) \ln a \right). \quad (5.30)$$

The algorithm is interesting in the sense that the sample complexity (10) does not depend on the number of uncertain parameters and therefore, the computational complexity of the algorithm does not depend on the dimension of the uncertainty set, in contrast with classical robust paradigm where computational complexity grows exponentially with the number of uncertain parameters. Another interesting point about the design procedure is that no conservatism has been introduced while handling the non-linear parametric uncertainty.

## 5.4 Simulation

This section presents numerical simulation results to evaluate the performance of an HDD in track-following mode for the three sampling and actuation schemes discussed in Section 5.2. To this end, the performance results for six different system configurations are studied in this section. These configurations are different in terms of the controller used as well as the irregularity in the sampling and control rates.

In Section 5.4.1, we compare the performance of the  $H_2$ , Probabilistic and constrained  $LQG$  controllers when the sampling and actuation are both regular. We then compare these three controllers when they are applied to a system with irregular sampling and actuation in Section 5.4.1. Finally, Section 5.4.2 is dedicated to control design and performance analysis when the sampling time is irregular but the actuation rate is kept regular. Since the problem is of regulation type, the output sensitivity transfer function, which shows the ability of the system in rejecting different output disturbances, is of vital importance. For LPTV systems, frequency response methods do not apply. Despite this, we quantified the performance of the closed-loop system by using what we call an “empirical Bode magnitude plot,” which uses a swept-sine approach to find an approximate frequency response. The assumption here is that inputting a sine wave into the system produces a negligible response at other frequencies. Note that for a LTI system, the empirical Bode magnitude plot and Bode magnitude plot are equal. Since, the systems in Section 5.4.1, and Section 5.4.2 are all LPTV, the empirical Bode magnitude plot is used to show the behavior of these systems in frequency domain. The VCM model of the is described in Section



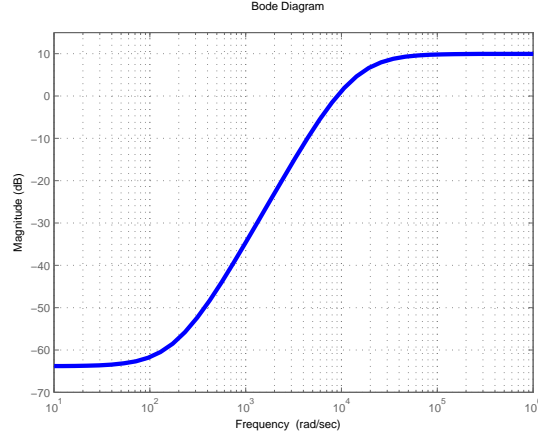


Figure 5.7: The optimal performance weighting function

2.3 is used as the plant model. The disturbance model which decribed in Section 2.5 is used in order to calculate the  $3\sigma$  value and further evaluate the track-following performance of the designed controller. Based on the method explained in Section 5.3.2 and  $H_2$  controller is designed for the plant model. We denote this controller as  $K_{H_2}$  and the closed-loop system as R-R- $K_{H_2}$ . The control weighting functions  $W_u$  is chosen to be 0.2 .The inverse of the performance weighting functions  $W_p$  used in this section is shown in Fig.5.7.

To design the probabilistic controller the time uncertainty is defined as  $t_{u,k} = \bar{t}_{u,k}(1 + 0.16\lambda)$ . We denote the probabilistic controller and the closed-loop system  $K_{prob}$  and R-R- $K_{prob}$  respectively.

The constrained LQG controller which denoted by  $K_{Lqg}$  is designed based on Section 5.3.1. Since, we are interested in comparing the performance of  $K_{Lqg}$  ,  $K_{H_2}$  and  $K_{prob}$  under the same conditions, we design  $K_{Lqg}$  such that the control effort variance of  $K_{Lqg}$  is less than or equal to the control effort variance used by  $K_{H_2}$ . Thus, we compute the control variance associate with the  $H_2$  setup and use it as a

variance constraint in the optimal  $LQG$  control design.

The bode plot of the controllers are shown in Fig. 5.8 and output sensitivity of the systems are shown in Fig. 5.9. The performance of LQG system (R-R- $K_{LQG}$ ), which is listed in Table 5.4.2, shows that the calculated  $3\sigma$  value of PES is 9% less than the corresponding value in R-R- $K_{prob}$  while the control variances are equal. Since, the PES performance of R-R- $K_{LQG}$  can be interpreted as the limit of performance when the control effort variance is less than or equal to the control effort variance used by  $K_{H_2}$ , the PES performance of R-R- $K_{LQG}$  can be used as a good metric to evaluate the performance associated with other sampling and actuation schemes.

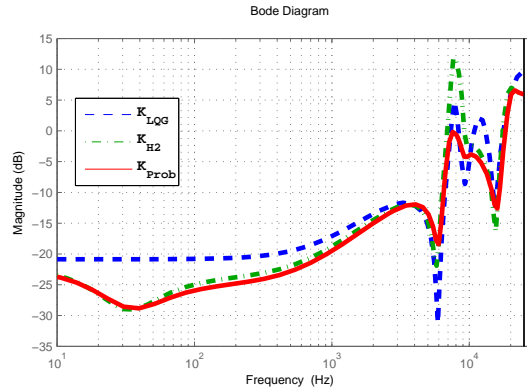


Figure 5.8: Bode diagram of controllers design for the nominal system

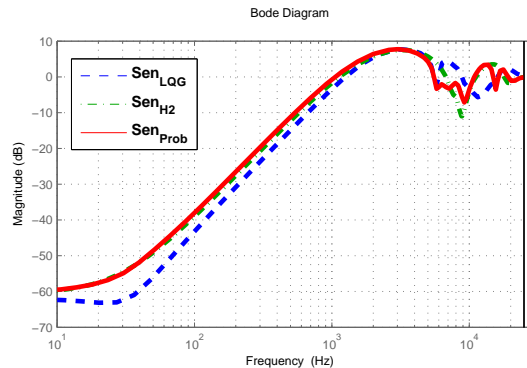


Figure 5.9: Closed loop sensitivity plot for the nominal system

### 5.4.1 Irregular Sampling and Actuation

In order to investigate the influence of irregularity on performances of the tree aforementioned controllers, the plant and disturbance models are discretized with the method explained in Section 5.2.2 so that the sampling and control update rate are both time-varying. Here, we assume that the elapsed time between successive measurements varied as  $\bar{T}(1 + 0.16 \sin(2\pi k/N))$ , where  $\bar{T}$  is the sampling time of the chosen HDD and  $k$  is the discrete-time index. The closed-loop systems containing  $K_{Lqg}$ ,  $K_{H_2}$  and  $K_{prob}$  and mentioned open-loop model is denoted as I-I- $K_{Lqg}$ , I-I- $K_{H_2}$  and I-I- $K_{prob}$  respectively. The results for these three systems are listed in Tab. 5.4.2, which show that  $K_{Lqg}$  and  $K_{H_2}$  are not stabilizing when we have 16% sampling time variation, and the performance of  $K_{prob}$  is 18% degraded. In order to demonstrate the robustness of the designed controller we extracted 500 random samples from the uncertainty set and formed the error rejection (sensitivity) transfer function for each random realizations. Fig.5.11 shows the obtained sensitivity transfer function for 500 uncertain scenarios. As it is clear, the sensitivity transfer function does not degrade over the uncertainty set which proves the robustness of the designed controller. Fig. 5.12 shows that the controller for the nominal plant tend to instability for some uncertain realizations.

We now examine the limits of performance of this system architecture by designing an optimal LQG controller with the same variance constraint as  $K_{Lqg}$  for the LPTV open-loop model. We denote the closed-loop system corresponding to this controller as I-I- $K_{Lptv}$ . The performance of this system listed in Tab. 5.4.2 shows that the

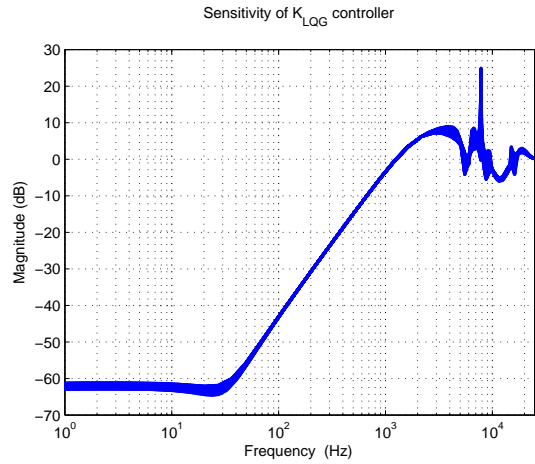


Figure 5.10: Closed loop sensitivity plot for 500 random realizations for the system with  $K_{LQG}$  controller

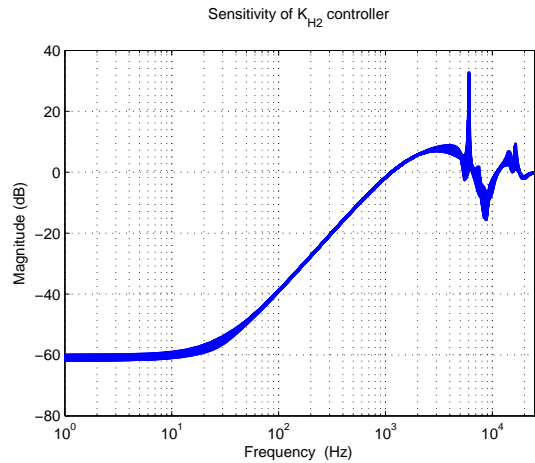


Figure 5.11: Closed loop sensitivity plot for 500 random realizations for the system with probabilistic  $H_2$  controller

LPTV LQG controller gives closed-loop PES performance almost equal to the limit of performance for regular sampling and actuation, which is 7% better than achieved by probabilistic LTI controller. Figure 5.13 shows the empirical Bode magnitude plots for the sensitivity function of I-I- $K_{prob}$  and I-I- $K_{Lptv}$  measured at the output of the controller.

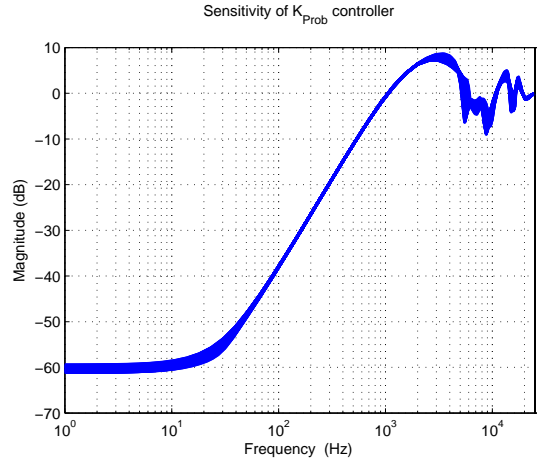


Figure 5.12: Closed loop sensitivity plot for 500 random realizations for the system with nominal  $H_{Prob}$  controller

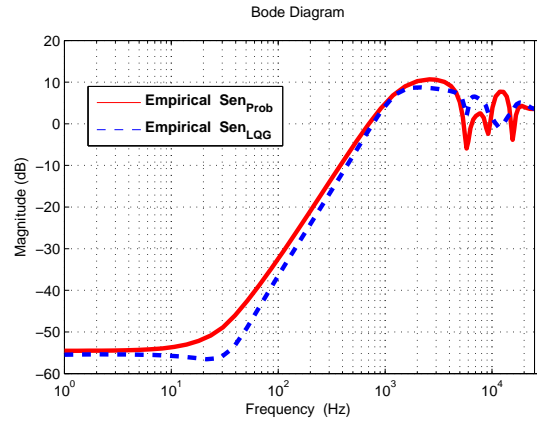


Figure 5.13: Empirical Bode magnitude plot of the sensitivity function for  $I - I - K_{prob}$  and  $I - I - K_{LPTV}$  controller

## 5.4.2 Irregular Sampling and Regular Actuation

All the six aforementioned systems are dealing with sampling time and control update rate that are either both time-varying or both time-invariant. As explained in Section 5.2.3, we are interested in designing a controller with a constant update rate for a system with an irregular sampling time. To evaluate the performance of a LPTV LQG and probabilistic controller, the continuous-time plant model used for previous cases is discretized by the method discussed in Section 5.2.3, i.e. the state and

control updates in this system are occurring regularly while the measurement arrives irregularly. The limit of performance of the closed-loop system, which is denoted as I-R- $K_{Lptv2}$ , is listed in Tab. 5.4.2. These results show that the optimal  $3\sigma$  value of PES for the I-R- $K_{H_{prob}}$  architecture is 6% larger than limit of performance. However it should be emphasize that the main advantage of the probabilistic approach is to stabilizing the system with an LTI controller and achieves an acceptable level of the performance at the same time. Moreover the open-loop plant with regular sampling time and irregular control has more than one component in the signal  $y$ , we have only used the most updated value in the  $K_{H_{prob}}$  controller. Fig. 5.14 shows the empirical Bode magnitude plots of I-R- $K_{LptvLqg2}$  and I-R- $K_{H_{Prob}}$ . The nominal and worst case stability margins (phase and gain margins) are evaluated and compared to the designed nominal and probabilistic controller and the results which are shown in Table.5.2.

Design Approach	TMR (nm)		RMS( $u_V$ ) (mV)		$\ u_V\ _\infty$ (mV)	
	Nominal	Worst Case	Nominal	Worst Case	Nominal	Worst Case
R-R- $K_{H2}$	8.95	-	13.7	-	72.4	-
R-R- $K_{H_{Prob}}$	9.12	-	12.4	-	67.9	-
R-R- $K_{Lqg}$	8.29	-	12.8	-	72.4	-
I-I- $K_{H_{Prob}}$	10.48	12.37	11.3	12.8	67.9	69.2
I-I- $K_{LqgLptv}$	9.74	10.13	10.7	13.7	67.9	72.4
I-R- $K_{H_{Prob2}}$	10.21	11.87	11.9	13.1	67.9	69.2
I-R- $K_{LqgLptv2}$	9.45	9.87	11.3	13.7	55.7	72.4

Table 5.1: Comparison of the nominal and worst case performance specifications

Design Approach	Gain Margin (dB)		Phase Margin (Degree)	
	Nominal	Worst Case	Nominal	Worst Case
$R-R-K_{H_2}$	8.95	-	50.66	-
$R-R-K_{H_{Prob}}$	7.45	-	40.81	-
$R-R-K_{Lqg}$	7.16	-	30.63	-
$I-I-K_{Prob}$	6.93	6.16	35.43	32.19
$I-I-K_{LqgLptv}$	6.22	5.94	27.31	25.47
$I-R-K_{H_{Prob2}}$	7.12	6.86	36.77	33.46
$I-R-K_{LqgLptv2}$	6.77	6.21	30.85	27.19

Table 5.2: Comparison of the nominal and worst case stability margins

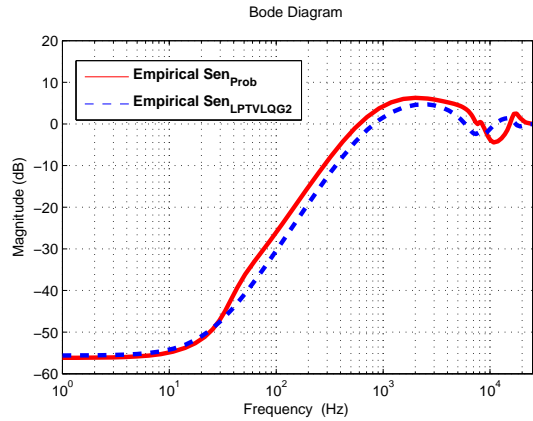


Figure 5.14: Closed loop sensitivity function at the output of the controller for LPTV and nominal plant

## 5.5 Conclusion

In this chapter, we have evaluated and compare the effect of various sampling and actuation schemes on the performance of the system. In section 2 we present a method of discretizing the continuous-time plant dynamics. For the regular measurement and control update scheme and the irregular measurement and control update scheme, the discretization process did not introduce any addition states into the state space model. For the scheme with irregular measurements and regular control updates, the discretization process did introduce  $n_u$  additional states into the state space model. These additional states were unavoidable essentially because in the worst-case sce-

nario, the computational delay causes there to be more than a full step delay between when a measurement arrives and when the controller can use that measurements to update the control signal.

In Section 3 we used a controller design based on LPTV approach to investigate the limits of performance for different schemes. However in a physical HDD, there is a limited amount of memory available to store the controller parameters. As a result, the controllers designed in section Section 5.3.1 are not directly suitable for implementation. To address this limitation this section followed by a probabilistic scenario approach to design an LTI robust controller. We evaluated the performance using a model of the system that included a detailed model of the stochastic disturbances acting on the system.

For the HDD considered in this section, there is significant performance degradation from the regular sampling case to the irregular sampling and irregular control action case. In other words, if there is significant variation in the sample period over a revolution of the disk, simply ignoring that variation and using an LTI controller can lead to significant degradation in performance. Also, it turns out that the irregular sampling and regular actuation configuration achieved a smaller RMS  $3\sigma$  PES value than the irregular sampling and actuation configuration. This means that, although we are primarily interested in the irregular sampling and the regular actuation configuration because it does not complicate the design of notch filters for the plant, this configuration turns out to yield better performance than the irregular sampling and actuation configuration for this particular system.



# Chapter 6

## Conclusions and Future Works

In this thesis, several challenges on the control design of nano-positioning systems are studied. We mainly focus on the robust control design for HDD servo system. This chapter concludes the thesis with the summary of the main contributions and provides possible future research directions.

### 6.1 Conclusion

(a) **Integral resonant control to suppress micro-actuator resonance:**

An effective method of suppressing vibration of flexible modes of a piezoelectric micro-actuator based on the principle of the integral resonant control was presented. IRC concept applied to compensate the main resonant mode of the secondary stage of dual-stage actuation. An extended decoupling sensitivity method was proposed to accommodate the configuration of IRC in a dual-stage controller design.

Its effectiveness was verified with the help of simulation and experimental results. It was demonstrated that the performance of a 1st-order IRC compensator in suppressing resonances is comparable to the conventional approach using a much higher order notch filter. Besides the performance improvement, other benefits of the proposed controller include ease of implementation and robustness. IRC controller permits an increase in the worst-case stability margins for the variation in the plant model.

(b) **Probabilistic approach for design of robust control:**

A discrete-time multi-objective robust controller is designed in a probabilistic framework. An iterative algorithm based on ellipsoid iteration was used to find the probabilistic robust feasible solution for track following controller in the HDD. The design is less conservative compared to classical robust approaches. Firstly, in spite of the classical robust paradigm where uncertain nonlinear parameters are embedded into a larger affine structure, in a probabilistic framework, these parameters are treated as they are. Secondly, multiple Lyapunov matrixes were used for different objectives of the robustness and performance. In probabilistic designs, by allowing a small probability that the objective function being violated, the performance of the resulting controller is simpler and the worst-case performance is close to the nominal system. The computational complexity of the algorithm is based on a priori bounds, which depend only on probabilistic levels  $\epsilon$  and confidence  $\delta$ . Therefore, the computational complexity does not increase with the number of uncertain parameters at the expense

of accepting probabilistic risk terms which can be arbitrarily small. The effectiveness of the designed controller is verified through extensive simulations and experiments. Our case study allows natural frequency and damping ratio to vary within 8% and 10% from their nominal values for rigid body and all resonance modes. The designed controller achieves robustness in the presence of these uncertainties.

(c) **Design controller under irregular sampling:**

A novel method of discretizing the continuous-time plant dynamics was presented. For the regular measurement and control update scheme and the irregular measurement and control update scheme, the discretization process does not introduce any additional states in the state space model. For the scheme with irregular measurements and regular control updates, the discretization process introduces  $n_u$  additional states in the state space model. These additional states are unavoidable essentially; because in the worst-case scenario, the computational delay causes there to be more than a full step delay between when a measurement arrives and when the controller can use that measurement to update the control signal. Next, controller design based on LPTV approach was evaluated to investigate the limits of performance for different sampling schemes. The LPTV controller designed has some limitations on the implementation of a commercial HDD. Since, in LPTV design the total number of controllers, which is required to store the memory of servo system, is equal to the number of servo sectors in one revolution. On the other hand, there is a

limited amount of memory available to store the controller parameters. A robust LTI probabilistic  $H_2$  control design methodology under irregular sampling was proposed. This approach is based on a non-sequential randomized technique, called scenario probabilistic design. In simulations, the performance of the system was verified using a detailed model of the stochastic disturbances acting on the system. Our proposed approach consistently outperformed their conventional counterparts and offered improvements in the robust performance.

## 6.2 Future Works

### (a) **Integral resonant control to suppress micro-actuator resonance:**

Although IRC scheme presented in this thesis was found to be more robust than conventional notch filter method for suppressing resonance, it has its own limitations. It cannot deal with multiple resonance mode uncertainty in a MIMO structure. In [65] Bhikkaji et al presented an extension of the IRC technique to resonant MIMO systems based on LMI approach. However, the procedure proposed in the paper for designing IRC controllers involves minimizing a non-linear nonconvex cost function over a convex set. The nonconvex nature of the cost function makes the control design heavily reliant on the initial guess or the starting point of the nonlinear search used for minimizing the cost function. Moreover, there is no systematical way to guarantee the robust stability for the MIMO case. Using the idea of randomized algorithms, the original nonconvex problem can change to convex and solve more efficiently.

The IRC compensator proposed in this thesis is partially restricted in a necessary condition on the nature of the zeros of micro-actuator transfer function, as it assumes the gains of each resonant mode to be positive ( $A_i > 0$ ). The micro-actuator used here for experimental verification conforms to this restriction. Further research should be carried out to investigate the effects of negative  $A_i$  in general case.

(b) **Probabilistic approach for design of robust control:**

One interesting direction for further investigation into the probabilistic controller design is to decouple robustness and stability. Randomized algorithm and violation function applied to evaluate both stability on robustness. In other words, when the valuation function becomes negative, there is no way to distinguish between stability or robustness violation. Further research should be carried out to determine the stability of the system in deterministic manner and robustness in probabilistic one.

In the probabilistic controller design presented in this thesis uniform probability distribution is assumed in the sampling of the uncertainty space. However, uniform probability distribution is the worst case scenario. It is an acceptable assumption when there is not enough data available to characterize the distribution form of the uncertainty set. In case of HDD since a wide set of samples are available; One can find the exact form of uncertainty distribution. As a result, the performance of the controller and overall system would improve.

(c) **Design controller under irregular sampling:**

It would be an interesting problem to consider the effect of variation in the plant model (parametric uncertainty) and variation in the sampling time (irregular sampling) concurrently. However by considering such uncertainty set the problem is not convex or linear anymore since there are plenty of coupling term in the optimization equations. To the best of author knowledge in general there is not a simple solution for this type of problem. However it would be a good extension of ideas proposed in this thesis to perform and find a heuristic approach to find sub-optimal controller with a reasonable performance against variation in plant model and irregular sampling.

# Bibliography

- [1] B. Shapiro, “Control and system integration of micro-and nano-scale systems,” *IEEE Control Syst. Mag*, vol. 25, pp. 82–8, 2005.
- [2] B. Bhushan, *Springer handbook of nanotechnology*. Springer, 2010.
- [3] S. Devasia, E. Eleftheriou, and S. Moheimani, “A survey of control issues in nanopositioning,” *Control Systems Technology, IEEE Transactions on*, vol. 15, no. 5, pp. 802–823, 2007.
- [4] G. Binnig and H. Rohrer, “Scanning tunneling microscopy,” *IBM Journal of research and development*, vol. 44, no. 1-2, pp. 279–293, 2000.
- [5] G. Binnig, C. F. Quate, and C. Gerber, “Atomic force microscope,” *Physical review letters*, vol. 56, no. 9, p. 930, 1986.
- [6] M. Yves, “Scanning probe microscopes,” *Bellingham, WA: SPIE*, 1995.
- [7] L. R. Harriott, “Limits of lithography,” *Proceedings of the IEEE*, vol. 89, no. 3, pp. 366–374, 2001.

- [8] J. Fasik, “An inchworm actuator for the next generation space telescope,” *Burleigh Instruments, Inc., Fishers, NY*, 1998.
- [9] S. Verma, W.-j. Kim, and H. Shakir, “Multi-axis maglev nanopositioner for precision manufacturing and manipulation applications,” *Industry Applications, IEEE Transactions on*, vol. 41, no. 5, pp. 1159–1167, 2005.
- [10] A. Sebastian and S. M. Salapaka, “Design methodologies for robust nanopositioning,” *Control Systems Technology, IEEE Transactions on*, vol. 13, no. 6, pp. 868–876, 2005.
- [11] S. Bashash and N. Jalili, “Robust adaptive control of coupled parallel piezoflexural nanopositioning stages,” *Mechatronics, IEEE/ASME Transactions on*, vol. 14, no. 1, pp. 11–20, 2009.
- [12] C. K. Pang, G. Guo, B. M. Chen, and T. H. Lee, “Nanoposition sensing and control in hdd dual-stage servo systems,” in *Control Applications, 2004. Proceedings of the 2004 IEEE International Conference on*, vol. 1. IEEE, 2004, pp. 551–556.
- [13] A. A. Mamun, I. Mareels, T. H. Lee, and A. Tay, “Dual stage actuator control in hard disk drive - a review,” in *Industrial Electronics Society, 2003. IECON '03. The 29th Annual Conference of the IEEE*, vol. 3, 2003, pp. 2132 – 2137 Vol.3.
- [14] L. Xiao and D. Hu, “Research on high density data storage technology,” in *Eighth International Symposium on Optical Storage and 2008 International Workshop*



## BIBLIOGRAPHY

---

- on Information Data Storage*. International Society for Optics and Photonics, 2008, pp. 712 529–712 529.
- [15] A. A. Mamun, G. Guo, and C. Bi, *Hard Disk Drive: Mechatronics and Control*, 1st ed. CRC Press, Nov. 2006.
- [16] B. M. Chen, *Hard disk drive servo systems*. Springer, 2006.
- [17] J. Manyika, M. G. Institute, M. Chui, B. Brown, J. Bughin, R. Dobbs, C. Roxburgh, and A. H. Byers, *Big data: The next frontier for innovation, competition, and productivity*. McKinsey Global Institute, 2011.
- [18] C. Thum, C. Du, B. Chen, E. Ong, and K. Tan, “A unified control scheme for track seeking and following of a hard disk drive servo system,” *Control Systems Technology, IEEE Transactions on*, vol. 18, no. 2, pp. 294–306, 2010.
- [19] W. Lan, C. Thum, and B. Chen, “A hard-disk-drive servo system design using composite nonlinear-feedback control with optimal nonlinear gain tuning methods,” *Industrial Electronics, IEEE Transactions on*, vol. 57, no. 5, pp. 1735–1745, 2010.
- [20] T. Suthasun, I. Mareels, and A. Al-Mamun, “System identification and controller design for dual actuated hard disk drive,” *Control engineering practice*, vol. 12, no. 6, pp. 665–676, 2004.
- [21] C. Kang and C. Kim, “An adaptive notch filter for suppressing mechanical resonance in high track density disk drives,” *Microsystem technologies*, vol. 11, no. 8, pp. 638–652, 2005.

- [22] K. Ohno and T. Hara, "Adaptive resonant mode compensation for hard disk drives," *Industrial Electronics, IEEE Transactions on*, vol. 53, no. 2, pp. 624–630, 2006.
- [23] D. Wu, G. Guo, and T.-C. Chong, "Adaptive compensation of microactuator resonance in hard disk drives," *Magnetics, IEEE Transactions on*, vol. 36, no. 5, pp. 2247–2250, 2000.
- [24] P. Weaver and R. Ehrlich, "The use of multirate notch filters in embedded-servo disk drives," in *American Control Conference, 1995. Proceedings of the*, vol. 6. IEEE, 1995, pp. 4156–4160.
- [25] J. Hyde and W. Seering, "Using input command pre-shaping to suppress multiple mode vibration," in *Robotics and Automation, 1991. Proceedings., 1991 IEEE International Conference on*. IEEE, 1991, pp. 2604–2609.
- [26] S.-M. Suh, C. C. Chung, and S.-H. Lee, "Discrete-time lqg/ltr dual-stage controller design in magnetic disk drives," *Magnetics, IEEE Transactions on*, vol. 37, no. 4, pp. 1891–1895, 2001.
- [27] X. Chen and M. Tomizuka, "A minimum parameter adaptive approach for rejecting multiple narrow-band disturbances with application to hard disk drives," *Control Systems Technology, IEEE Transactions on*, vol. 20, no. 2, pp. 408–415, 2012.

- [28] P. P. San, B. Ren, S. S. Ge, T. H. Lee, and J.-K. Liu, “Adaptive neural network control of hard disk drives with hysteresis friction nonlinearity,” *Control Systems Technology, IEEE Transactions on*, vol. 19, no. 2, pp. 351–358, 2011.
- [29] S.-C. Wu and M. Tomizuka, “An iterative learning control design for self-servowriting in hard disk drives,” *Mechatronics*, vol. 20, no. 1, pp. 53–58, 2010.
- [30] R. Conway and R. Horowitz, “Guaranteed cost control for linear periodically time-varying systems with structured uncertainty and a generalized h2 objective,” *Mechatronics*, vol. 20, no. 1, pp. 12–19, 2010.
- [31] R. Nagamune, X. Huang, and R. Horowitz, “Robust control synthesis techniques for multirate and multisensing track-following servo systems in hard disk drives,” *Journal of dynamic systems, measurement, and control*, vol. 132, no. 2, p. 021005, 2010.
- [32] T. Namerikawa and M. Fujita, “Uncertainty structure and mu-synthesis of a magnetic suspension system,” *TRANSACTIONS-INSTITUTE OF ELECTRICAL ENGINEERS OF JAPAN C*, vol. 121, no. 6, pp. 1080–1087, 2001.
- [33] A. Nemirovskii, “Several NP-hard problems arising in robust stability analysis,” *Mathematics of Control, Signals, and Systems*, vol. 6, no. 2, pp. 99–105, Jun. 1993.
- [34] J. G. VanAntwerp and R. D. Braatz, “A tutorial on linear and bilinear matrix inequalities,” *Journal of Process Control*, vol. 10, no. 4, pp. 363–385, Aug. 2000.

## BIBLIOGRAPHY

---

- [35] O. Toker and H. Ozbay, “On the NP-hardness of solving bilinear matrix inequalities and simultaneous stabilization with static output feedback,” in *American Control Conference, 1995. Proceedings of the*, vol. 4, 1995, pp. 2525–2526 vol.4.
- [36] R. Conway, J. Choi, R. Nagamune, and R. Horowitz, “Robust Track-Following controller design in hard disk drives based on parameter dependent lyapunov functions,” *Magnetics, IEEE Transactions on*, vol. 46, no. 4, pp. 1060–1068, Apr. 2010.
- [37] H. Mutoh, “Magnetic bit-patterned disk and disk drive,” Mar. 17 2010, uS Patent App. 12/726,270.
- [38] J. Nie, E. Sheh, and R. Horowitz, “Optimal h control design and implementation of hard disk drives with irregular sampling rates,” *IEEE transactions on control systems technology*, vol. 20, no. 2, pp. 402–407, 2012.
- [39] R. Ehrlich, “Methods for improving servo-demodulation robustness,” Sep. 13 2005, uS Patent 6,943,981.
- [40] D. Abramovitch, T. Hurst, and D. Henze, “An overview of the pes pareto method for decomposing baseline noise sources in hard disk position error signals,” *Magnetics, IEEE Transactions on*, vol. 34, no. 1, pp. 17–23, 1998.
- [41] P. A. Ioannou, H. Xu, and B. Fidan, “Identification and high bandwidth control of hard disk drive servo systems based on sampled data measurements,” *Control Systems Technology, IEEE Transactions on*, vol. 15, no. 6, pp. 1089–1095, 2007.

- [42] A. Al Mamun, T. Lee, and T. Low, “Frequency domain identification of transfer function model of a disk drive actuator,” *Mechatronics*, vol. 12, no. 4, pp. 563–574, 2002.
- [43] E. Keikha, A. Al Mamun, T. H. Lee, and C. S. Bhatia, “Multi-frequency technique for frequency response measurement and its application to servo system with friction,” in *World Congress*, vol. 18, no. 1, 2011, pp. 5273–5278.
- [44] R. Conway, S. Felix, and R. Horowitz, “Model reduction and parametric uncertainty identification for robust  $H_2$  control synthesis for dual-stage hard disk drives,” *Magnetics, IEEE Transactions on*, vol. 43, no. 9, pp. 3763–3768, 2007.
- [45] S. Skogestad and I. Postlethwaite, *Multivariable feedback control: analysis and design*. Wiley, 2007, vol. 2.
- [46] R. Conway, J. Choi, R. Nagamune, and R. Horowitz, “Robust track-following controller design in hard disk drives based on parameter dependent Lyapunov functions,” *Magnetics, IEEE Transactions on*, vol. 46, no. 4, pp. 1060–1068, 2010.
- [47] F. Hong and C. K. Pang, “Robust vibration control at critical resonant modes using indirect-driven self-sensing actuation in mechatronic systems,” *ISA transactions*, 2012.
- [48] X. Huang, R. Nagamune, and R. Horowitz, “A comparison of multirate robust track-following control synthesis techniques for dual-stage and multisensing servo

- systems in hard disk drives,” *Magnetics, IEEE Transactions on*, vol. 42, no. 7, pp. 1896–1904, 2006.
- [49] U. Boettcher, R. A. D. Callafon, and F. E. Talke, “Modeling and control of a dual stage actuator hard disk drive,” *Journal of Advanced Mechanical Design, Systems, and Manufacturing*, vol. 4, no. 1, pp. 107–118, 2010.
- [50] S. Chatterjee, “Vibration control by recursive time-delayed acceleration feedback,” *Journal of Sound and Vibration*, vol. 317, no. 1, pp. 67–90, 2008.
- [51] K. Alhazza, A. Nayfeh, and M. Daqaq, “On utilizing delayed feedback for active-multimode vibration control of cantilever beams,” *Journal of Sound and Vibration*, vol. 319, no. 3, pp. 735–752, 2009.
- [52] F. Huang, T. Semba, W. Imaino, and F. Lee, “Active damping in hdd actuator,” *Magnetics, IEEE Transactions on*, vol. 37, no. 2, pp. 847–849, 2001.
- [53] S. Lee, C. Chung, and C. Lee, “Active high-frequency vibration rejection in hard disk drives,” *Mechatronics, IEEE/ASME Transactions on*, vol. 11, no. 3, pp. 339–345, 2006.
- [54] C. Pang, G. Guo, B. Chen, and T. Lee, “Self-sensing actuation for nanopositioning and active-mode damping in dual-stage hdds,” *Mechatronics, IEEE/ASME Transactions on*, vol. 11, no. 3, pp. 328–338, 2006.
- [55] J. Fanson and T. Caughey, “Positive position feedback control for large space structures,” *AIAA Journal*, vol. 28, pp. 717–724, 1990.

- [56] G. Song, S. Schmidt, and B. Agrawal, “Experimental robustness study of positive position feedback control for active vibration suppression,” *Journal of guidance, control, and dynamics*, vol. 25, no. 1, pp. 179–182, 2002.
- [57] H. Pota, S. Moheimani, and M. Smith, “Resonant controllers for smart structures,” *Smart Materials and Structures*, vol. 11, no. 1, p. 1, 2002.
- [58] S. Aphale, A. Fleming, and S. Moheimani, “Integral resonant control of collocated smart structures,” *Smart Materials and Structures*, vol. 16, no. 2, p. 439, 2007.
- [59] B. Bhikkaji and S. Moheimani, “Integral resonant control of a piezoelectric tube actuator for fast nanoscale positioning,” *Mechatronics, IEEE/ASME Transactions on*, vol. 13, no. 5, pp. 530–537, 2008.
- [60] A. Fleming, S. Aphale, and S. Moheimani, “A new method for robust damping and tracking control of scanning probe microscope positioning stages,” *Nanotechnology, IEEE Transactions on*, vol. 9, no. 4, pp. 438–448, 2010.
- [61] E. Pereira, S. Aphale, V. Feliu, and S. Moheimani, “Integral resonant control for vibration damping and precise tip-positioning of a single-link flexible manipulator,” *Mechatronics, IEEE/ASME Transactions on*, vol. 16, no. 2, pp. 232–240, 2011.
- [62] S. Kuiper and G. Schitter, “Active damping of a piezoelectric tube scanner using self-sensing piezo actuation,” *Mechatronics*, vol. 20, no. 6, pp. 656–665, 2010.

- [63] R. Horowitz, Y. Li, K. Oldham, S. Kon, and X. Huang, “Dual-stage servo systems and vibration compensation in computer hard disk drives,” *Control Engineering Practice*, vol. 15, no. 3, pp. 291–305, 2007.
- [64] A. Al-Mamun, E. Keikha, C. S. Bhatia, and T. H. Lee, “Integral resonant control for suppression of resonance in piezoelectric micro-actuator used in precision servomechanism,” *Mechatronics*, 2012.
- [65] B. Bhikkaji, S. R. Moheimani, and I. R. Petersen, “Multivariable integral control of resonant structures,” in *Decision and Control, 2008. CDC 2008. 47th IEEE Conference on*. IEEE, 2008, pp. 3743–3748.
- [66] G. Zames, “Feedback and optimal sensitivity: Model reference transformations, multiplicative seminorms, and approximate inverses,” *Automatic Control, IEEE Transactions on*, vol. 26, no. 2, pp. 301–320, 1981.
- [67] A. Packard and J. Doyle, “The complex structured singular value,” *Automatica*, vol. 29, no. 1, pp. 71–109, Jan. 1993.
- [68] S. P. Bhattacharyya, H. Chapellat, and L. H. Keel, *Robust Control: The Parametric Approach*. Upper Saddle River: Prentice Hall, 1995.
- [69] S. Boyd, L. E. Ghaoui, E. Feron, and V. Balakrishnan, *Linear Matrix Inequalities in System and Control Theory*. Philadelphia: SIAM, 1994.
- [70] D. Bernstein and W. Haddad, “Lqg control with an  $\ell_1$   $h_2$  performance bound: a riccati equation approach,” *Automatic Control, IEEE Transactions on*, vol. 34, no. 3, pp. 293–305, 1989.



- [71] C. Scherer, P. Gahinet, and M. Chilali, “Multiobjective output-feedback control via LMI optimization,” *Automatic Control, IEEE Transactions on*, vol. 42, no. 7, pp. 896–911, 1997.
- [72] M. de Oliveira, J. Bernussou, and J. Geromel, “A new discrete-time robust stability condition,” *Systems & control letters*, vol. 37, no. 4, pp. 261–265, 1999.
- [73] M. De Oliveira, J. Geromel, and J. Bernussou, “Extended  $h_2$  and  $h_\infty$  norm characterizations and controller parametrizations for discrete-time systems,” *International Journal of Control*, vol. 75, no. 9, pp. 666–679, 2002.
- [74] S. Kanev, C. Scherer, M. Verhaegen, and B. D. Schutter, “Robust output-feedback controller design via local BMI optimization,” *Automatica*, vol. 40, no. 7, pp. 1115–1127, Jul. 2004.
- [75] G. Calafiore, F. Dabbene, and R. Tempo, “A survey of randomized algorithms for control synthesis and performance verification,” *Journal of Complexity*, vol. 23, no. 3, pp. 301–316, 2007.
- [76] M. Vidyasagar, “Randomized algorithms for robust controller synthesis using statistical learning theory,” *Automatica*, vol. 37, no. 10, pp. 1515–1528, Oct. 2001.
- [77] G. Calafiore and B. T. Polyak, “Stochastic algorithms for exact and approximate feasibility of robust LMIs,” *Automatic Control, IEEE Transactions on*, vol. 46, no. 11, p. 1755–1759, 2001.

- [78] S. Kanev, B. D. Schutter, and M. Verhaegen, “An ellipsoid algorithm for probabilistic robust controller design,” *Systems & Control Letters*, vol. 49, no. 5, pp. 365–375, Aug. 2003.
- [79] F. Dabbene, P. S. Shcherbakov, and B. T. Polyak, “A randomized cutting plane method with probabilistic geometric convergence,” *SIAM Journal on Optimization*, vol. 20, no. 6, p. 3185, 2010.
- [80] R. Tempo, G. Calafiore, and F. Dabbene, *Randomized Algorithms for Analysis and Control of Uncertain Systems*. Springer-Verlag London Limited, 2005.
- [81] G. C. Calafiore, F. Dabbene, and R. Tempo, “Research on probabilistic methods for control system design,” *Automatica*, vol. In Press, Corrected Proof, 2011.
- [82] J. Lofberg, “Yalmip: A toolbox for modeling and optimization in matlab,” in *Computer Aided Control Systems Design, 2004 IEEE International Symposium on*. IEEE, 2004, pp. 284–289.
- [83] B. T. Polyak and R. Tempo, “Probabilistic robust design with linear quadratic regulators,” *Systems & Control Letters*, vol. 43, no. 5, pp. 343–353, Aug. 2001.
- [84] R. Tempo, E. Bai, and F. Dabbene, “Probabilistic robustness analysis: explicit bounds for the minimum number of samples,” in *Decision and Control, 1996., Proceedings of the 35th IEEE*, vol. 3, 1996, pp. 3424–3428 vol.3.
- [85] A. Tremba, G. Calafiore, F. Dabbene, E. Gryazina, B. Polyak, P. Shcherbakov, and R. Tempo, “RACT: randomized algorithms control toolbox for MATLAB,” in *Proc. 17th World Congress of IFAC, Seoul*, 2008, p. 390–395.

## BIBLIOGRAPHY

---

- [86] J. Löfberg, “YALMIP : A toolbox for modeling and optimization in MATLAB,” in *Proceedings of the CACSD Conference*, 2004.
- [87] A. Sala, “Computer control under time-varying sampling period: An lmi gridding approach,” *Automatica*, vol. 41, no. 12, pp. 2077–2082, 2005.
- [88] Y. Wang and G. Yang, “Output tracking control for networked control systems with time delay and packet dropout,” *International Journal of Control*, vol. 81, no. 11, pp. 1709–1719, 2008.
- [89] V. Suplin, E. Fridman, and U. Shaked, “H sampled data control of systems with time-delays,” *International Journal of Control*, vol. 82, no. 2, pp. 298–309, 2009.
- [90] H. Gao, J. Wu, and P. Shi, “Robust sampled-data h control with stochastic sampling,” *Automatica*, vol. 45, no. 7, pp. 1729–1736, 2009.
- [91] R. Nagamune, X. Huang, and R. Horowitz, “Robust control synthesis techniques for multirate and multisensing Track-Following servo systems in hard disk drives,” *Journal of Dynamic Systems, Measurement, and Control*, vol. 132, no. 2, pp. 021 005–10, Mar. 2010.
- [92] G. Calafiore and M. C. Campi, “Robust convex programs: Randomized solutions and applications in control,” in *Decision and Control, 2003. Proceedings. 42nd IEEE Conference on*, vol. 3, 2004, p. 2423–2428.
- [93] G. Calafiore and M. Campi, “The scenario approach to robust control design,” *IEEE Transactions on Automatic Control*, vol. 51, no. 5, pp. 742–753, May 2006.

## BIBLIOGRAPHY

---

- [94] R. Conway and R. Horowitz, “A quasi-newton algorithm for lqg controller design with variance constraints,” *Proceedings of the DSCC*, 2008.
  
- [95] T. Alamo, R. Tempo, and A. Luque, “On the sample complexity of probabilistic analysis and design methods,” *Perspectives in Mathematical System Theory, Control, and Signal Processing*, pp. 39–50, 2010.

# List of Publications

## Journal Papers

- A. A. Mamun, **E. Keikha**, C. S. Bhatia, T. H. Lee “Integral resonant control for suppression of resonance in piezoelectric micro-actuator used in precision servomechanism” *Mechatronics Elsevier Journals* Volume 23, Issue 1, pp. 1-9, February 2013.
- A. A. Mamun, **E. Keikha**, C. S. Bhatia, T. H. Lee, “Integral Resonant Control for Suppression of Micro-Actuator Resonance in Dual Stage Actuator,” *IEEE Transactions on Magnetics*, Volume 48, Issue 11, pp. 4614-4617, Nov. 2012.
- M. Chamnabaz, **E. Keikha**, V. Venkataramanan, A. A. Mamun, Q.-G. Wang, Y. F. Liew “Design of a Probabilistic Robust Track-Following Controller for Hard Disk Drive Servo Systems” to be appear in *Mechatronics Elsevier Journals*
- B. Shahsavari, R. Conway, **E. Keikha**, F. Zhang, and R. Horowitz “Robust Track-Following Controller Design for Hard Disk Drives With Irregular Sampling” *IEEE Transactions on Magnetics*, Volume 49, Issue 6, pp. 2798-2804,

2013.

## Conference Papers

- **E. Keikha** B. Shahsavari, Fu Zhang, A. A. Mamun, and R. Horowitz “An Evaluation of HDD Servo System Performance with Irregular Sampling Rate” in *23rd ASME Annual Conference on Information Storage and Process Systems (ISPS'13)*, Santa Clara University 2013.
- **E. Keikha**, B. Shahsavari, A. A. Mamun, and R. Horowitz “A probabilistic approach to robust controller design for a servo system with irregular sampling” in *IEEE International Conference on Control and Automation Hangzhou, China*, 2013.
- B. Shahsavari, R. Conway, **E. Keikha** and R. Horowitz “Limits of Performance in Systems with Periodic Irregular Sampling and Actuation Rates” *The 6th IFAC Symposium on Mechatronic Systems (Mechatronics '13)* Hangzhou, China, 2013 , pp. 347-354.
- B. Shahsavari, R. Conway, **E. Keikha** and R. Horowitz “Robust Control Design for Hard Disk Drives with Irregular Sampling” in *The Asia-Pacific Magnetic Recording Conference (APMRC)* Singapore ,2012. pp. 1-2.
- **E. Keikha**, D. Zonoobi, A. Kassim, A. A. Mamun, C. S. Bhatia “A Track following Controller design based on Compressive Sensing Approach” in *2012*

## BIBLIOGRAPHY

---

*ASME-ISPS joint international conference on Mechatronics for information and precession equipment* Santa Clara, 2012.

- M.Chamnabaz, **E. Keikha**, V. Venkataramanan, Q.-G. Wang , A. A. Mamun “ Probabilistic Robust Approach for Discrete Multi-objective Control of Track-Following Servo Systems in Hard Disk Drives” in *7th IFAC Symposium on Robust Control Design* Aalborg, Denmark, 2012, pp 653-658
- **E. Keikha**, A. A. Mamun, C. S. Bhatia , T. H. Lee “Multi-Frequency Technique for Frequency Response Measurement and its Application to Servo System with Friction” in *18th IFAC World Congress* Milano, Italy, 2011. pages 5273-5278
- **E. Keikha**, M.Chamnabaz, A. A. Mamun, C. S. Bhatia “Design of Track Following Controller of Dual Actuated HDD Servo for 10 Tb/in<sup>2</sup> Magnetic Recording” in *International Conference on Control, Instrumentation, and Automation (ICCIA)* 2011, Shiraz, Iran, pp. 551-556.
- M.Chamnabaz, **E. Keikha**, V. Venkataramanan, A. A. Mamun, Q.-G. Wang, Y. F. Liew “ $H_\infty$  Probabilistic Robust Control of Hard Disk Drive Servo Systems” in *37th IEEE Industrial Electronic Society Conference (IECON)* 2011, Melbourne, Australia, pp 3275-3280.